DESIGN AND EVALUATION OF A MICROPROCESSOR-CONTROLLED POWERED HIP PROSTHESIS

KELLY BRANNEN

Thesis submitted to the University of Ottawa
in partial Fulfillment of the requirements for the
Master of Applied Science in Biomedical Engineering

Ottawa-Carleton Institute for Biomedical Engineering
Faculty of Engineering
University of Ottawa

Abstract

Hip disarticulations and hemipelvectomies are the highest level of lower limb amputations. As such, these amputations create ambulation difficulties and current prosthetic solutions are limited. Powered prosthetic joints have successfully improved lower limb amputee gait; however, no powered hip joints are available on the market. This thesis presents the design and evaluation of a microprocessor-controlled powered hip joint for hip-level amputees. A rope and pulley system was used to transmit power from an actuator located at the prosthetic thigh to rotate the prosthetic leg around an anteriorly-located prosthetic hip joint. The pulley system features an innovative tensioning system using multiple keyways, allowing the system to be tensioned without external tensioning devices. The powered hip prosthesis passed ISO 15032:2000 mechanical strength tests that simulated 100 kg user loads. The joint was also tested by able-bodied individuals using a hip disarticulation simulator to walk with the powered hip-knee-ankle-foot prosthesis. Though the participants had asymmetrical gait with shorter intact-side swing time, the device successfully allowed the participants to ambulate. The final device weighed 3.9 kg and respected geometric design constraints to fit comfortably under pants. Future work is needed to implement a gait control system, resolve a rope slack issue, and test the device with hip-level amputees.

Table of Contents

Table of Figures

List of Tables

Definitions

Abduction	Motion of a limb away from the midline of the body
Adduction	Motion of a limb towards the midline of the body
Ambulation	The act of walking
Anterior	Towards the front of the body
Bearing	Mechanical part that reduces friction between two objects
Distal	Away from the point of attachment to the body
External Rotation	Rotating anterior surface of limb away from midline of body
Frontal Plane	Vertical plane dividing the body into front and back sides
Gait Cycle	Interval between repetitive events of walking
Hemipelvectomy	Amputation of the leg and a portion of the pelvis
Hip Disarticulation	Amputation of the leg at the hip joint
Internal Rotation	Rotating anterior surface of limb towards midline of body
Lamination Plate	Plate within hip socket to which prosthesis is fixed
Lateral	Away from the centre of the body
Medial	Towards the centre of the body
Posterior	Towards the back of the body
Proximal	Towards the point of attachment to the body
Pylon	Weight-bearing structure between prosthetic joints
Pyramid Adapter	Part used to join prosthetic components
Sagittal Plane	Vertical plane dividing the body into left and right sides
Transfemoral Amputation	Amputation of the leg between the knee and the hip
Transtibial Amputation	Amputation of the leg between the ankle and the knee
Transverse Plane	Horizontal plane dividing the body into top and bottom sides

Abbreviations

A-P	Anterior-Posterior
ASME	American Society of Mechanical Engineers
A_t	Stress area
b	Gear face width
c	Distance from shaft centre
CAD	Computer-Aided Design
d	Gear diameter
D_i	Inner diameter
D_o	Outer diameter
F	Force
FBD	Free Body Diagram
F_{BHTS1y}	y direction force between the top shaft and the lateral side of the bearing housing
F_{BHTS2x}	x direction force between the top shaft and the medial side of the bearing housing
F_{BHTS2y}	y direction force between the top shaft and the medial side of the bearing housing
F_{BSMy}	y direction force between the bottom shaft and the motor
FEA	Finite Element Analysis
F_{HLP1x}	x direction force between the top hinge and the lamination plate distal end
F_{HLP1y}	y direction force between the top hinge and the lamination plate distal end
F_{HLP2x}	x direction force between the top hinge and the lamination plate proximal end
F_{HLP2y}	y direction force between the top hinge and the lamination plate proximal end
F_{KMx}	x direction force between the knee and the motor
F_{KMy}	y direction force between the knee and the motor
F_{MBHx}	x direction force between the motor and the bearing housing

F_{MBHy}	y direction force between the motor and the bearing housing
F_{PBSy}	y direction force between the pulley and the bottom shaft
F_{PTSy}	y direction force between the pulley and the top shaft
F_t	Gear teeth tangential force
F_{test}	Test Force
F_{TSH1x}	x direction force between the top shaft and the lateral side of the top hinge
F_{TSH1y}	y direction force between the top shaft and the lateral side of the top hinge
F_{TSH2y}	y direction force between the top shaft and the top hinge medial side
F_x	x direction force
F_y	y direction force
GRF	Ground Reaction Forces
HD	Hip Disarticulation
HMPE	High Molecular Weight Polyethylene
HP	Hemipelvectomy
I	Moment of inertia
ISO	International Organization for Standardization
J	Helical gear geometry factor, Polar moment of inertia
k_a	Surface condition modification factor
k_b	Size modification factor
k_c	Load modification factor
k_d	Temperature modification factor
k_e	Reliability factor
K_f	Fatigue stress-concentration factor for bending
k_f	Miscellaneous-effects modification factor
K_{fs}	Fatigue stress-concentration factor for torsion
K_m	Mounting factor
K_o	Overload factor
K_v	Velocity factor
l	Key length

LCP	Liquid Crystal Polymer
M	Moment, Bending moment
m	Gear module
M_a	Alternating bending moment
M_{BSMz}	Moment between the bottom shaft and the motor about the z-axis
M_{KMz}	Moment between the knee and the motor about the z-axis
M-L	Medial-Lateral
M_m	Midrange bending moment
M_{MBHz}	Moment between the motor and the bearing housing about the z-axis
M_z	Moment about the z-axis
n	Number of gear teeth, safety factor
PBO	Polybenzobisoxazole
PHP	Power Hip Prosthesis
PTFE	Polytetrafluoroethylene
R	Reaction force
r	Radius
SAI	Stair Assessment Index
S_e	Endurance limit
S_e'	Test specimen endurance limit
S_p	Proof load
S_{sy}	Shear strength
S_{ut}	Ultimate tensile strength
S_y	Yield strength
T	Torque
t	Key width
T_a	Alternating torque
TF	Transfemoral
T_m	Midrange torque
UV	Ultraviolet

V	Shear force
σ	Bending stress
σ'	Von Mises stress
σ_a	Alternating bending stress
σ'_a	Alternation von Mises stress
σ_m	Midrange bending stress
σ'_m	Midrange von Mises stress
τ	Torsional stress; shear stress
τ_a	Alternating torsional stress
τ_m	Midrange torsional stress
ω	Angular velocity

Acknowledgements

I would like to start by thanking my thesis supervisors, Dr. Edward Lemaire and Dr. Natalie Baddour, for their guidance and support throughout this project.

Thank you to David Langlois for acting as a liaison with Össur, for providing valuable design input, and for supporting this project through completion. Thank you to the rest of the Össur staff that contributed to this project as well. Specifically, Aron Ingi Ingvason for conducting the mechanical strength testing in Iceland and Guðni Ingimarsson for contributing design input and assisting during the assembly process.

I would also like to acknowledge Dr. Patrick Dumond from the University of Ottawa for advising on design issues numerous times. Thank you for always being willing to help and for sharing your mechanical expertise.

A special thank you goes out to the entire Power Hip Research Team at the University of Ottawa. To Hossein Gholizadeh for providing expertise and guidance as a prosthetist. To Farshad Golshan for his hard work on the electrical and control systems. To Yousef Bader for his help with the assembly, functional testing, and in resolving the issue with the slack in the rope. To Michael Botros for his teamwork and positive energy throughout the project. Lastly, to Sarah Mroz for her collaboration throughout the project and for becoming a good friend along the way.

Thank you to all my family and friends that have supported me through this thesis. You have acted as sounding boards for my ideas, as moral support, and as much needed study breaks – all of which have provided tremendous support in completing this project.

Most importantly, thank you Mom and Dad. You have supported me in countless ways from day one. I would not be where I am today without you.

Chapter 1: Introduction

Prosthetic limbs are used to restore mobility for people with lower limb amputations. However, design challenges such as providing adequate torque without a large weight lead to greater energy requirements than people without amputations [1]. Walking performance is more affected at more proximal amputation locations [2]. Hip disarticulation (HD) is amputation at the hip and hemipelvectomy (HP) is the amputation of the entire leg plus a portion of the pelvic bone [3]. People with these amputations often have difficulty walking with prostheses and less than 50% of HD and HP amputees use a prosthesis in everyday life [4]. This low number is due to several factors, including socket intolerance, instability, and excessive energy expenditure [4].

Advancements in prosthetic limbs, such as microprocessor-controlled damping and powered joints, have improved lower limb amputee mobility [5]. However, there are currently no powered or microprocessor-controlled devices on the market for hip-level amputations. A powered hip prosthesis (PHP) would be able to replicate the hip moments that HD and HP amputees are missing and thus restore a more natural gait. Furthermore, a microprocessor-controlled joint would be better able to adapt to the walking environment and stumbles.

In this thesis, a microprocessor-controlled PHP design was developed for HD and HP amputees. A mechanical pulley system was created in SolidWorks Computer-Aided Design (CAD) software to transfer power from an actuator located on the thigh to an anterior hip location consistent with current HD prostheses. Stress calculations and Finite Element Analysis (FEA) were performed to ensure that the device can withstand the forces in walking, sitting, standing, and stair climbing. Next, mechanical tests were performed on a prototype to validate the adherence to the International Organization for Standardization (ISO) standard 15032:2000 Prostheses – Structural testing of hip units. Finally, a hip disarticulation simulator was used to allow able-bodied individuals to walk with the powered hip-knee-ankle-foot (HKAF) prosthesis.

1.1 Rationale

Currently, less than 50% of HD and HP amputees use a prosthesis in everyday life [4]. The limitations of currently available devices result in unnatural gait patterns and increased energy expenditure [6]. Adding an actuator to the hip prosthesis could restore hip flexion and extension

power, allowing people to recover a more natural gait. This has the potential to increase the low end-user acceptance rates currently seen with HD and HP prostheses.

In addition to walking, the PHP will help users to complete other daily motions, such as walking up and down stairs and going from sitting to standing and from standing to sitting. Stair ascent could be particularly important, since HD and HP amputees are currently limited to the step-by-step stair ascent strategy [7]. A power hip joint may allow users to employ the step-over-step strategy, which is quicker and more efficient.

The PHP will be the first microprocessor-controlled prosthetic hip joint. Microprocessor control may result in better reactions to user movements, including stumbles. This could increase safety compared to non-microprocessor-controlled devices.

The actuator is located on the thigh, inferiorly to the hip centre of rotation. This system has applications in other wearable systems where the power source may not be able to be located directly at the joint.

1.2 Objectives

The overall goal of this thesis was to design and validate a mechanical system to transfer power from an actuator located on the thigh to the hip centre of rotation in a microprocessor-controlled PHP. The specific objectives are:

1. Design a mechanical power transmission system that will rotate the prosthetic leg about the prosthetic hip joint using power from an actuator located on the thigh,
2. Integrate the mechanical design into a microprocessor-controlled PHP,
3. Evaluate the PHP mechanical properties in accordance with ISO standard 15032:2000 Prostheses – Structural testing of hip joints,
4. Evaluate PHP function with able-bodied participants using a hip disarticulation simulator.

1.3 Thesis Contributions

The principal contribution of this thesis was the design and validation of a viable powered hip joint that will improve gait for people with HD or HP amputations. Specific thesis contributions are:

1. Design of a light and compact pulley system capable of transferring the required torque from the actuator to the hip joint. This design approach created a device that is thinner than a person's thigh, thereby fitting under clothes and potentially being aesthetically acceptable. From a mechanical perspective, this pulley approach could be considered for other powered systems where moving the motor away from the axis of rotation is desirable.
2. Mechanical design stress analysis that determined that the system is strong enough to withstand loads encountered in walking, stair climbing, sitting, and standing. Strength calculations confirmed minimum safety factors above 1 in all PHP components for both static and cyclical loading conditions.
3. PHP mechanical testing that verified that the device adheres to ISO 15032:2000. The PHP sustained the standard's 100 kg user loads without permanent deformation.
4. PHP functional testing using a new HKAF prosthesis simulator, which demonstrated both PHP and simulator performance for walking. Able-bodied participants successfully walked with the PHP using the simulator.
5. Contribution to a published scoping review of HD and HP prostheses literature [8].

1.4 Thesis Outline

This thesis is divided into 10 chapters. Chapter 2 is a literature review of transfemoral amputee gait and existing hip prostheses. Chapter 3 presents the PHP design criteria, including mechanical requirements and geometric restrictions. Chapter 4 evaluates PHP design candidates, including a direct drive system, a gear drive system, a belt drive system, a chain and sprocket system, and a pulley and rope system. Chapter 5 presents the final PHP design and components. Chapter 6 shows a failure analysis of the PHP components, using calculations and FEA. Chapter 7 outlines the prototyping process and presents pictures of the PHP prototype. Chapter 8 discusses the PHP mechanical evaluation. Chapter 9 presents PHP functional testing using the hip disarticulation simulator. Chapter 10 concludes the thesis with a results summary and future work to be done on the PHP.

Chapter 2: Literature Review

This chapter reviews existing HD and HP prosthetic devices as well as kinetics and kinematics of transfemoral (TF) amputee movement to help determine PHP design criteria.

2.1 Gait Cycle

The gait cycle is the series of motions that are repeated during locomotion, consisting of stance phase where the reference foot is in contact with the ground and swing phase where the reference foot is in the air [9]. Stance and swing can be further divided into seven subphases (Figure 2-1).

The first subphase is loading response, which begins at initial contact when the reference foot first contacts the ground and ends at opposite foot off when the contralateral foot leaves the ground [9]. Next, midstance begins with opposite foot off and ends at heel rise, where the reference foot heel begins to lift from the ground. Terminal stance follows midstance, ending at opposite initial contact when the contralateral foot contacts the ground. Stance phase finishes with the pre-swing period, which begins at opposite initial contact and ends with foot off, where the reference foot loses contact with the ground.

Swing phase occurs from around 60% of the gait cycle to 100%, beginning with initial swing [9]. The initial swing period ends at feet adjacent when both feet are aligned horizontally. Feet adjacent marks the beginning of mid-swing, which ends when the reference leg tibia is vertical. Terminal swing is the final subphase and lasts until initial contact, at which point the gait cycle repeats itself.

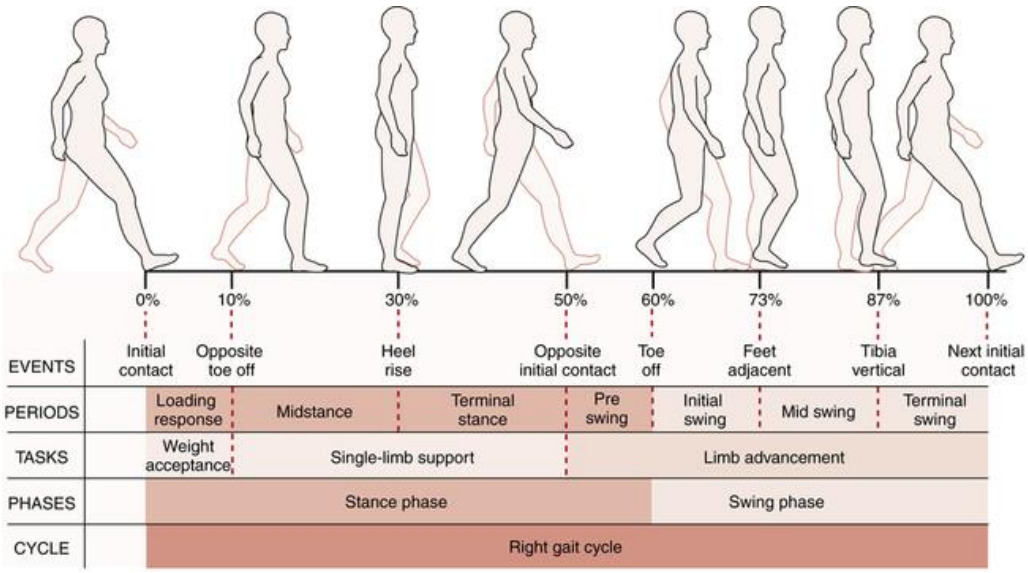

Figure 2-1 Gait cycle subphases and events [9]

Each gait cycle subphase features unique kinetics and kinematics at the ankle, knee, and hip. The angles, moments, and powers observed throughout the gait cycle provide quantitative measures to compare normal and pathological gait. These values are important when developing a prosthetic device that will be able to withstand the loads faced during locomotion, as well as provide the necessary power to replicate natural gait patterns.

In this thesis, the PHP was only evaluated for level-ground walking because simple gait controls were developed for walking. A final PHP with an appropriate control system should be able to perform other daily motions. Specifically, the PHP should accommodate sit-to-stand, stand-to-sit, stair climb, and stair descent movements.

2.2 Transfemoral Amputee Mobility

TF amputations occur between the knee and the hip, allowing the amputee to retain normal hip function and achieve better mobility than HD and HP amputees [5]. The PHP uses the same knee and ankle prostheses as TF amputees and aims to replace the muscle function at the hip with an actuator. Therefore, TF amputee gait is a reasonable reference for the PHP. The objective is to attain similar symmetry, gait parameters, and functional abilities as observed in TF amputees.

2.2.1 Transfemoral Amputee Gait

A study by Segal et al. [10] looked at the gait of eight TF amputees using two different prosthetic knees, Ottobock C-Leg with microprocessor-controlled damping (Figure 2-2) and Össur Mauch SNS knee (Figure 2-3), which is non-computerized. Average joint angles, moments, and power are presented in Figure 2-4.

Figure 2-2 Ottobock C-Leg with microprocessor-controlled damping [11]

Figure 2-3 Össur Mauch SNS knee [12]

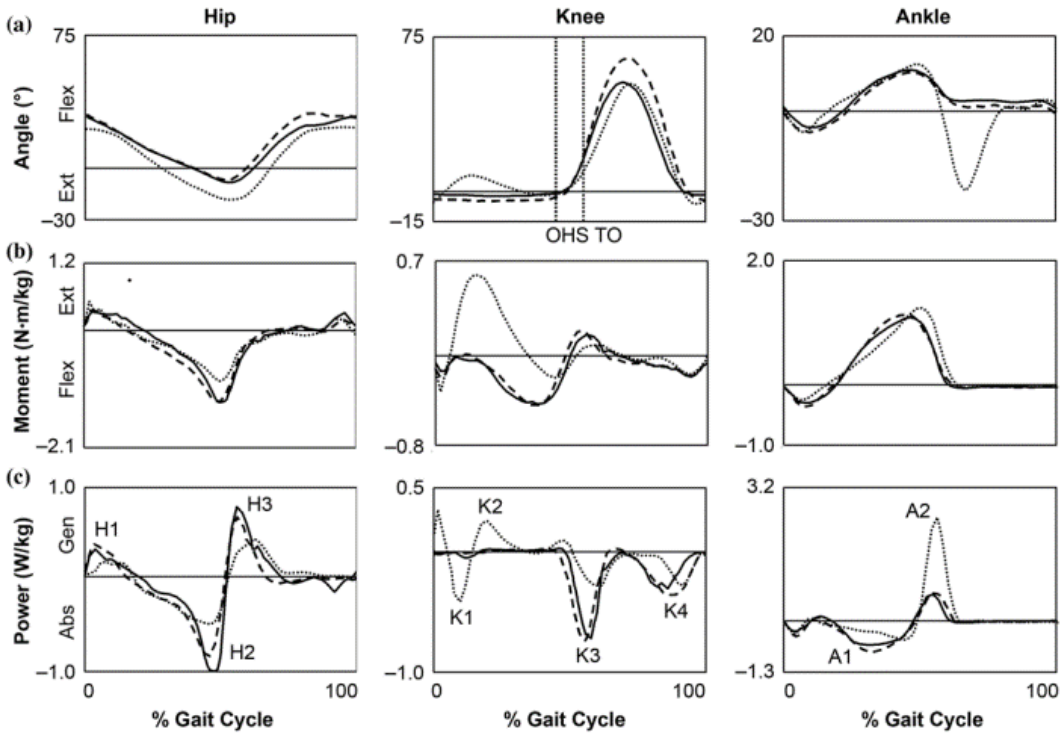

Figure 2-4 Prosthetic limb kinematics and kinetics for participants wearing C-Leg (solid line), Mauch SNS (dashed line), or control group (dotted line) [10]. Power generation (Gen) indicates a concentric motion where the hip is generating the movement. Power absorption (Abs) indicates an eccentric motion where the hip is resisting motion caused by gravity or momentum.

The kinematic and kinetic results for the C-Leg are of particular importance to this thesis since the PHP will be paired with a microprocessor-controlled knee. The maximum hip moment for participants walking with the C-Leg was 1.275 Nm/kg of flexion [10], occurring in pre-swing when the hip is at its maximum extension.

Three values of interest for power generation at the hip (Figure 2-4) are: H1, peak sagittal plane hip power generation in early stance; H2, peak sagittal plane hip power absorption in midstance; and H3, peak sagittal-plane power generation in late stance [10]. For C-Leg, H1 = 0.46 W/kg, H2 = 1.0 W/kg, and H3 = 0.75 W/kg [10].

2.2.2 Transfemoral Amputee Sit-to-Stand and Stand-to-Sit

Another important daily motion is sitting down and standing up. With adults averaging 60 sit-to-stand movements a day [13], prosthetic devices need to support this motion in a smooth and timely manner. Highsmith et al. [14] studied joint kinetics asymmetry for unilateral TF amputees, comparing the sound leg ground reaction forces (GRF) and joint moments to the prosthetic side

for four groups: a non-amputee control group, C-Leg users, Mauch SNS users, and Össur Power knee users (Table 2-1). Force plates measured GRFs that participants exerted onto the ground.

Table 2-1 Participant mean and standard deviation for sit-to-stand and stand-to-sit kinetic results, for an able-bodied control, Össur Power Knee, C-Leg, and Mauch SNS knee groups, where Pros is the prosthetic side for the prostheses groups and the non-dominant side for the control group, and intact is the healthy non-amputated side for the prostheses groups and the dominant side for the control group [14]

Group	Pros GRF (N/kg)	Intact GRF (N/kg)	Pros Knee Flexion Moment (N/kg)	Intact Knee Flexion Moment (N/Kg)	Pros Hip Extension Moment (N/kg)	Intact Hip Extension Moment (N/kg)	Total Event Duration (s)
Sit to stand							
Control	5.2 ± 0.5	6.0 ± 0.5	-0.44 ± 0.16	-0.41 ± 0.16	0.44 ± 0.13	0.66 ± 0.12	1.6 ± 0.1
Power knee	2.7 ± 0.9	8.8 ± 0.7	0.06 ± 0.04	-0.57 ± 0.15	0.46 ± 0.19	0.92 ± 0.26	1.6 ± 0.3
C-Leg	1.9 ± 0.6	9.1 ± 0.1	0.02 ± 0.06	-0.42 ± 0.15	0.25 ± 0.15	0.91 ± 0.36	2.0 ± 0.8
Mauch SNS	1.7 ± 0.6	9.6 ± 0.5	0.04 ± 0.02	-0.59 ±0.22	0.26 ± 0.08	1.02 ± 0.14	1.7 ± 0.5
Stand to sit							
Control	5.2 ± 0.7	5.9 ± 0.7	-0.40 ± 0.14	-0.43 ± 0.21	0.47 ± 0.20	0.66 ± 0.20	1.6 ± 0.2
Power knee	3.4 ± 1.0	6.5 ± 0.8	-0.05 ± 0.16	-0.36 ± 0.21	0.32 ± 0.19	0.78 ± 0.15	2.3 ± 0.8
C-leg	2.2 ± 0.9	7.3 ± 0.8	-0.05 ± 0.14	-0.48 ± 0.16	0.12 ± 0.09	0.70 ± 0.18	2.8 ± 0.6
Mauch SNS	2.0 ± 0.9	8.1 ± 0.7	0.03 ± 0.08	-0.57 ±0.14	0.28 ± 0.10	0.76 ± 0.12	2.1 ± 0.4

The largest prosthetic side hip moment in sit-to-stand was 0.46 ± 0.19 N/kg (mean and standard deviation) for the power knee users; however, no significant differences were found between the four groups ($p < 0.05$) [14]. The level of asymmetry between the prosthetic leg and the sound leg, or the dominant and non-dominant legs in the control group, was measured as the difference between the sound (or dominant) side hip moment and the prosthetic (or non-dominant) side hip moment, over the sum of the two moments. The control group had 21 ± 10 % asymmetry, compared to 34 ± 16 % for power knee users, 54 ± 36 % for C-leg users, and 59 ± 8 % for Mauch SNS users [14]. Significant differences were found between Mauch SNS group asymmetry and both the control and power knee groups ($p < 0.05$) [14]. Asymmetry between the two legs is detrimental because it places more work on the intact limb. Therefore, increasing the moment on the prosthetic side is beneficial to reducing asymmetry.

In stand-to-sit, the largest prosthetic side hip moment was 0.47 ± 0.20 N/kg in the control group. The only significant difference ($p < 0.05$) between the four groups was between the control

group and the C-Leg users, who had an average prosthetic side hip moment of 0.12 ± 0.09 N/kg. These groups also had significantly different hip moment asymmetries with 19 ± 10 % asymmetry in the control group and 71 ± 20 % asymmetry in the C-Leg group.

The total event duration (Table 2-1) provides another PHP design parameter. The device should allow the user to sit down and stand up in a similar amount of time to TF amputees. For C-Leg users, the event duration for sit-to-stand was 2.0 ± 0.8 s and stand-to-sit was 2.8 ± 0.6 s.

When examining correlations between the amputated leg residual limb length and joint moments during sit-to-stand and stand-to-sit [15], no significant correlations were found between residual limb length and hip moment on the prosthesis side for sit-to-stand or stand-to-sit. Therefore, the values described in [14] for hip moments and event duration should be applicable to TF amputees in general, regardless of residual limb length.

These two studies have limitations since each participant only used one of the knee prostheses, so there could be other factors affecting differences between the groups [14], [15]. Furthermore, many hip moment results had large standard deviations; however, these results can still provide a good baseline for the level of torque required at the hip joint while performing sit-to-stand and stand-to-sit.

2.2.3 Transfemoral Amputee Stair Ascent and Stair Descent

Stair climbing is an important aspect of mobility that can greatly improve a user's access to buildings and varied terrain. A study with 12 TF amputees wearing the C-Leg knee joint found that the peak hip flexion moment on the prosthetic side during stair descent was 0.47 ± 0.25 Nm/kg [16]. This was a non-significant ($p < 0.05$) difference from the non-amputee control group, who had a peak hip moment of 0.39 ± 0.16 Nm/kg [16]. TF hip joint moments followed a similar pattern to the control group, beginning with flexion moments in the early support phase, followed by extension moments [16]. Wolf et al. found that the peak hip power generation in stair descent for TF amputees using the C-Leg was 0.4 ± 0.2 W/kg [17].

Another metric used to measure stair ambulation performance is the stair assessment index (SAI). SAI is a 14-level scale that describes the person's functional independence and technique in stair ascent and descent [18]. The levels range from 0, indicating that the participant cannot or will not perform the activity, to 13, indicating that the participant can ascend or descend the stairs

in a step-over-step pattern without the use of an assistive device or rail [18]. SAI scores for TF amputees in stair descent were around 10 when participants used a microprocessor-controlled knee and around 4 when the same participants used a non-microprocessor knee [19].

For stair ascent, peak hip power generation was 2.0 ± 1.2 W/kg for C-Leg users [17], with an SAI score of around 5 for both microprocessor-controlled and non-microprocessor knees [19]. Similarly, a mean SAI value of 6.2 and a median value of 5 for TF amputees in stair ascent were also found [20], and SAI scores were not correlated with residual limb length [20].

2.3 Hip Disarticulation and Hemipelvectomy Prostheses

With a small population of HD and HP amputees, the market for hip prostheses is small and few advancements have been made in this field compared with other prosthetic joints [4]. Still, several types of hip prostheses provide a good starting point for the PHP design.

2.3.1 Canadian Type Hip Prosthesis

The Canadian hip prosthesis was proposed by McLaurin in 1954 [21], and many exoprosthetic hip joints today are still based on that model. Two important aspects of the Canadian hip disarticulation prosthesis are hip joint position and knee joint position. The hip joint is located anteriorly and inferiorly to the anatomical hip joint [22]. This positioning allows the user to sit down while donning the prosthesis. The hip joint is a hinge that allows rotation in the sagittal plane and prevents medial/lateral rotation [22]. The knee joint is positioned posteriorly to the hip joint, such that the load line from the foot to the hip always passes anteriorly to the knee joint [23]. This ensures that, as long as the prosthesis bears weight, the knee joint is stable and will not buckle [23]. The knee only flexes once the user initiates swing phase through upper thigh contact with an elastic bumper on the hip socket [23]. The Canadian hip prosthesis is pictured in Figure 2-5, demonstrating the anterior hip joint position and the corresponding knee joint position, along with the bumper located on the hip socket.

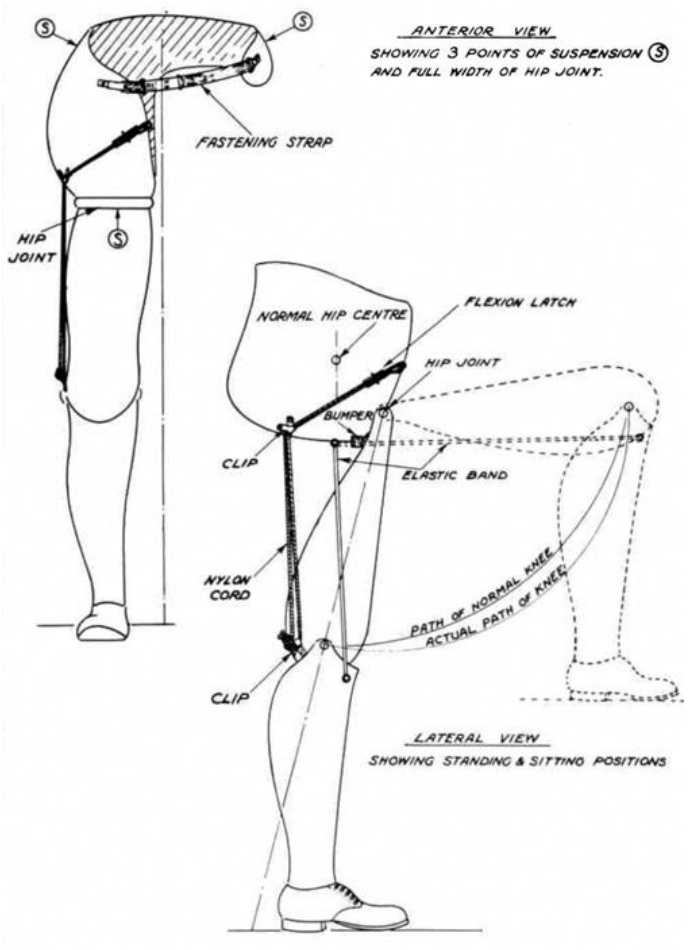

Figure 2-5 Canadian-type hip disarticulation prosthesis design [21]

Though Canadian hip prosthesis joint alignment creates stance phase stability, it also results in unnatural gait. The knee remains fully extended throughout stance phase [24], [25]. Contrarily, in normal gait, the knee reaches an 18° maximum stance phase flexion during loading response [26]. This stance phase knee flexion is one of the six determinants of gait that minimize energy consumption by reducing centre of gravity movement [27]. Knee flexion shortens the effective leg length, keeping the hip height as constant as possible [27]. When the knee remains fully extended, the body's centre of gravity rises and falls as the trunk moves over the extended leg. This results in a less efficient gait and higher energy expenditure [27].

Knee flexion in swing phase with a Canadian hip prosthesis is also less than in normal gait [24], [28]. This results in another Canadian design drawback since the prosthetic leg must be shorter than the non-amputated leg to provide adequate toe clearance without vaulting [29]. Another concern is that hip extension is not controlled until the leg hits a bumper on the hip socket

[22]. This can result in spine issues and causes the user to reach full hip extension before contralateral toe off, which is earlier than in normal gait [4]. Other deviations from normal gait seen in the Canadian hip prosthesis are a later hip flexion in swing phase, and increased pelvic tilt [4], [22], [28], [30]. These differences result in a less natural and more energy-consuming gait.

2.3.2 Helix3D Hip Prosthesis

The prosthetics company Otto Bock developed the Helix3D hip joint (Figure 2-6) that aims to reduce pelvic tilt, support swing phase initiation, and improve shock absorption, to allow for a more natural gait [31]. The joint uses a spatial four-axis mechanism to allow for natural internal and external hip rotation throughout the gait cycle, and hydraulic stance and swing phase resistance control [31].

Figure 2-6 Otto Bock Helix3D Hip Joint [31]

The Helix3D is mounted to the user's hip socket using a lamination plate (Figure 2-7). The lamination plate is a metal plate that is embedded into the hip socket. Prosthetic hip joints are bolted into the lamination plate.

Figure 2-7 Lamination plate that gets embedded into a hip socket. Hip joints are secured to the lamination plate [32]

In a 2011 study, 6 participants with HD walked with both the Helix3D hip joint and the 7E7 joint, which is based on the Canadian model [4]. The Helix3D extended slower than the 7E7 and reached full extension later, which resulted in a less abrupt stop that more closely resembled natural gait [4]. The range of pelvic tilt was also significantly ($p < 0.05$) reduced by $5° \pm 3$ with the Helix3D system [4]. Furthermore, both stance phase knee flexion and maximum swing phase knee flexion were greater with the Helix3D than with the 7E7 [4]. These results suggested that the Helix3D can reduce gait abnormalities seen with traditional hip joint designs [4].

Conversely, Gailledrat et al. [33] found that people had difficulties walking with the Helix3D. Of the three participants in the study, the gait pattern improved for only one person who had his knee joint and prosthetic feet changed as well, which may partly account for the improvement. All three participants ultimately discontinued Helix3D use due to comfort problems [33]. A longer adaptation period may improve results with the Helix3D, but this study indicated that hip prosthesis improvements are still required.

2.3.3 Powered Hip Prostheses

Dampened devices can mimic isometric and eccentric muscle activity by resisting motions, but only powered devices can replace concentric muscle actions. Adding an actuator to the

prosthetic system can provide the power needed to perform gait motions that are otherwise impossible for people missing the required leg muscles. This added functionality can reduce energy consumption and asymmetries in gait, as well as increase walking speed [5]. Though actuators have been used in ankle and knee prostheses, there are no powered hip devices on the market to date [5].

Although no power hips are commercially available, recent studies have shown the potential of such a device [34], [35]. Ueyama, Kubo, and Shibata developed a robotic hip disarticulation prosthesis with two motors to power both the hip and knee joints [34]. They compared non-amputee gait using the robotic device with the same person using a non-powered device. The participant had a more natural and symmetric gait when using the powered device compared to the non-powered one [34]. The non-powered device produced a short step length and forward lean, both of which were eliminated with the robotic device [34]. One limitation is that the powered prosthesis was much heavier than other hip prostheses [34]. This extra weight means that the power hip joint may not reduce fatigue, although the gait will be smoother [34].

Another study demonstrated that a powered hip exoskeleton can reduce the metabolic cost of walking for TF amputees [35]. Unlike prostheses, which replace the missing limb, exoskeletons are external devices that attach to the natural or prosthetic leg. The authors reported a metabolic improvement "equivalent to removing a 12-kg backpack from a nonamputee individual" when TF participants walked with the powered device [35]. Though this study examined an exoskeleton instead of a prosthesis and involved TF instead of HD participants, the results demonstrated the positive effect of adding power at the hip joint. These benefits will likely translate to a powered hip prosthesis.

Chapter 3: Design Criteria

This chapter presents the PHP design criteria. These criteria were selected to ensure that the PHP can withstand ambulatory loads and provide adequate power to replicate TF gait in HD and HP amputees. The PHP design must use power from the actuator to rotate the prosthetic leg about the hip centre of rotation following the design criteria outlined in this chapter.

3.1 Device Weight

Lower prosthetic leg weight is correlated with reduced walking metabolic cost [36]. As such, the PHP has a maximum weight criterion to minimize the users' energy expenditure. This weight limit encompasses all the PHP components, including the hip joint that affixes to the socket, power transmission system, actuator, battery, and all structural pieces. Also included in the weight limit is the pylon that connects the PHP bottom to the knee.

Össur's power knee weighs 3.2 kg [37] and the PHP uses the same actuator and battery as the power knee. The PHP is also a more complex system than the power knee because, unlike the knee, it is not a direct drive system and hence requires additional components to transmit rotational power. Therefore, the PHP requires a maximum weight criterion greater than 3.2 kg. Fortunately, increased mass affects metabolic cost less when the mass is located proximally [36]. Since the PHP mass is proximal to the hip, the mass will not be as detrimental in terms of energy expenditure. To allow room for the additional components while keeping the weight minimal, a 4.0 kg maximum device weight was chosen.

3.2 User Weight

As user weight increases, the GRFs and, consequently, the forces on the prosthesis increase. A maximum user weight must therefore be enforced to ensure that the prosthesis can support ambulatory loads. The stress analysis and power requirements are based on this maximum user weight. A larger maximum user weight allows a greater percentage of the population to use the device but requires more strength and often results in a heavier device.

The leading-edge HD prosthesis, OttoBock's Helix3D, has a user weight limit of 100 kg [38]. 100 kg is the 75^{th} mass percentile for adult men, but since prosthetic legs weigh less than anatomical legs, this weight limit encompasses greater than 75 percent of men. The prosthesis

weight limit includes the device weight itself. Using a conservative 10 kg estimate for the total prosthesis weight [39], [40], the 100 kg weight limit allows for an amputee weight of up to 90 kg. Considering that HD and HP amputees are missing a leg, which is on average 20.37% of the body weight [41], a 90 kg amputee would be equivalent to a 113 kg non-amputee. 113 kg is greater than the 90th mass percentile for adult females in the US and greater than the 85th percentile for adult males in the US [42]. 100 kg was therefore selected as the maximum user weight to be consistent with the Helix3D and because it covers a large percentage of the population.

3.3 Strength

Strength is an important factor in PHP design. The device must support users throughout gait and other daily movements without failure. The actuator will also place loads on the PHP that must be withstood.

ISO standard 15032:2000 [43] outlines structural testing requirements for prosthetic hip joints. These test loads serve as design criteria for the PHP. Firstly, for a 100 kg user, the hip joint must be able to withstand a 2240 N load for 30 seconds without failure or total device deformation greater than 15 mm. The joint must also not experience ductile failure at a load below the ultimate test force of 3360 N. Finally, the PHP must be able to withstand 2×10^6 cycles of cyclic testing with a minimum force of 50 N and a maximum force of 1330 N.

Additionally, the PHP must be able to withstand any loads generated by the actuator. These loads depend on the power transmission design and are considered in the stress analysis.

3.4 Range of Motion

The PHP must have a normal hip range of motion. As the leg rotates, the mechanical components must not impede the range of motion. Specifically, the leg must not hit the socket during extension (except by design when a physical stop is used at maximum extension). Additionally, the method of power transmission must allow for sufficient flexion when performing daily tasks. Range of motion design criteria define the range of motion that the PHP must attain.

Non-amputees walk with 20° maximum hip extension [10]. Though TF amputees walking with the C-Leg only had 8° hip extension [10], a design criterion of 20° hip extension was chosen to accommodate variances in gait.

90° of hip flexion is needed to sit comfortably. A greater range of motion is necessary to perform tasks that involve bending forwards, such as tying shoes. As such, a 130° hip flexion criterion was selected.

3.5 Hip Moment

The Össur actuator used in the PHP has a 96 Nm maximum torque output. The PHP design must transmit this torque to the hip joint to cause hip flexion and extension. The method of power transmission must be able to provide adequate moments at the hip as defined by a maximum hip moment criterion. This criterion was chosen based on the maximum hip moments seen during TF and non-amputee gait and sitting and stair-climbing motions.

The maximum hip moment during gait is in pre-swing during power absorption [10]. The hip generates a flexion moment to resist further extension. To reduce the load on the actuator, a physical stop can prevent the leg from extending past the maximum extension angle. Therefore, the maximum torque needed from the actuator is when the hip enters power generation. At this point, the leg begins to move in flexion so the moment can not be achieved with a physical stop. The maximum TF amputee power generation hip moment is 1.08 Nm/kg for Mauch SNS users and 1.23 Nm/kg for C-Leg users. For non-amputees, the maximum power generation hip moment is 0.793 Nm/kg [10]. For a 100 kg user, these values are equivalent to 108 Nm for the Mauch SNS users, 123 Nm for C-Leg users, and 79.3 Nm for non-amputees.

To reduce the hip moment asymmetry between the prosthetic and intact legs during sit-to-stand and stand-to-sit, the maximum prosthetic-side hip moments of all groups were used as design criteria for these actions. The power knee group has the largest prosthetic-side hip moment for sit-to-stand with 0.46 N/kg [14]. Incorporating the power knee group's mean height of 180.1 cm and the maximum user weight of 100 kg results in a 82.8 Nm moment. The control group has the largest stand-to-sit prosthetic-side hip moment with 0.47 N/kg and has a mean height of 174.4 cm [14]. Therefore, the maximum moment required for stand-to-sit is 82.0 Nm. In stair descent, C-Leg users generate a maximum prosthetic side hip moment of 0.47 Nm/kg [16]. For a 100 kg user, this would be equivalent to 47 Nm.

The largest hip moment observed in these four daily movements is in TF amputee gait. Though ideally, the PHP would provide the 123 Nm hip moment seen in C-Leg user gait, hip

angular velocity can be increased with the motor, generating the same amount of power with less torque. Using the Össur motor's 96 Nm maximum output as the design criterion means that a 1:1 torque ratio can be used between the actuator and hip joint. Not amplifying the torque simplifies the design and likely makes the device lighter. A 96 Nm hip moment is greater than the moment needed in non-amputee gait and is also larger than the moments required in TF sit-to-stand, stand-to-sit, and stair descent. Therefore, a 96 Nm hip moment criterion was selected.

3.6 Angular Velocity

Like with the hip moment, an angular velocity design criterion that must be met when the PHP transfers the power from the actuator to the hip. The leg rotates about the hip at varying angular velocities throughout the gait cycle. The PHP must match these angular velocities to replicate TF amputee gait and sustain an adequate walking speed. The maximum angular velocity needed at the hip is based on the maximum angular velocity observed in TF amputee gait.

At a 1.1 m/s walking speed, the maximum C-Leg user prosthetic side hip angular velocity is approximately 130 °/s [5]. Non-amputee controls experienced a maximum hip angular velocity of around 150 °/s at the same walking speed. TF amputee self-selected walking speeds have been reported between 0.82 m/s and 1.2 m/s [44]–[46]. Therefore, the angular velocity measured at 1.1 m/s walking speed should be appropriate for most TF amputee gait. A design criterion of 150 °/s was chosen to accommodate gait variances and faster walking speeds.

3.7 Anterior Protrusion

The PHP must be able to easily fit under the user's pants. Therefore, it must not protrude far in front of the socket. A design criterion was chosen that the PHP could not protrude at the hip joint more than 20 mm anteriorly from the top of the lamination plate.

3.8 Medial and Lateral Protrusion

To avoid hitting obstacles, the PHP should not protrude laterally beyond the user's hip width. Thus, a lateral protrusion design criterion was used. To ensure that the PHP could be used by as many people as possible, the lateral protrusion was designed using the 15th percentile female hip breadth, which is 31.96 cm [47]. 31.96 cm is also between the 10th and 15th percentile of male hip breadth [47]. Since the lamination plate is located ¼ of the hip breadth from the socket's lateral

end (Figure 3-1), the PHP should not protrude farther than 31.96/4 or 7.99 cm laterally from the lamination plate's center.

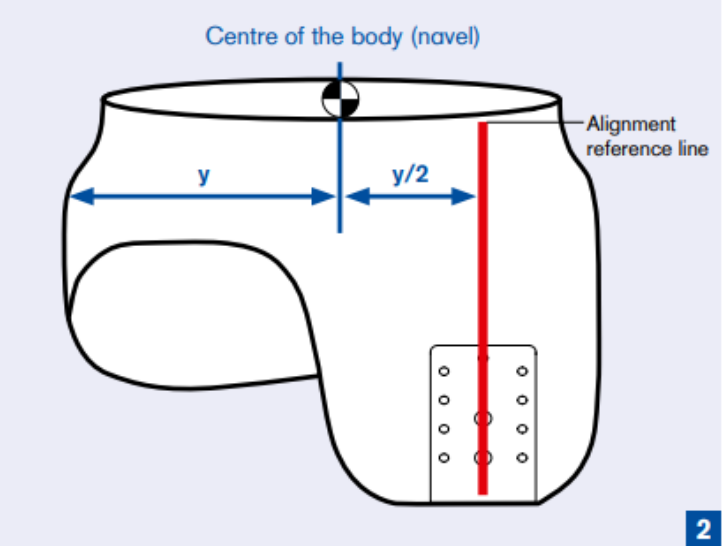

Figure 3-1 Medial/lateral alignment of lamination plate in socket [48]

The PHP medial side requires more clearance to avoid hitting the contralateral leg. Therefore, the medial protrusion was limited by an additional 3 cm to 4.99 cm from the lamination plate centre.

3.9 Device Length

The PHP length needed to be minimized to ensure that the prosthesis would fit within the user's thigh length. The total PHP length includes the power transmission system, the electronics chassis that houses the battery and all other electronic components, and a pylon at the bottom to connect the PHP to the knee. A longer pylon can be used to accommodate taller users, so the short end of the height range is the main design concern. The 15th percentile women's height is 1541.8 mm and the 15^{th} percentile men's height is 1676.4 mm [49]. To accommodate the largest number of people, the PHP maximum length will be based on the shorter of the two heights, 1541.8 mm. Using anthropometric data, thigh length is 0.245*height [50], or 377.74 mm for the 15^{th} percentile women. This length accounts for the vertical distance between the knee joint and the hip joint, but since the PHP will be at an angle, the total length will be longer than 377.74 mm and trigonometry is required to calculate the total allowable length.

A schematic was used to determine the maximum allowable device length (Figure 3-2). The knee joint was located 30 mm posterior to the load line [51]. The load line location relative to the hip depends on the user, so a conservative estimate located the load line at 1/3 of the lamination plate length from the front. The length of the lamination plate bottom is approximately 130 mm, so the load line was placed 43.3 mm from the front. The neutral standing position was set at 5° of extension from vertical. A height-adjustable pylon was used so that the prosthetist can adjust leg length for each user. Össur's shortest height-adjustable pylon has a minimum length of 77 mm [52]. These values are displayed in Figure 3-2.

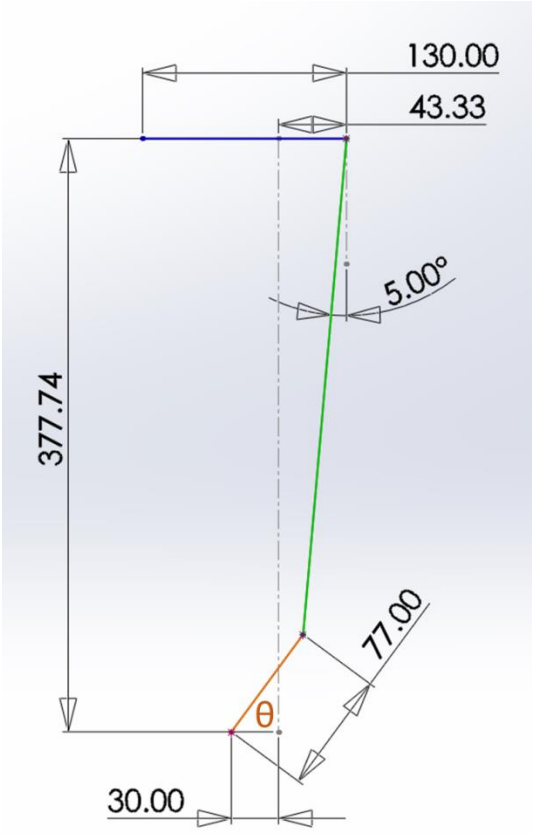

Figure 3-2 Schematic for determining the maximum allowable PHP length (green line) with a 77 mm pylon (orange line). The knee joint is located 30 mm posterior to the load line (grey dashed line), which is 1/3 of the lamination plate length (blue line) from the front.

Equations were written for the total superior-inferior length between the hip and knee joints (Eq. 3-1) and the total anterior-posterior distance between the hip and knee joints (Eq. 3-2), based on Figure 3-2:

$$L * \cos(5) + 77 * \sin(\theta) = 377.74 \quad \text{(Eq. 3-1)}$$

$$L * \sin(5) + 77 * \cos(\theta) = \frac{130}{3} + 30 \quad \text{(Eq. 3-2)}$$

where L is the PHP length (including the power transmission system and electronics chassis, but not the pylon), and θ is the pylon angle from horizontal (Figure 3-2). Solving the set of equations, $L = 316.98\,mm$ and $\theta = 53.59°$. The length from the bottom of the electronics chassis to the motor's centre is 220.5 mm. Therefore, the distance from the motor's centre to the hip joint must be kept under $316.98\,mm - 220.5\,mm = 96.48\,mm$.

3.10 User Safety

User safety is very important so the PHP must not have any open finger traps that could pinch or harm the user. Any possible hazards must be covered.

3.11 Design Criteria Summary

Table 3-1 summarizes the PHP design criteria.

Table 3-1 Summary of PHP design criteria

Criteria	Values
Device weight	Maximum 4.0 kg
User weight	Maximum 100 kg
Strength	Withstand 2240 N load for 30 s without failure or deformation >15 mm Withstand 3360 N without ductile failure Withstand 2×10^6 cycles between 50 N and 1330 N without failure
Range of motion	Minimum 20° hip extension Minimum 130° hip flexion
Hip moment	Minimum 96 Nm
Angular velocity	Minimum 150 °/s
Anterior protrusion	Maximum 20 mm from top of lamination plate
Lateral protrusion	Maximum 7.99 cm from centre of lamination plate
Medial protrusion	Maximum 4.99 cm from centre of lamination plate
Device length	Maximum 96.5 mm between the motor's centre and the hip joint
User safety	No uncovered finger traps

Chapter 4: Design Candidates

This chapter presents multiple design candidates that were considered for the PHP power transmission system, including direct drive, gear drive, belt drive, chain and sprockets, and rope and pulleys. Ultimately, as a result of the analysis outlined in this chapter, the rope and pulley system was chosen as the best option for the final PHP design.

4.1 Actuator

The actuator selected for the PHP design was the custom DC motor used in Össur's power knee prosthesis (Figure 4-1). This actuator has high torque, small size, and has proven successful as a knee actuator for users up to 116 kg [57]. The 96 Nm maximum torque and 300 °/s maximum angular velocity provide adequate moments and speed to meet the hip functional requirements outlined in Chapter 3:. The actuator outer diameter is 77 mm, which should be small enough to design a device within the geometric constraints. All design candidates discussed below were designed around the Össur power knee actuator.

Figure 4-1 Össur Power Knee [57]

4.2 Monocentric Versus Polycentric Hip Joint

The first design consideration was the type of joint to use at the hip. Prosthetic joints can be classified into two groups: monocentric and polycentric. Monocentric joints have a singular centre of rotation throughout the full joint range of motion. Polycentric joints, like four-bar

linkages, have an instantaneous centre of rotation that changes throughout the joint range of motion. The polycentric joint instantaneous centre of rotation is based on the joint angle. Both monocentric and polycentric joints have been used in hip prostheses, and they each provide advantages and disadvantages.

The first noted advantage of polycentric joints is increased stability. Prosthetic knees such as the Ottobock 3R106 and the Össur OH5/KH5 use four-bar linkages to provide increased stability in stance [53]. In monocentric knees, the knee is stable in weight-bearing when the knee centre is behind the user's load line [54]. When knee flexion begins, the knee center passes anterior to the load line and the knee is no longer stable. With a four-bar linkage, the linkages can be designed such that the instantaneous center of rotation remains posterior to the load line through the beginning of flexion. Thus, the knee remains stable through a larger portion of stance phase. The Helix 3D hip joint uses a polycentric hip joint to create stability using the same approach as polycentric knee joints [4]. Since a PHP uses a microprocessor-controlled motor, the hip joint can remain stable throughout the entire range of motion, even with a single-axis hip joint. Therefore, the additional stability from a polycentric joint does not provide a large advantage in a PHP.

Polycentric hip joints can help with toe clearance during swing phase [55]. This same advantage is reported in polycentric knees [56]. However, in a comparison of 11 polycentric knees and 2 monocentric knees, one monocentric knee provided more ground clearance than 8 of the polycentric knees [53]. Therefore, a monocentric knee joint with proper alignment and swing phase control may generate greater ground clearance than a polycentric knee [53]. Similarly, an optimized hip design could provide adequate toe clearance without a polycentric joint. The PHP actuator can increase the hip angular velocity at the start of swing phase to cause increased knee flexion and, consequently, increased toe clearance.

Polycentric hip joints can also increase prosthetic hip maximum extension [55]. The PHP must reach a full range of normal extension so that the contralateral step length is not limited. A 20° extension criterion was selected to ensure that the PHP can achieve a full range of motion. If this requirement is attainable with a monocentric hip joint, then there is no need for any further extension that a polycentric joint may provide.

The main disadvantage of polycentric hip joints is that they are more complex and have more components than monocentric hip joints, which may produce a heavier system that is more

expensive and difficult to machine and assemble than a monocentric joint. Also, polycentric joints take up more space than monocentric joints.

Since most monocentric joint disadvantages can be mitigated with a microprocessor-controlled motor and appropriate design, and since polycentric joints have other disadvantages, a monocentric joint design was selected for the PHP.

4.3 Direct Drive System

The hip joint is mounted anteriorly, consistent with existing hip prostheses. This allows the user to sit while wearing the prosthesis. The simplest hip rotation solution would be to drive the hip directly from the motor. If the motor is placed at the hip joint, then the motor can rotate the leg around the hip center without additional components. This would be the simplest, lightest option with the fewest parts and assembly steps. But the Össur actuator has a 77 mm diameter, which would protrude too far anteriorly and would not fit comfortably under the user's pants (Figure 4-2, left). As such, the motor must be located inferiorly on the thigh, and a method of power transmission is needed to transmit the power to the hip (Figure 4-2, right). Four rotational power transfer methods were considered: gears, belts, chains, and pulleys. These methods are similar in that they all consist of a driving wheel and a driven wheel, but the medium of rotating the driven wheel varies.

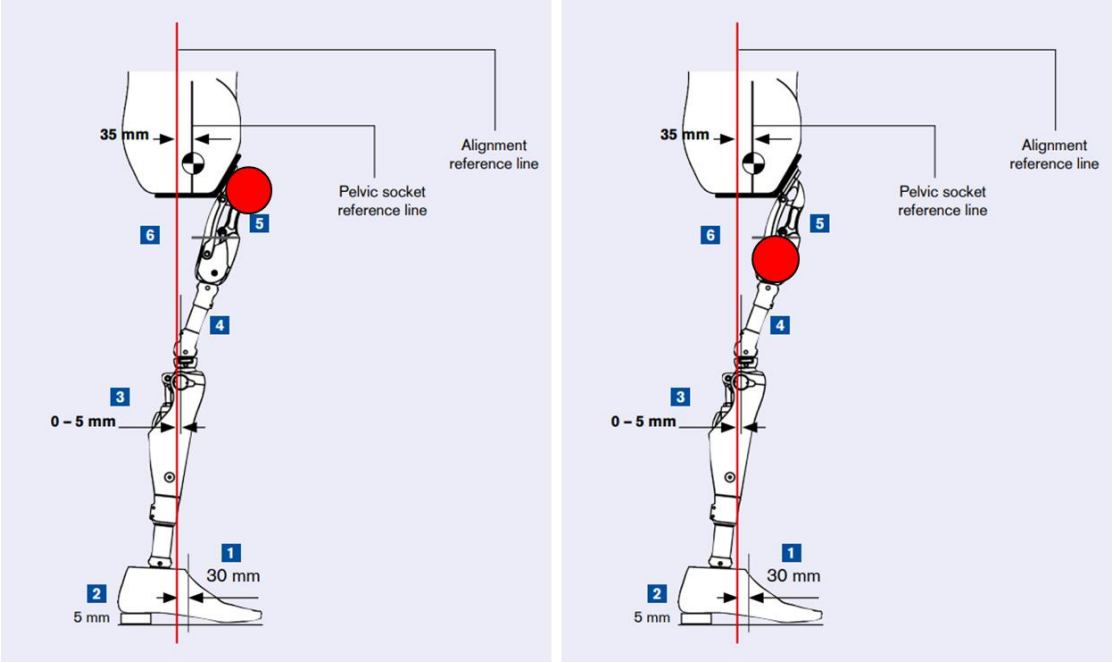

Figure 4-2 Left - red circle representing motor positioned at hip joint protrudes far anteriorly; Right - red circle representing motor positioned inferiorly on the thigh (Adapted from [58])

4.4 Gear Drive System

The first power transmission mechanism considered was a gear train. Gear systems use gear ratios to transmit rotational power and increase output torque or velocity. Gear drives consist of a driving gear, powered with an input torque, and a driven gear that is rotated by the driving gear. Gear systems may also contain one or more idler gears that are located between the driving and driven gears and transmit power between the two. Generally, in gear systems, the motor is fixed in place; however, for the PHP the top driven gear would be fixed and the motor would rotate the bottom gear, rotating the whole system about the top gear.

A gear ratio is the ratio of the number of driven gear teeth to the number of driving gear teeth. The driven gear torque and diameter are directly related to the gear ratio, and the angular velocity is inversely related to the gear ratio (Eq. 4-3), given by

$$Gear\ Ratio = \frac{n_2}{n_1} = \frac{\omega_1}{\omega_2} = \frac{d_2}{d_1} = \frac{T_2}{T_1} \qquad \text{(Eq. 4-1)}$$

where n_1 is the number of driving gear teeth, n_2 is the number of driven gear teeth, ω_1 is the driving gear angular velocity, ω_2 is the driven gear velocity, d_1 is the driving gear diameter, d_2 is the driven gear diameter, T_1 is the driving gear torque, and T_2 is the driven gear torque.

For the PHP, the maximum input torque is 96 Nm and the required hip torque is 96 Nm. Therefore, the minimum allowable gear ratio is minimum required output torque over maximum input torque, or $\frac{T_2}{T_1} = \frac{96\ Nm}{96\ Nm} = 1{:}\,1$. The actuator's maximum angular velocity is 300°/s and the hip angular velocity criterion is 150°/s, so the maximum allowable gear ratio is maximum input velocity over minimum required input velocity, or $\frac{\omega_1}{\omega_2} = \frac{300°/s}{150°/s} = 2{:}\,1$. Therefore, the PHP gear ratio must be between 1:1 and 2:1.

One limitation of a gear train is that an even number of gears are needed for the system to rotate. This is demonstrated in Figure 4-3. Starting with the input torque applied to the bottom gear, the resulting forces between the adjacent gears can be drawn to determine the reaction moment at the top gear, which is fixed to its shaft. In Figure 4-3 (A), the reaction moment M_3 is in the opposite direction of the input torque. **These two moments would counteract each other and the system would not rotate**. Contrarily, in Figure 4-3 (B), the reaction moment M_4 is in the same direction as the input torque. **This allows the system to rotate about the top shaft**. The same result occurs for any other number of even gears (allowing movement) and odd gears (not allowing movement). These results were confirmed with a SolidWorks simulation. When the simulated torque was applied to an even number gear, the simulated parts rotated. When the same torque was applied to an odd number gear, the system did not move.

Since an even number of gears is required, two-gear and four-gear systems were considered. The top of the motor must not pass above the lamination plate's bottom, to prevent interference in extension, and the top gear must not reach below the lamination plate, to allow the user to sit while wearing the prosthesis. Therefore, if using two gears, the bottom gear must be larger than the actuator, which has an outer diameter of 77 mm. Since the minimum gear ratio is 1:1, the driven gear must be at least the same size as the driving gear. 88 mm pitch diameter gears were used to satisfy these geometric constraints.

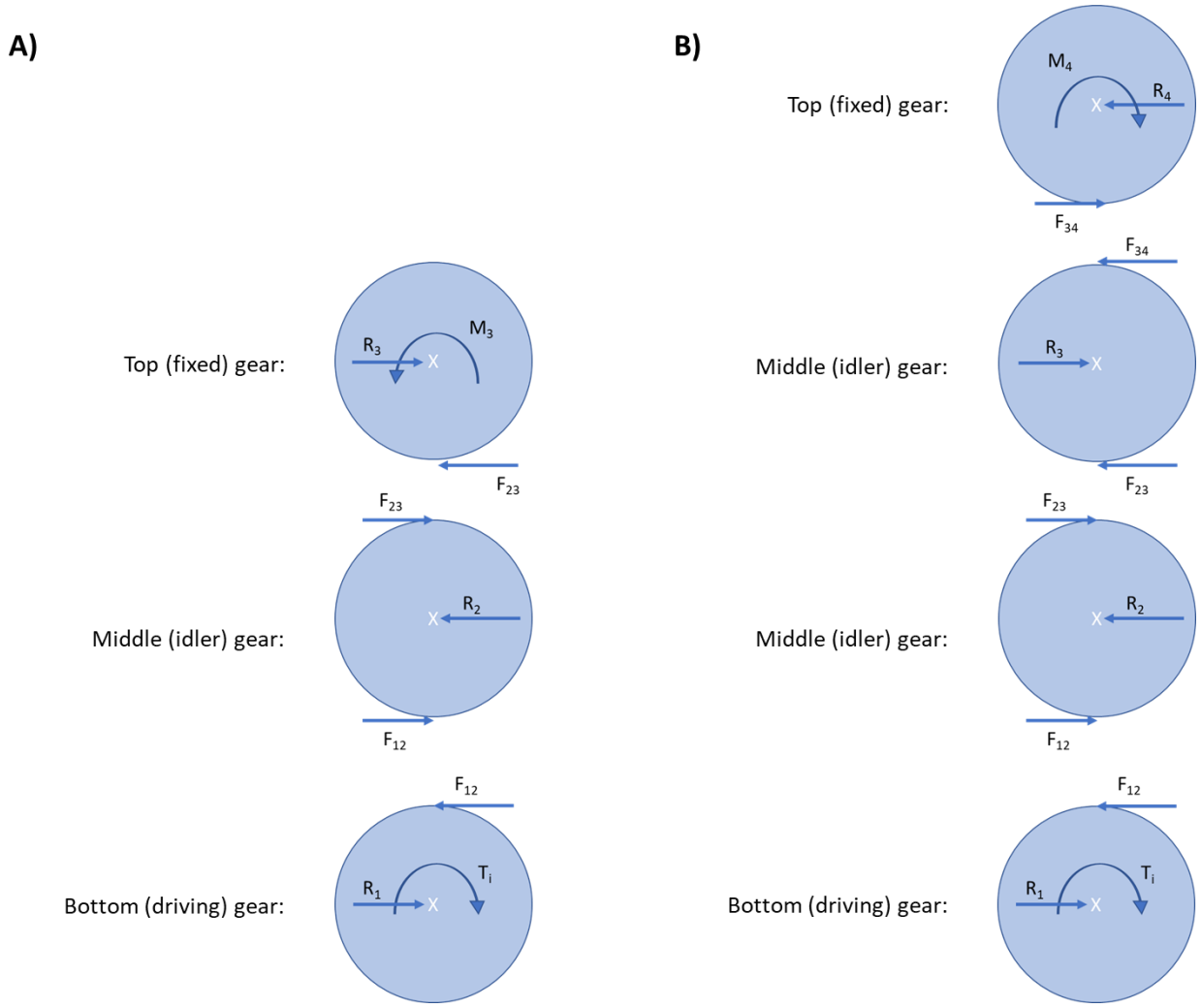

Figure 4-3 Free body diagrams of an odd-numbered gear system (A) and an even-numbered gear system (B) where R_1, R_2, R_3, and R_4 are the reaction forces at the gear shafts; F_{12}, F_{23}, and F_{34} are the forces between the gear teeth of the adjacent gears; T_i is the input torque applied from the motor to the driving gear; M_3 is the reaction moment at the fixed gear shaft for the three-gear system; and M_4 is the reaction moment at the fixed gear shaft for the four-gear system. In A, M_3 is in the opposite direction of T_i, so the system would not rotate. In B, M_4 is in the same direction as T_i, so the system would rotate.

An 88 mm gear would protrude too far anteriorly, similar to the direct drive system. However, the system will not be rotating 360°, so the gear's entire circumference would not be used. To reduce the anterior protrusion at the hip joint, the gears can be cut, as shown in Figure 4-4, to keep only the portion of the gears that will mesh with the other gear.

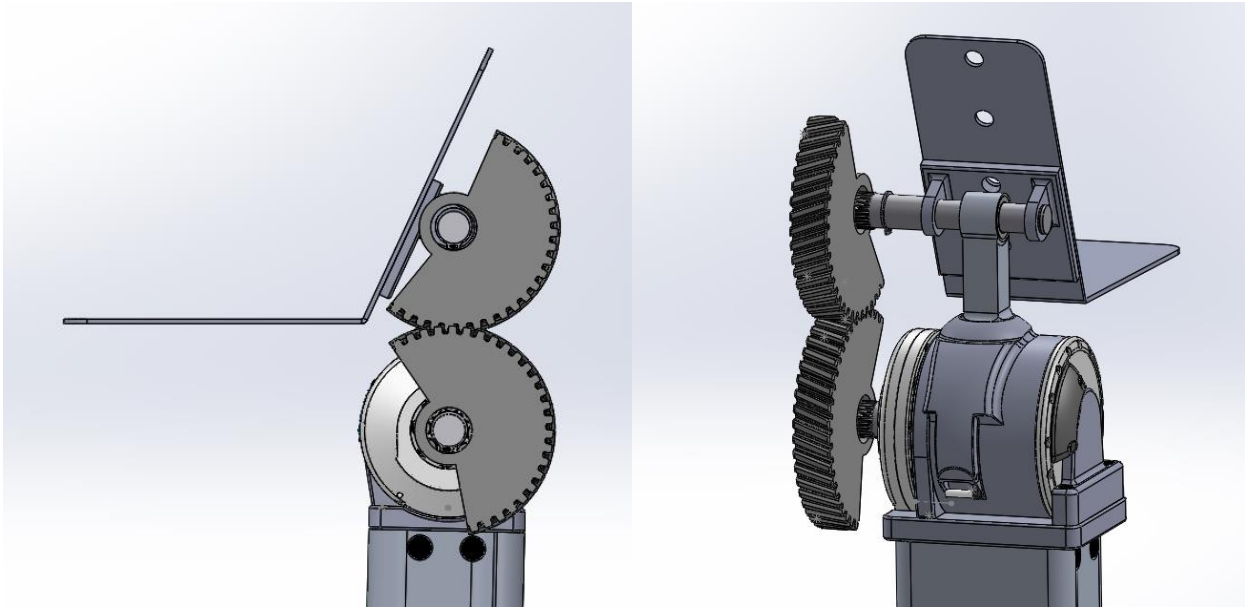

Figure 4-4 Gear train power transmission system with two partial 88 mm gears

Even with reduced size 88 mm gears, a 29 mm anterior protrusion from the top of the lamination plate remained (Figure 4-5). This protrusion exceeded the design criterion maximum of 20 mm anterior protrusion. Additionally, a casing would not be able to rotate around the modified gears, as demonstrated in Figure 4-6. A casing is required over moving parts to prevent finger traps for user safety.

Due to the anterior protrusion and the inability to create a cover for the gear system, the two-gear system was not a viable design option. The next smallest even number after two is four. A four-gear system would have a driving gear, two idler gears, and a driven gear. This setup requires additional plates on either side of the gears to support the idler gears (Figure 4-7). The gears in this power transmission system should be as small as possible to reduce the weight and PHP size. The top (driven) gear specifically must be small enough to meet the anterior protrusion criterion. A four-gear conceptual design was created using helical gears to provide more strength in a smaller volume and mass than spur gears. However, helical gears are more expensive and difficult to manufacture. The helical gear fatigue strength (Eq. 4-2) and bending stress (Eq. 4-3) were used to determine the smallest gear sizes that could withstand the motor torque.

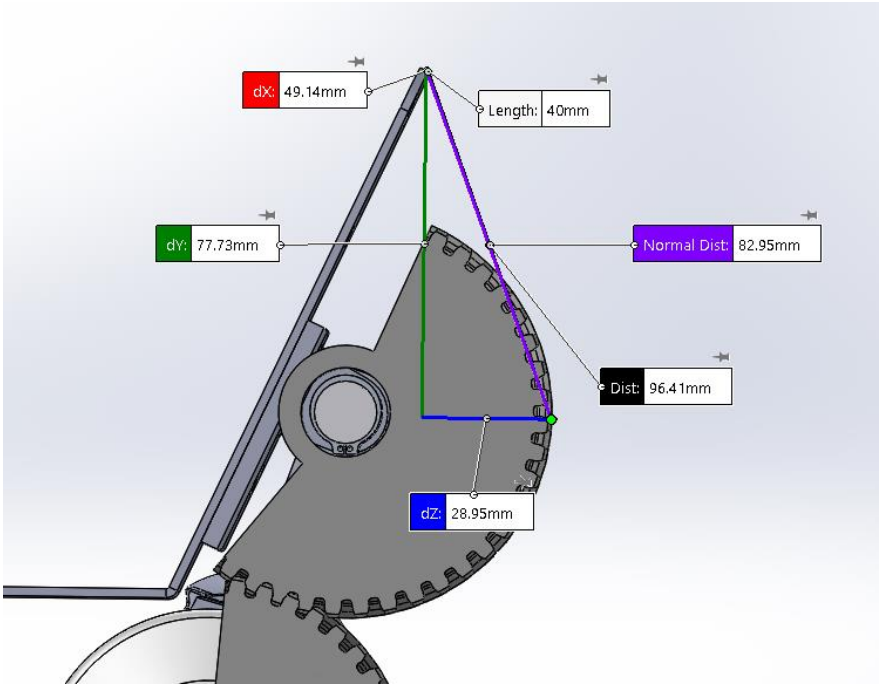

Figure 4-5 A partial 88 mm gear will protrude 29 mm anteriorly from the top of the lamination plate at the hip joint

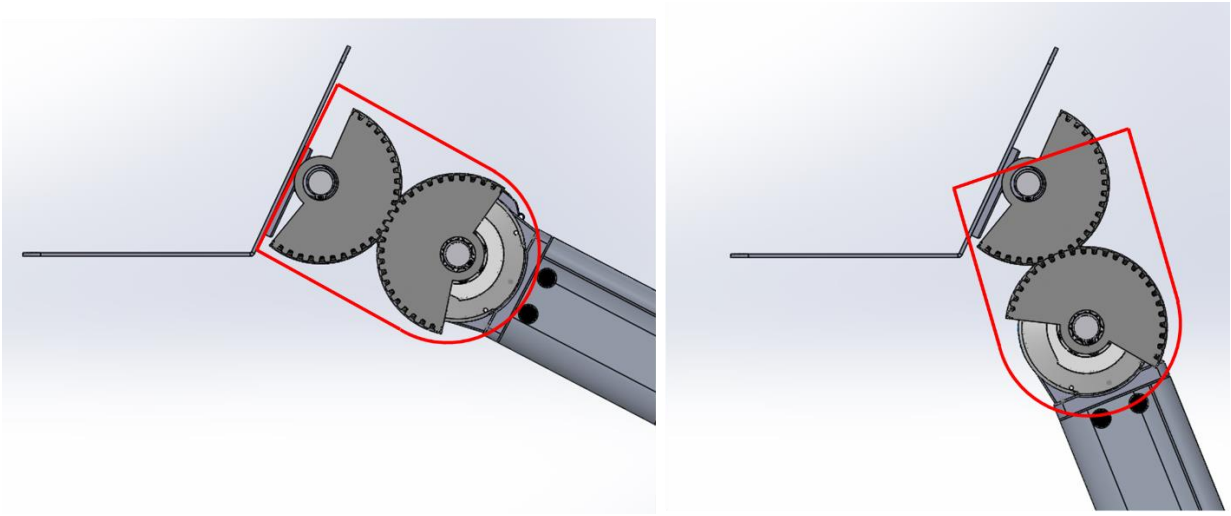

Figure 4-6 Theoretical casing shape would hit the socket when rotating around the modified gears

Fatigue strength [59] is given by

$$S_n = S'_n C_L G_G C_S k_r k_t k_{ms} \quad \text{(Eq. 4-2)}$$

where

S_n = fatigue strength

S'_n = standard R.R. Moore endurance limit = $0.5S_u$ for steel, where S_u is the ultimate tensile strength [59]

C_L = load factor = 1.0 for bending loads [59]

G_G = gradient factor = 1.0 for m < 5.08 [59]

C_S = surface factor = 0.61 for a machined steel part with S_u = 1448 MPa [60]

k_r = reliability factor = 0.814 for 99% reliability [59]

k_t = temperature factor = 1.0 for steel gears if temperature is less than 71.1°C [59]

k_{ms} = mean stress factor = 1.0 for idler gears and 1.4 for input and output gears [59]

The bending stress equation for helical gear teeth [61] is given by

$$\sigma = \frac{F_t}{mbJ} K_v K_o (0.93 K_m) \quad \text{(Eq. 4-3)}$$

where

σ = helical gear teeth bending stress

F_t = tangential force between gear teeth

m = module = pitch diameter in mm divided by number of teeth

b = gear face width

J = helical gear geometry factor based on helix angle and teeth in mating gear = 0.97 for helix angle 21.5, 40 teeth in mating gear [61]

K_v = velocity factor = 1 for pitch line approaching zero [59]

K_o = overload factor = 1.5 for power source light shock and driven machinery moderate shock [59]

K_m = mounting factor, reflecting the accuracy of mating gear alignment = 1.3 for accurate mountings for face widths between 0 mm and 50.8 mm [59]

Using Eq. 4-2, helical gears made with the high strength 17-4 PH stainless steel H900 had a fatigue strength of 359.5 MPa for idler gears and 503.3 MPa for driving and driven gears. The safety factor for helical gears fatigue is fatigue strength over bending stress. Using values from standard gear sizes, the smallest possible gear for the driven and driving gears with a safety factor greater or equal to 1.15 would have a 30mm diameter, 16mm width, and module (ratio of pitch diameter to number of teeth) of 2, resulting in a safety factor of 1.35 For the idler gears, the diameter must be at least 40mm to achieve an acceptable safety factor of 1.28. A conceptual design using these gears was created in SolidWorks (Figure 4-7).

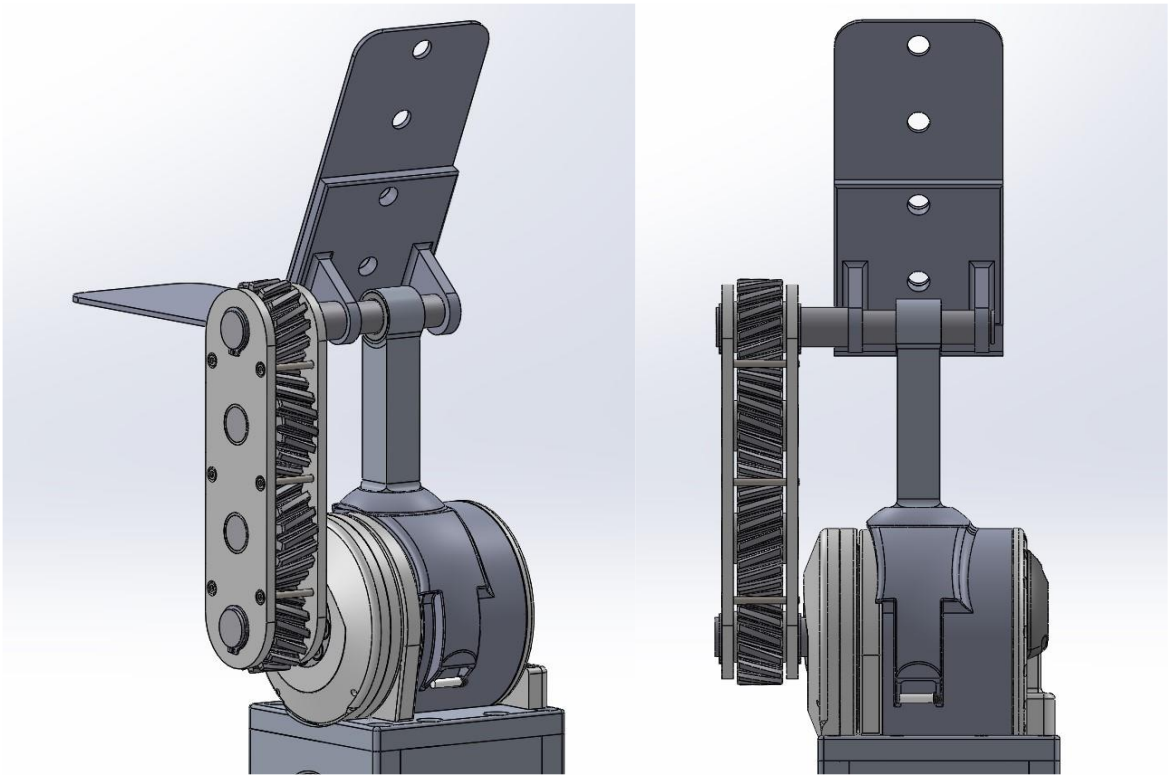

Figure 4-7 Four helical gears power transmission system conceptual design

In this SolidWorks model, the distance between the top and bottom shafts is 110mm. This distance exceeds the 96.5 mm design restriction between the motor's centre and the hip joint. The gears used in this conceptual design would also have to be custom-made because off-the-shelf gears use materials that are weaker than the 17-4PH stainless steel H900 used in the calculations. Ready-made gears would have to be even larger, thereby further surpassing the geometric design criteria. For these reasons, gears were not selected for the power transmission system.

4.5 Belt Drive System

The next power transmission method investigated used two pulleys and a timing belt. Belt systems can be open (Figure 4-8), where the belt remains straight between the two pulleys, or crossed (Figure 4-9), where the belt crosses over itself between the two pulleys. Like the gear system that would require an even number of gears to function, a crossed belt system would be required to transmit rotation in the PHP. In the open belt system (Figure 4-8), the input moment and reaction moment are in opposing directions, which prevents the system from rotating. In the crossed belt system (Figure 4-9), the moments are in the same direction, allowing the system to move. This applies to any pulley-type system – the tension mechanism will always have to be crossed.

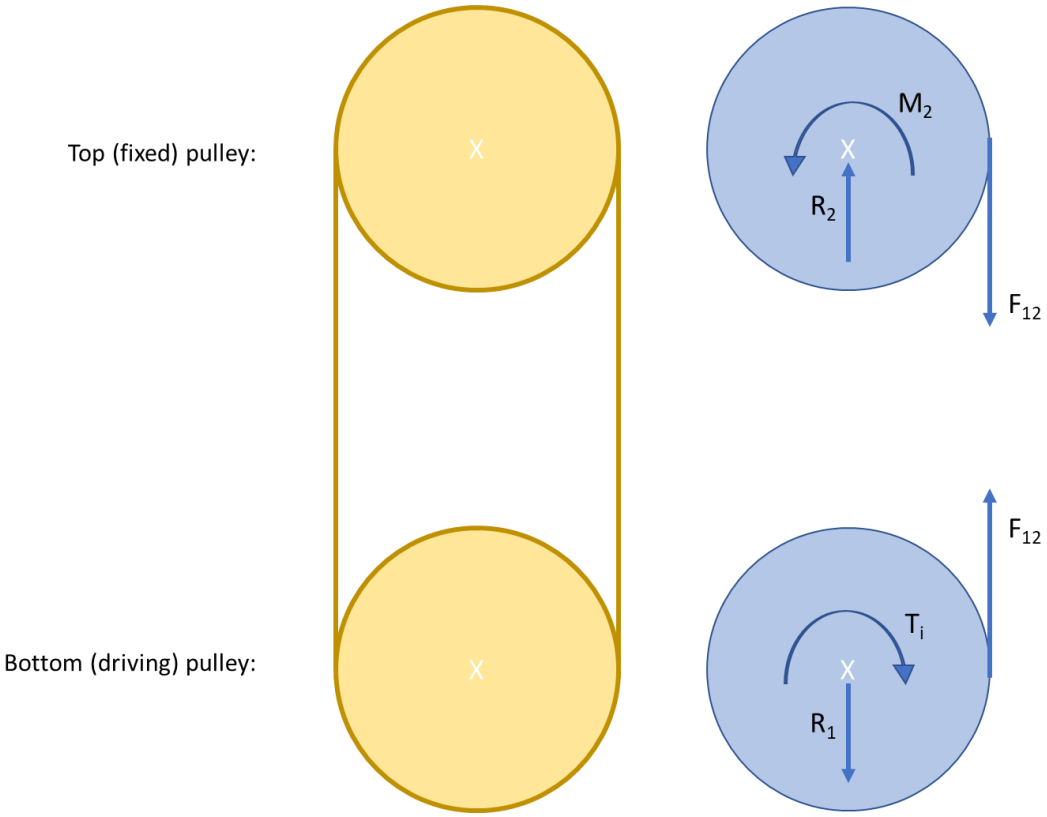

Figure 4-8 Diagram (left) and free body diagrams (right) of an open belt system, where R_1 and R_2 are the reaction forces between the pulleys and the shafts, F_{12} is the force from the belt pulling on the pulleys, T_i is the input torque from the motor acting on the driving pulley, and M_2 is the reaction moment at the fixed pulley shaft. M_2 is in the opposite direction of T_i, so the system would not rotate.

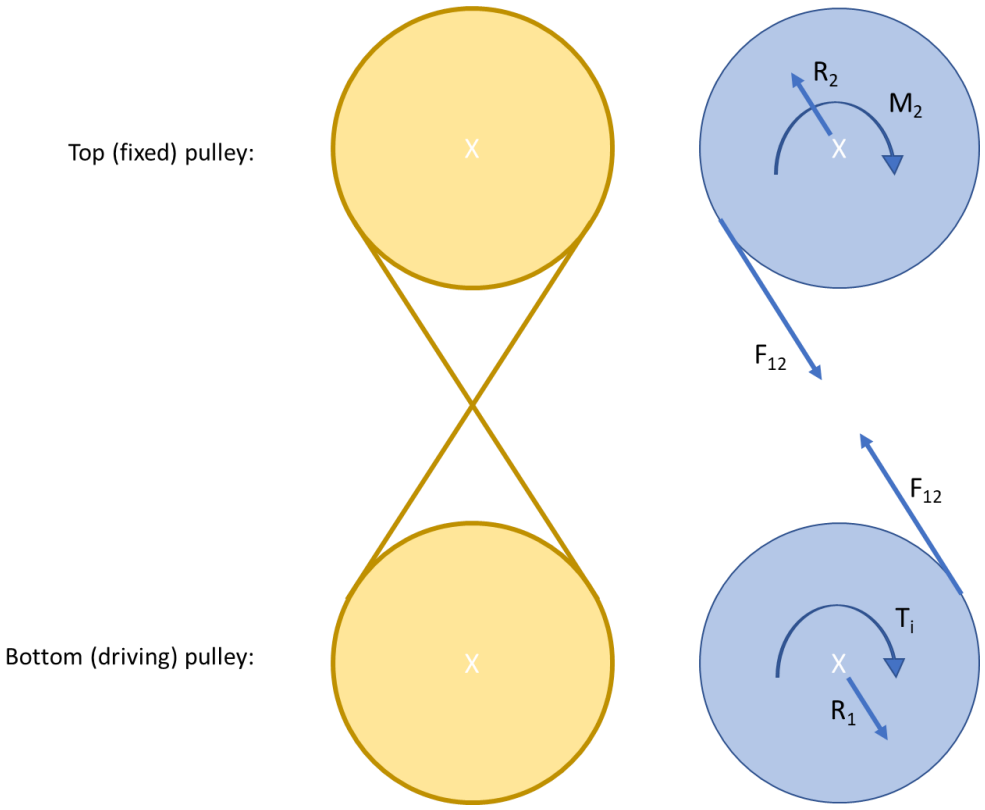

Figure 4-9 Diagram (left) and free body diagrams (right) of a crossed belt system, where R_1 and R_2 are the reaction forces between the pulleys and the shafts, F_{12} is the force from the belt pulling on the pulleys, T_i is the input torque from the motor acting on the driving pulley, and M_2 is the reaction moment at the fixed pulley shaft. M_2 is in the same direction as T_i, so the system would rotate.

To keep the anterior protrusion at the hip joint within the 20 mm limit outlined in the design criteria, the belt system's pulleys should have a diameter less than or equal to 50 mm. The tension force in the belt can be approximated using Eq. 4-4:

$$F = \frac{M}{r} \qquad \text{(Eq. 4-4)}$$

where F is the tension force in the belt, M is the maximum applied moment, and r is the pulley radius. Using a maximum motor torque of 96 Nm and a maximum pulley diameter of 50 mm, the belt must withstand 3840 N tension force.

Timing belts available from manufacturers did not satisfy this strength requirement within the geometric constraints. For example, an AT5 Redflex GEN III polyurethane steel-reinforced belt has a maximum allowable tensile strength of 911 N/(10 mm belt width) [62]. To achieve a tensile strength of 3840 N, the belt would need to be 42 mm wide. The 3840 N force estimation also did not take into account the pretension force that would be applied to the belt, so the belt

would likely need to be even wider. The first belt size available that satisfies this width requirement is 50 mm wide and operates with 60 mm wide pulleys. The belt system would be located on the actuator's lateral side; therefore, a power transmission system using the AT5 Redflex GEN III timing belt would surpass the maximum lateral protrusion design criterion.

The next smallest pitch in the GEN III series is the AT10 Redflex GEN III timing belt. The minimum number of pulley teeth for this belt is 15 [62], with a pitch diameter of 57.75 mm [62]. This is greater than the 50 mm diameter limit and will produce too much anterior protrusion. The other belts investigated from BRECOflex and other companies, including steel and Kevlar-reinforced belts, either required pulleys that were too large to fit at the hip joint or belt widths that created too much lateral protrusion. Thus, timing belts were not a feasible solution for the power transmission system.

4.6 Chain and Sprocket System

An alternative to a timing belt for the two pulleys was to use a chain as the tension mechanism. Like the belt drive, a chain would need to be crossed to cause rotation. Since chains are not as flexible as belts, this would be difficult to achieve. Instead, 2 chains could be used, one pulling in each direction, so that they can be crossed over each other.

For slow speeds, such as the PHP, the chains can be selected based on chain pull, which is equivalent to the torque divided by the pitch radius [63]. To ensure appropriate strength, the chain pull should not exceed 1/6 of the chain's tensile strength [63].

The first chain size considered was ASME 35-3. This chain has a 6300 lbs tensile strength [64], meaning that the chain pull must not exceed 1050 lbs or 4670 N. With a maximum torque of 96 Nm, the minimum pulley pitch diameter would be 41.1 mm. The smallest sprocket that meets this requirement has 14 teeth and an outer diameter of 47.5 mm [63], which would approach the anterior protrusion limit at the hip joint. The ASME 35-3 chain width is 1.36 inches or 34.54 mm [64]; so, with two chains the total width would be 69.08 mm. This width would cause the PHP design to surpass the lateral protrusion limit.

Other chain sizes with smaller widths have lower tensile strengths, meaning that the sprocket diameter would need to be even larger than for the ASME 35-3 chain. Since the diameter was already close to the maximum design criterion for ASME-35, these smaller chains will result

in too much anterior protrusion due to the larger sprockets. Therefore, it was concluded that a chain and sprocket system was not a suitable solution for the PHP power transmission system.

The chain and sprocket system was designed with the manufacturer's recommended design specification that chain pull does not exceed 1/6 of the chain's tensile strength [63]. However, lower safety factors were used in the PHP design so future work could reinvestigate chains as a power transmission option using a lower safety factor.

4.7 Pulley and Rope System

The final design candidate used a rope to transmit rotation between two sets of pulleys. Like belts and chains, the ropes had to be crossed to properly transfer power to the hip joint. Unlike timing belts and chains, ropes do not have grooves to mesh with the pulleys and instead rely on friction to not slip. To increase system stability, the ropes in the candidate design were anchored to the pulleys using loops on either end of the ropes, as seen in the 3D printed prototype in Figure 4-10. With this method of attachment, the rope can only provide tension in one direction; therefore, two ropes are needed, which cross over each other. The device shown in Figure 4-10 would also have another rope that crosses in the opposite direction to the one shown, providing tension for the other direction of rotation.

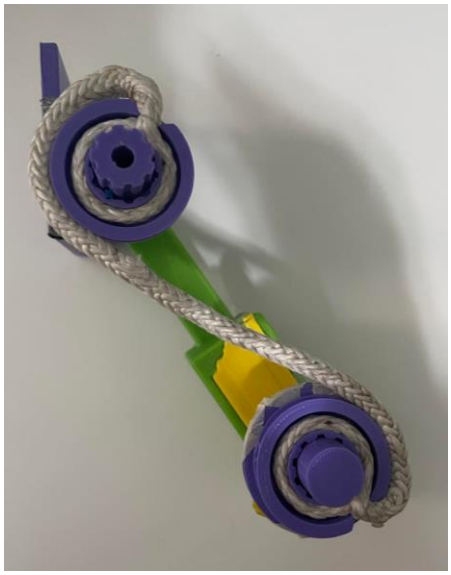

Figure 4-10 3D printed prototype of the rope and pulley design showing how the rope is anchored to the pulleys using loops on the ends

Polymer fibre ropes have high strength and low weight. For example, a 4 mm diameter Vectran rope has a breaking strength of 16,444 N. This means that the rope could withstand the maximum 96 Nm moment with pulleys as small as 11.7 mm in diameter. This is well within the maximum anterior protrusion design criterion. The width of the two 4 mm ropes would be 8 mm. Even accounting for the extra width of the pulleys, this should stay within the lateral protrusion limit. The pulley and rope design used 43 mm diameter pulleys (Figure 4-11).

Increasing the gear ratio would provide more torque at the hip, but the top pulley diameter could not be increased without creating too much anterior protrusion at the hip joint. Similarly, the bottom pulley diameter could not be decreased without decreasing the size of the bottom shaft, which had to be large enough for the keyway tensioning system (section 5.7). Therefore, a 1:1 gear ratio was used, which still fits within the design criteria.

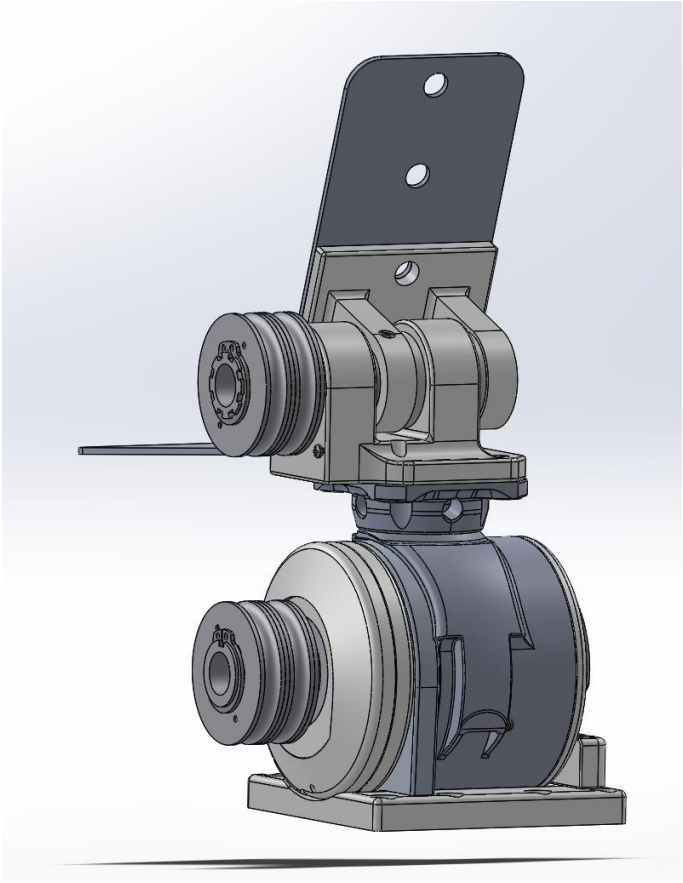

Figure 4-11 Pulley and rope system PHP design

To test the pulley and rope concept and the anchoring system, a prototype was 3D printed and tested with a servo motor (Figure 4-12). The bottom pulley was attached to the servo motor

and when the servo motor rotated, the 3D-printed device successfully rotated about the hip joint, as designed. With the successful prototype, the rope and pulley power transmission system was selected for the final PHP design.

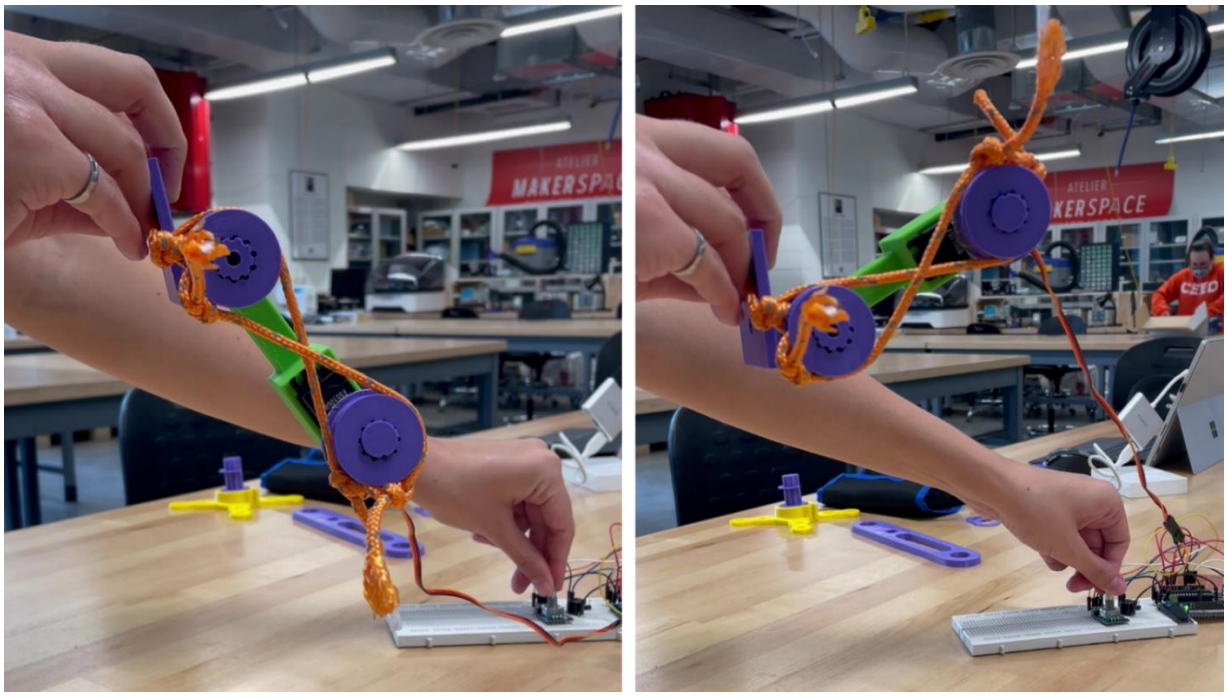

Figure 4-12 The 3D printed pulley design proof-of-concept prototype successfully rotated about the hip joint when powered with a servo motor

Chapter 5: Power Hip Prosthesis Design and Components

This chapter describes the final PHP design (Figure 5-1) and explains the function of each component.

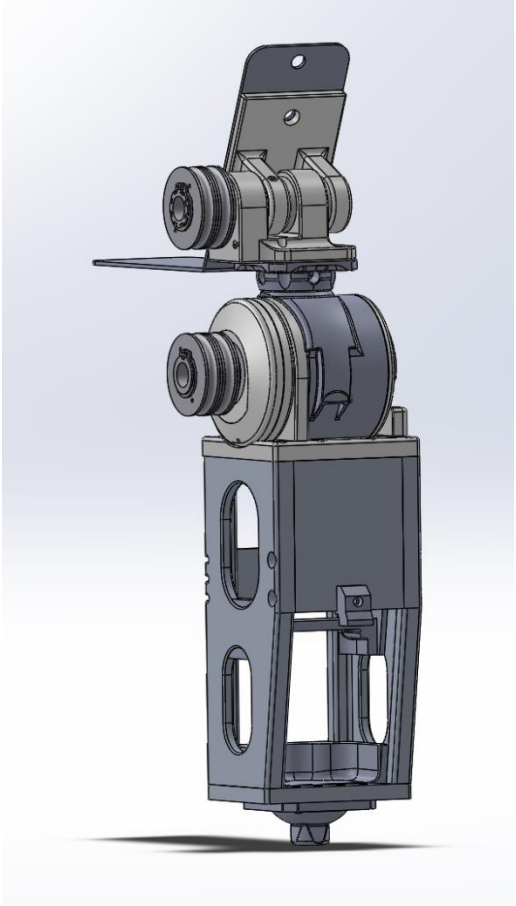

Figure 5-1 Final PHP design

The final PHP design uses two sets of pulleys and two ropes. The top shaft is fixed and the pulleys on the top do not rotate. The bottom shaft and pulleys rotate with the motor, which pulls on the ropes and drives the prosthetic leg to rotate about the top shaft.

5.1 Actuator

PHP power comes from an actuator (Figure 5-2) developed by Össur for their Power Knee and was modified for the PHP design. The first change made to the motor was to remove the lever arm from the actuator's lateral end component (Figure 5-3). Next, an additional set of threaded holes was added to the motor housing (Figure 5-4), so that the housing can be fixed to the

attachment ring (section 5.11). The medial end piece and the grey bearing seen in Figure 5-2 were also both removed.

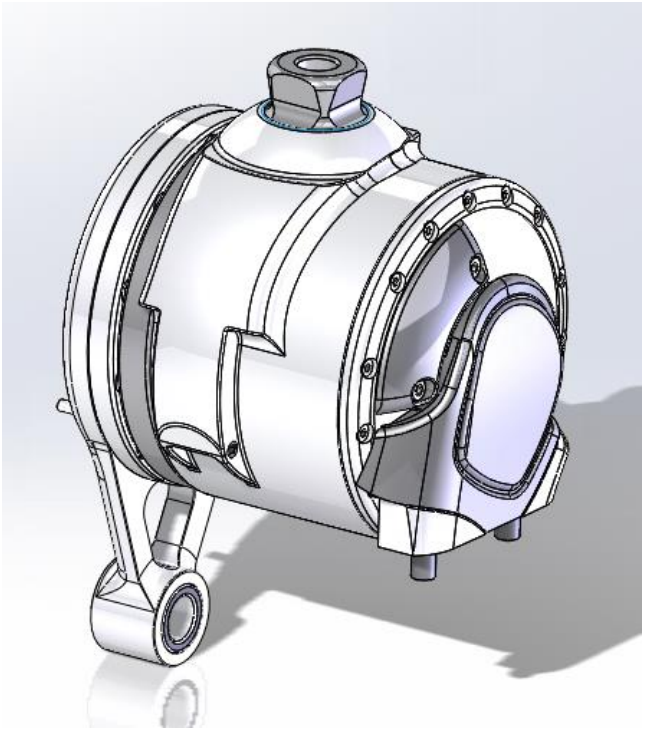

Figure 5-2 Power knee actuator used in the PHP

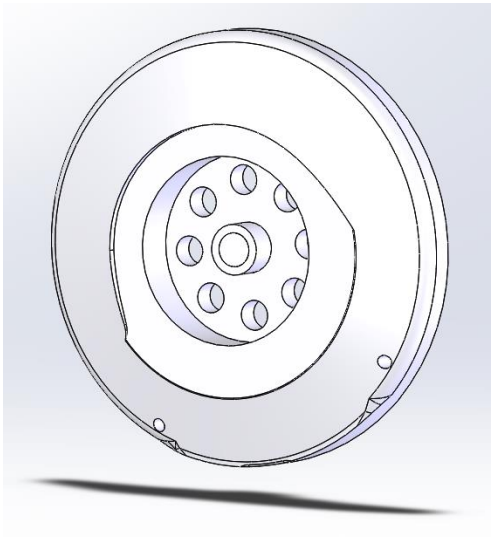

Figure 5-3 Actuator lateral component with the lever arm removed

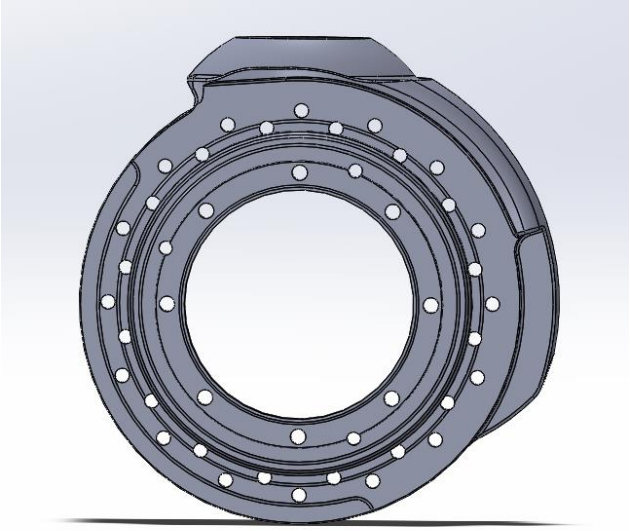

Figure 5-4 Motor housing with additional set of threaded holes

The actuator features a male pyramid adapter on the top, which was used by the power knee to connect to the user's thigh. In the PHP design, this pyramid adapter is used to connect the actuator to the bearing housing that rotates about the top shaft.

5.2 Rope

A high-strength fibre was needed for the rope to withstand the large tension forces caused by power transmission. Six materials were considered: polypropylene, high molecular weight polyethylene (HMPE), polybenzobisoxazole (PBO), liquid crystal polymer (LCP), polyester, and polyamide. These high-strength fibres are often used in sailing [65]. Of these six fibres, the three strongest are HMPE, PBO, and LCP. The three weaker fibres would require a thicker rope, which would necessitate wider pulleys and increase PHP lateral protrusion. The strongest of the six fibres is PBO, with a breaking strength of 78.4 kN for an 8 mm diameter [65]. PBO also has the lowest elongation at 50% breaking strength, only stretching 1.8% [65]. However, PBO has poor abrasion and UV resistance [66]. Though UV exposure can be reduced with a cover, abrasion resistance is important in the PHP since the ropes repeatedly rub against the pulleys.

Of the remaining fibres, LCP has the lowest stretch with a 2.2% elongation at 50% breaking strength [65]. HMPE is slightly stronger than LCP, but LCP has better abrasion resistance, tenacity, and lower creep than HMPE [65], [67]. LCP exhibits no creep under loads up to 50% of its breaking strength [68]. For these reasons, Vectran LCP was selected as the PHP rope material.

Unlike timing belts and chains that have grooves and teeth to transfer power, rope and pulley systems usually rely on friction. To make the system more secure and prevent slippage, the PHP ropes are anchored to the pulleys. Two ropes are used, each pulling in opposite directions. Both ropes have a loop on each end, that slips around the pulley's center to anchor the rope and allow separate tensioning. The ropes loop around the pulley's centre, exit through a hole, and wrap around the pulley.

Figure 5-5 PHP rope with a loop on each end

Figure 5-6 PHP ropes have loops that are anchored around the axle. The ropes exit through a hole in the pulley then wrap around the pulleys.

The rope loops were created with eye splices (Figure 5-7). These splices are made by looping the rope back on itself and intertwining the loose end into the rope [69]. Eye splices retain the highest breaking strength of all end connections, and generally maintain 100% of the rope strength [70]–[72]. They are also commonly used while determining rope breaking strengths, so the spliced ropes should be as strong as the breaking strength listed on the manufacturer's website [70]–[72].

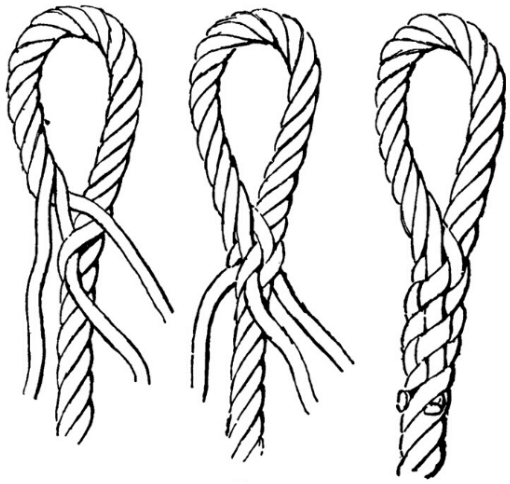

Figure 5-7 Eye splice made by intertwining the loose ends of a rope back into itself (Adapted from [69])

5.3 Pulley

The PHP pulleys were designed to allow the rope to anchor inside the part, to prevent slipping. The rope loop fits around a groove on the inside of the pulley (Figure 5-8) and a hole on the top allows the rope to stick out and wrap around the pulley.

The pulleys have multiple keyways that allow the assembler to adjust the pulley position relative to the shafts and create tension in the ropes. This tensioning system is discussed in greater detail in section 5.7.

Figure 5-8 PHP pulley design

5.4 Side Plate

Each pulley has an accompanying side plate (Figure 5-9). These side plates serve two purposes, to enclose the pulley groove so that the rope will not be able to slip out and to support the pulleys when they are placed under load. The rope groove in the pulley acts as a cantilever beam because the groove is not supported on one end. To compensate for this, the side plates have an extended portion that fits into the side of the pulley and supports the hanging end of the pulley groove (Figure 5-10).

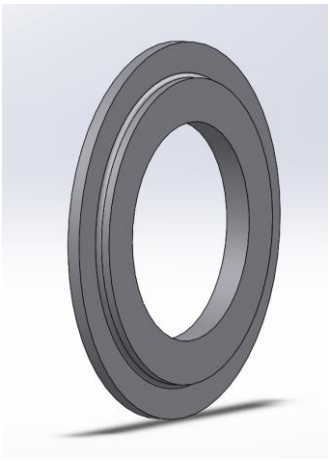

Figure 5-9 PHP side plate design that accompanies each pulley

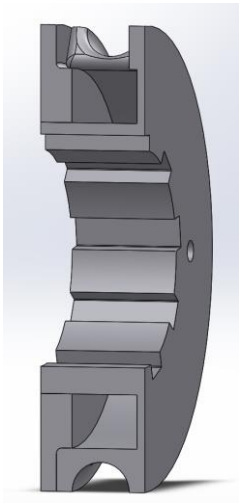

Figure 5-10 Section view of the PHP pulley and side plate assembly

5.5 Bottom Shaft

The PHP bottom shaft (Figure 5-11) rotates with the actuator to input torque to the bottom pulleys. The actuator has an eight-bolt pattern on the lateral side (Figure 5-12) that is used to transmit rotation to the bottom shaft. The medial end of the bottom shaft features eight indentations that fit over the bolt heads (Figure 5-13) so that when the shaft is inserted over the bolt pattern, the bolt heads transmit motion from the actuator to the shaft.

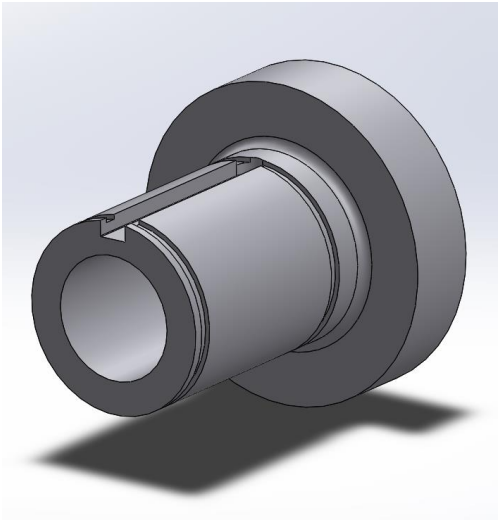

Figure 5-11 PHP bottom shaft design

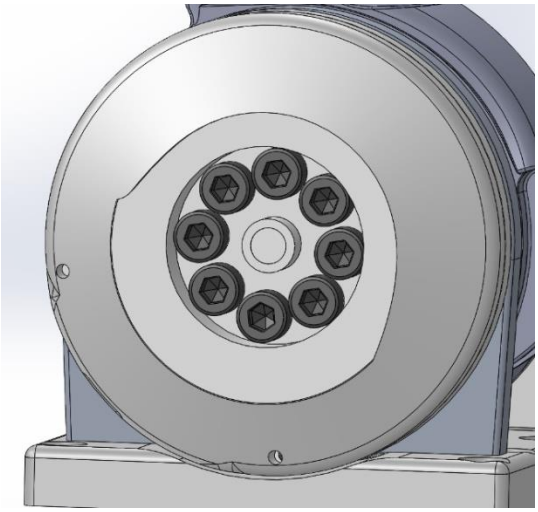

Figure 5-12 Bolt pattern on the lateral side of the actuator

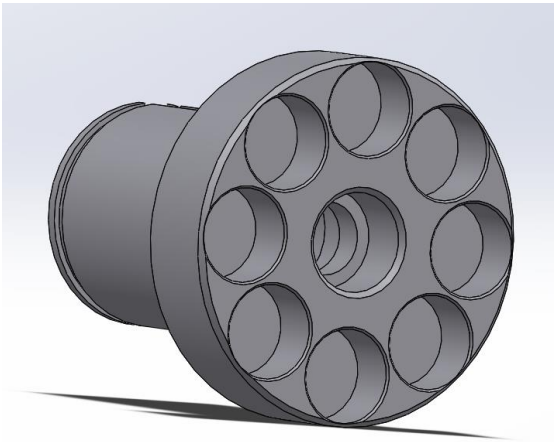

Figure 5-13 Indentations on the bottom shaft's medial end that fit over the actuator bolt pattern

The bottom shaft is secured in place medially/laterally with a screw that goes through the middle of the shaft and into the centre of the actuator (Figure 5-14). The shaft also has a keyway to prevent pulley rotation relative to the shaft and two grooves for external retaining rings that hold the pulleys in place along the shaft.

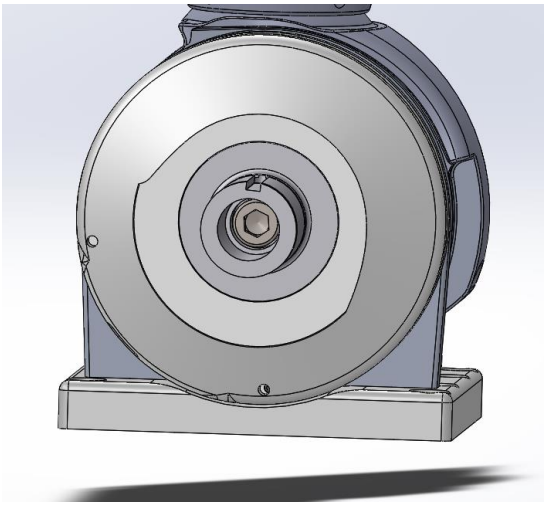

Figure 5-14 The bottom shaft is secured to the actuator with a screw

5.6 Top shaft

The top shaft is fixed to the top hinge (section 5.8) using a coiled spring pin. The top shaft features eight keyways (Figure 5-15) that allow the assembler to adjust the pulley position to create

tension, as explained further in section 5.7. The shaft also features two grooves for external retaining rings that hold the pulleys in place medially/laterally.

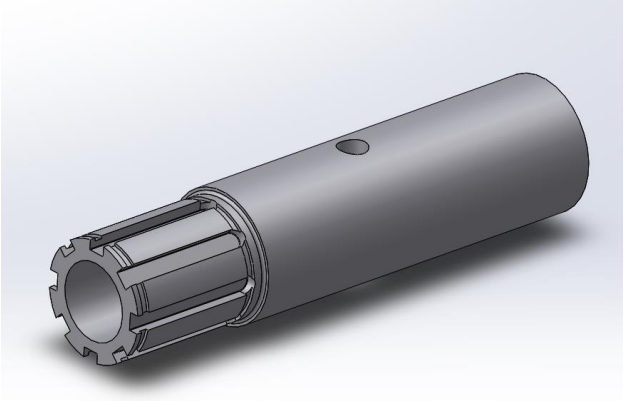

Figure 5-15 PHP top shaft featuring eight keyways and a hole for a coiled spring pin

5.7 Tensioning System

Instead of adding additional components to provide tension to the pulley system, a tensioning method was devised at the shafts to reduce the number of components and system weight. Two ropes are on separate pulleys so that the pulleys can be tensioned in opposite directions. To assemble the PHP, the first pulley is placed on the bottom shaft with the rope already in place and is fixed to the shaft with a key. The other pulley for that rope is then placed onto the top shaft. The pulley is rotated as far as possible, then the key is inserted into whichever pair of pulley keyway and shaft keyway align best.

The pulleys and top shaft have different numbers of keyways to provide a larger number of positions. The pulleys have nine keyways, and the top shaft has eight, resulting in 72 possible positions for the top pulley (Figure 5-16). With an available position every 5°, the maximum possible slack that will occur in the rope is 1.88 mm. This should result in minimal backlash when the leg changes directions, which should not be noticeable to the user. The other set of rope and pulleys is tensioned in the same way but in the opposite direction. The pulleys have two small holes so that an angle grinder wrench can be used to apply tension before inserting the key.

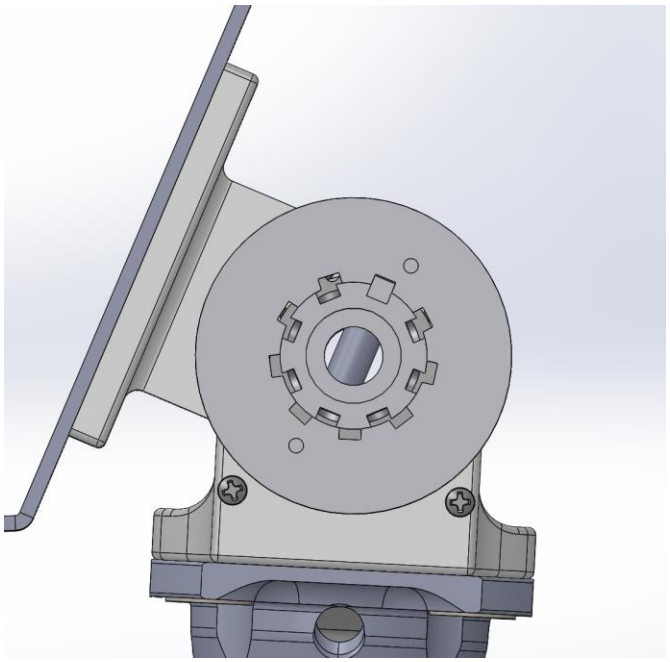

Figure 5-16 PHP tensioning system with 8 keyways in the shaft and 9 keyways in the pulley

The same system could have been accomplished using splines in both the pulley and the shaft, but splines are more difficult and costly to manufacture.

5.8 Lamination Plate and Top Hinge

The lamination plate (Figure 5-17) is embedded into the prosthetic socket and provides support to anchor the hip joint. The top hinge (Figure 5-18) is screwed into the lamination plate and hip socket and is used to hold the top shaft. One arm of the hinge has a hole for the coiled spring pin to prevent rotation between the top shaft and the hinge.

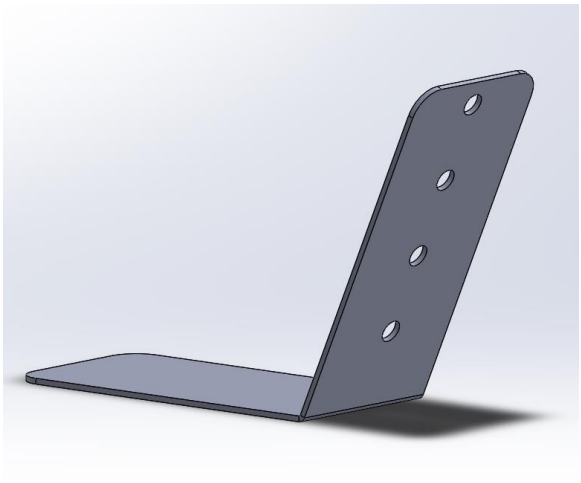

Figure 5-17 PHP lamination plate

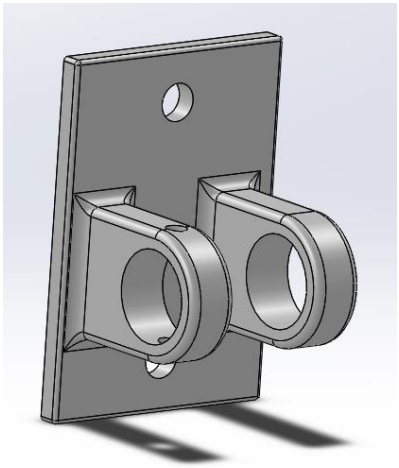

Figure 5-18 PHP top hinge

5.9 Bearings and Bearing Housing

The PHP must rotate about the top hinge. Bearings were used to reduce friction. Needle roller bearings were selected because the bearings will face high radial loads and low axial loads. The bearings are press-fit into the bearing housing (Figure 5-19). A four-hole female pyramid adapter is screwed onto the bottom of the bearing housing (Figure 5-20) so that it can be connected to the actuator's male pyramid adapter. The top shaft slides through the bearing housing and the top hinge, with two polytetrafluoroethylene (PTFE) spacers keeping the bearing housing in place medially/laterally. PTFE spacers were selected because they provide a low-friction surface and prevent the metal parts from rubbing against each other.

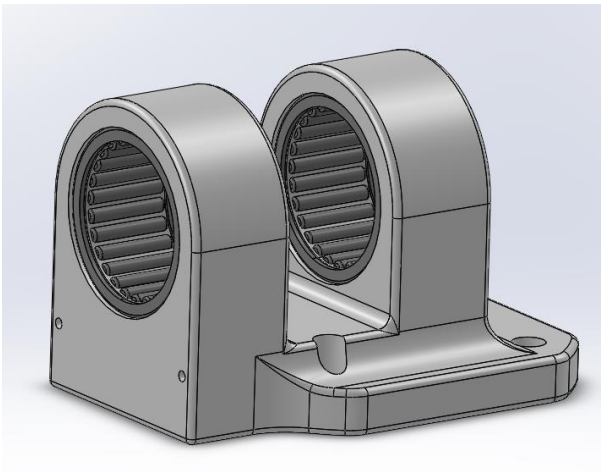

Figure 5-19 Needle roller bearings press fit into the bearing housing

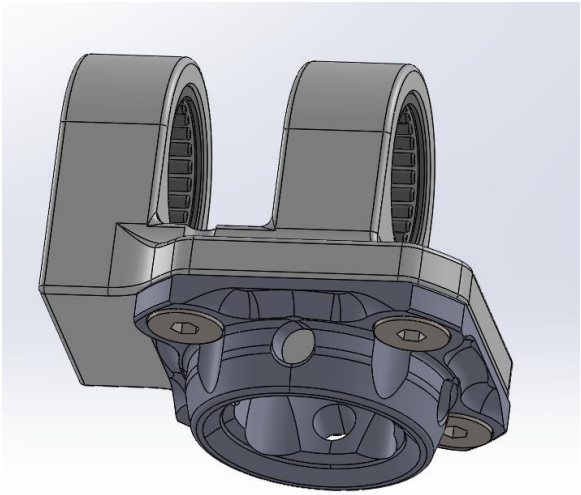

Figure 5-20 A four-hole female pyramid adapter is screwed into the bottom of the bearing housing and connects to the male pyramid adapter on the actuator

5.10 Attachment Plate

The attachment plate (Figure 5-21) is used to connect the actuator to the electronics chassis (section 5.14). The groove in the attachment plate creates clearance between the plate and the motor components, allowing the motor to rotate and avoiding tight tolerances between the two parts. The motor is secured to the attachment plate with the attachment ring (section 5.11) and the medial attachment piece (section 5.12). The attachment plate is then screwed into the top of the electronics chassis.

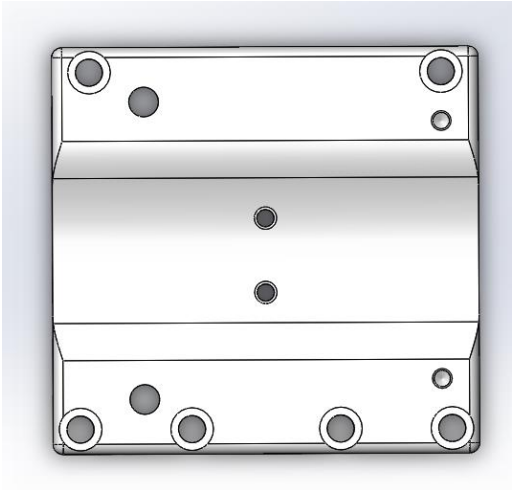

Figure 5-21 PHP attachment plate

5.11 Attachment Ring

The attachment ring is used to secure the actuator to the attachment plate and prevent the motor housing from rotating. The ring features two threaded holes on the bottom so that screws can be inserted through the attachment plate into the ring, securing the two together. The attachment ring also features 16 clearance holes that align with the threaded holes in the motor housing. Screws are used to secure the attachment ring to the motor housing and prevent rotation between the two parts (Figure 5-22).

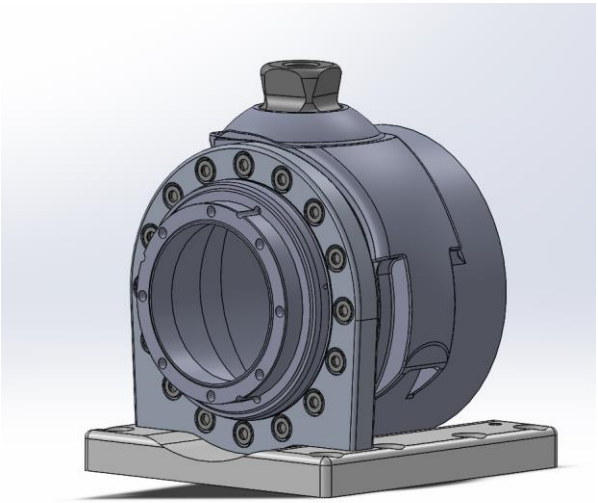

Figure 5-22 PHP attachment ring secured to the attachment plate and screwed into the motor housing

5.12 Medial Attachment Piece

The medial attachment piece fits into the PHP medial end and is screwed into the attachment plate (Figure 5-23). An O-ring was placed around the medial attachment piece where it interfaces with the motor (Figure 5-24), to avoid tight tolerances on the medial attachment piece and to help absorb shocks. The medial attachment piece helps to secure the motor to the attachment plate but does not prevent rotation.

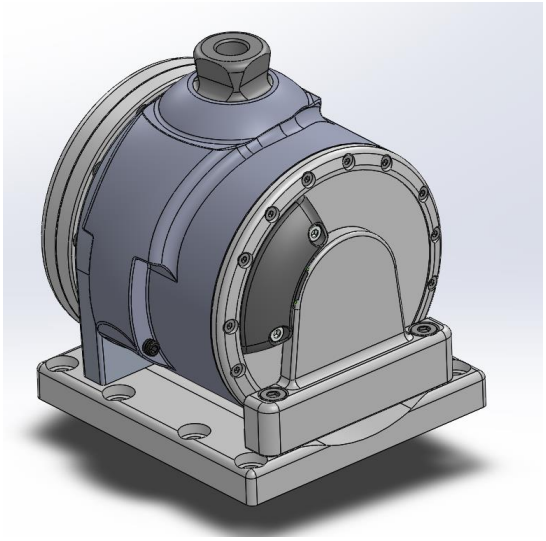

Figure 5-23 PHP medial attachment piece inserted into the actuator's medial end and screwed into the attachment plate

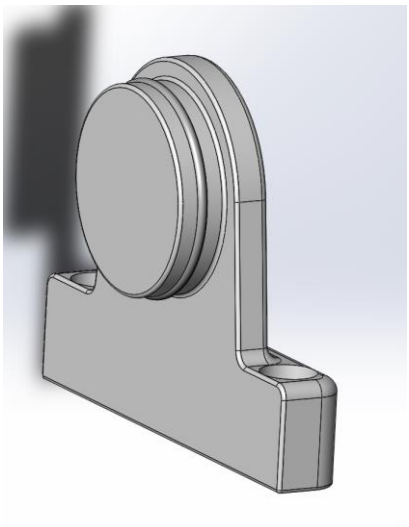

Figure 5-24 Medial attachment piece with O-ring around extrusion that interfaces with the motor

5.13 Casing

A plastic casing covers the pulleys to prevent finger traps (Figure 5-25). The casing back piece slides onto the shafts first before the pulleys. Once the pulleys have been secured onto the shafts, the top casing piece slides over using grooves that connect the casing pieces (Figure 5-26). Finally, the bottom casing piece slides into place, completely enclosing the pulleys (Figure 5-27).

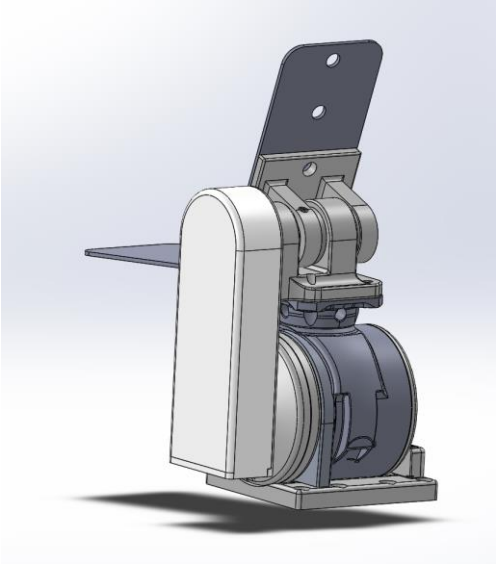

Figure 5-25 PHP casing covering the pulleys

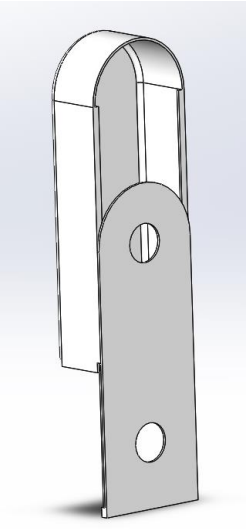

Figure 5-26 PHP casing top piece sliding onto the casing back piece

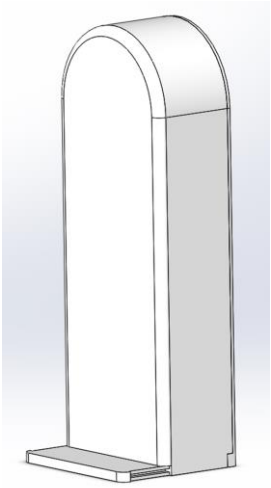

Figure 5-27 Bottom casing piece sliding into place to enclose the pulleys

5.14 Electronics Chassis

The electronics chassis (Figure 5-28), designed by colleagues, houses the PHP battery and other electronic components. It also features strain gauges used for the PHP control system. The attachment plate screws into the top of the electronics chassis. The chassis is connected to the knee with a height-adjustable pylon.

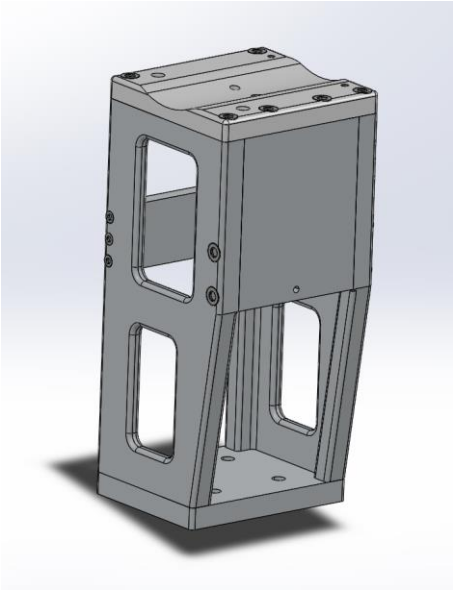

Figure 5-28 Electronics chassis with the attachment plate connected on top

Chapter 6: Failure Analysis

This chapter describes the stress analysis conducted prior to PHP machining. Calculations and FEA were used to verify that the PHP can sustain static and cyclical loads per ISO 15032:2000 and transmit the 96 Nm maximum torque from the motor without failure.

Except for the off-the-shelf parts like screws and retaining rings, all metal PHP components were made with aluminum 2024-T4 or 17-4 PH stainless steel. Aluminum was used as much as possible because it is lighter than stainless steel, but steel was needed for parts requiring more strength. Mechanical properties are summarized in Table 6-1 and were used in the calculations in this chapter.

Table 6-1 Mechanical properties of metals used for the PHP components

Material	**Ultimate Tensile Strength (MPa)**	**Yield Strength (MPa)**	**Density (kg/m^3)**
17-4 PH Stainless Steel H900 [73]	1448	1379	7800
Aluminum 2024-T4 [74]	469	324	2780

6.1 Rope Analysis

The tension force exerted on the rope can be calculated with Eq. 4-4. For a 96 Nm maximum moment and a 21.5 mm pulley radius, the rope must sustain a 4465 N force. The 12-strand Vectran 3 mm rope break load is 993 kg or 9741 N [75]. Therefore, the rope safety factor is 2.2 and the rope will not break.

Vectran experiences no creep under loads below 50% of its breaking load [68]. Half the breaking load is 4871 N, which is greater than the 4465 N tension force. Therefore, the rope will not experience creep, which means that slack will not be introduced into the system over time and the pulleys will not require continual adjustment.

6.2 Knee Analysis

The knee is not part of the PHP design, so no stress analysis was performed on the knee. However, the ISO test loads are applied at the knee joint, so a knee free body diagram (FBD)

(Figure 6-1) was used to determine the resultant forces that would be transmitted from the knee to the rest of the PHP. ISO 15032:2000 specifies four test loading conditions for the PHP: a medial-lateral (M-L) static load test, an M-L cyclical load test, an anterior-posterior (A-P) static load test, and an A-P cyclical load test. Figure 6-1 features the frontal plane knee FBD used for the M-L test cases, where y is the anterior direction, and x is the medial direction. The applied test force, F_{test}, was varied according to the test condition being analyzed.

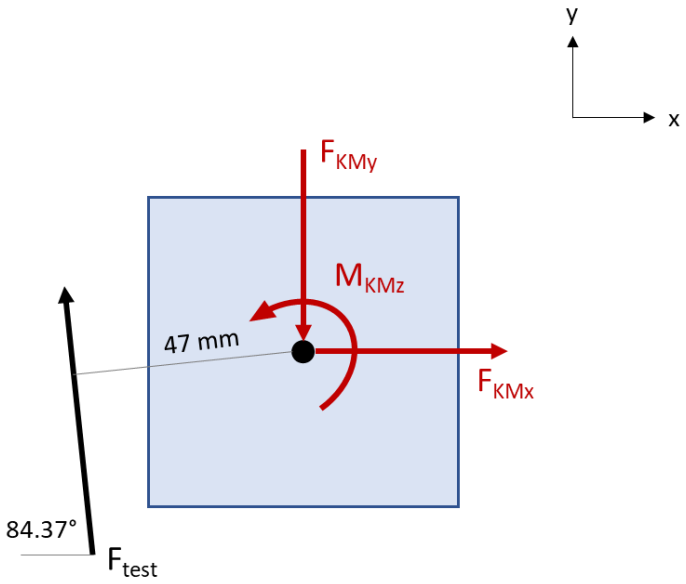

Figure 6-1 Knee frontal plane FBD, where F_{test} is the test force specified by the ISO standard, F_{KMx} is the force between the knee and the motor in the x direction, F_{KMy} is the force between the knee and the motor in the y direction, and M_{KMz} is the moment between the knee and the motor about the z-axis. Known forces are depicted in black and unknown forces are depicted in red.

The resultant forces F_{KMx} and F_{KMy} and the resultant moment M_{KMz} were calculated using the sum of forces in the x direction (Eq. 6-1), sum of forces in the y direction (Eq. 6-2), and sum of moments about the z-axis (Eq. 6-3):

$$\sum F_x = 0 \qquad \text{(Eq. 6-1)}$$

$$\sum F_x = F_{KMx} - F_{test} * \cos(84.37) = 0$$

$$\sum F_y = 0 \qquad \text{(Eq. 6-2)}$$

$$\sum F_y = F_{test} * \sin(84.37) - F_{KMy} = 0$$

$$\sum M_z = 0 \qquad \text{(Eq. 6-3)}$$

$$\sum M_z = M_{KMz} - F_{test} * 0.047 = 0$$

Using Newton's third law, the reaction forces were then applied to the motor FBD. Eq. 6-1, Eq. 6-2, and Eq. 6-3 were used to solve the unknown forces in each of the parts' FBDs.

6.3 Bottom Shaft Analysis

The bottom shaft is made of 17-4 PH Stainless Steel H900. The shafts must sustain both the maximum static force and the cyclical forces from the ISO standard, as well as the actuator torque. Stress along the shaft is a combination of bending and torsional stresses. Since the axial loads are small compared to the bending and torsion loads, axial loads were omitted from the stress analysis [76]. An FBD (Figure 6-2) was used to determine the bottom shaft forces in the frontal plane.

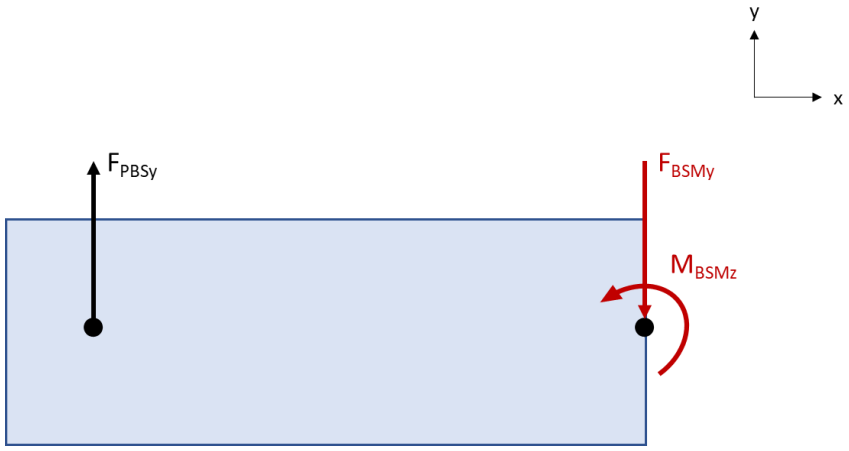

Figure 6-2 Bottom shaft frontal plane FBD, where F_{PBSy} is the force between the pulley and the bottom shaft in the y direction, F_{BSMy} is the force between the bottom shaft and the motor in the y direction, and M_{BSMz} is the moment between the bottom shaft and the motor about the z-axis. Known forces are depicted in black and unknown forces are depicted in red.

The force from the rope was added to the bottom shaft FBD in the lateral pulley location, and Eq. 6-1 to Eq. 6-3 were used to calculate the reaction forces at the interface with the motor. The forces in the y direction were then used to create a shear force diagram (Figure 6-3) and a

bending moment diagram (Figure 6-4) for the M-L static load case. A torque diagram is also presented in Figure 6-5.

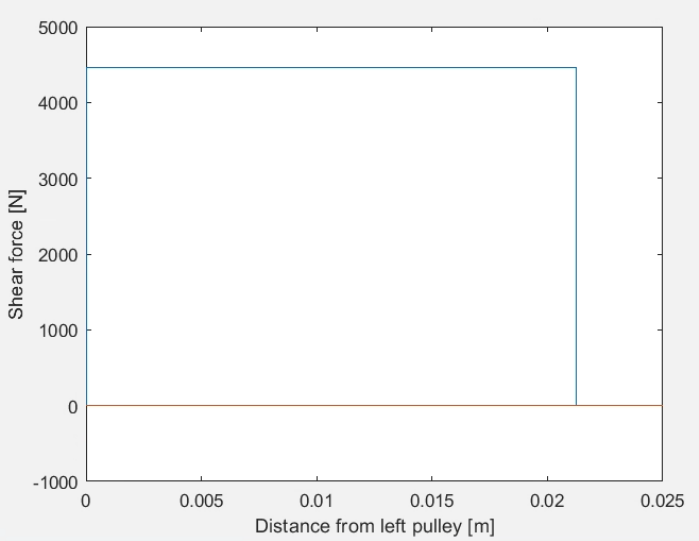

Figure 6-3 Bottom shaft M-L static load shear force diagram

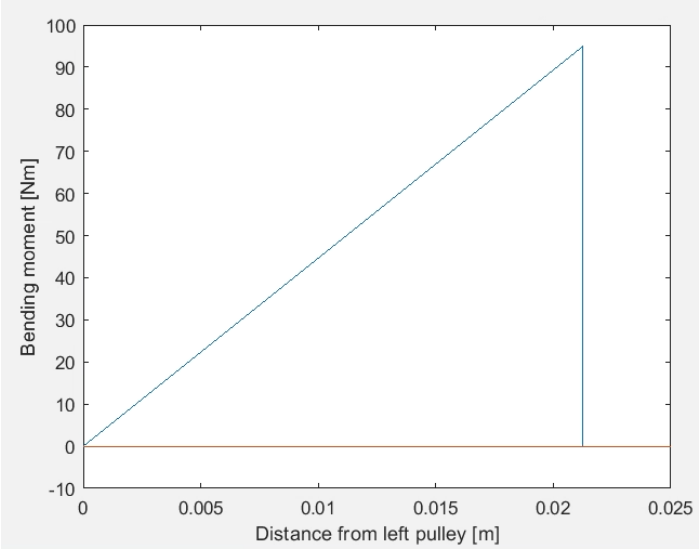

Figure 6-4 Bottom shaft M-L static load bending moment diagram

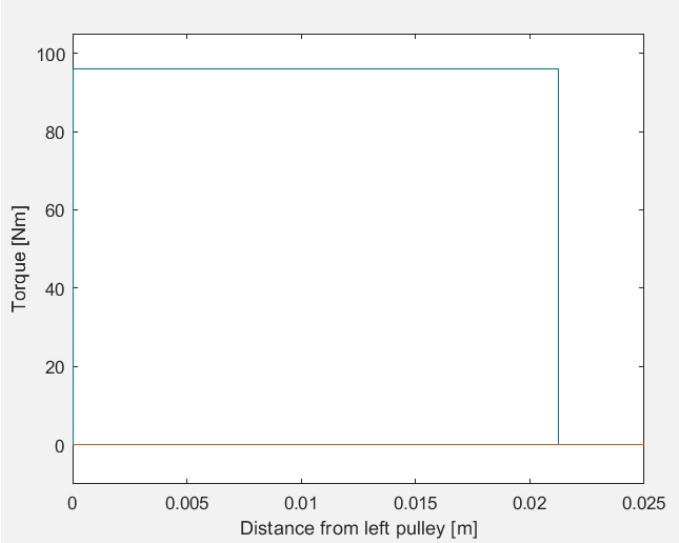

Figure 6-5 Bottom shaft torque diagram

Based on the three load diagrams, the shaft's right end (where it connects to the motor) has the largest stresses and was therefore the location of interest for the stress analysis. The bending stress was calculated with Eq. 6-4 [76]:

$$\sigma = \frac{Mc}{I} \quad \text{(Eq. 6-4)}$$

where σ is the bending stress, M is the bending moment, c is the radial distance from the shaft's centre, and I is the moment of inertia. For a hollow circular shaft such as those used in the PHP, the moment of inertia is calculated with Eq. 6-5:

$$I = \frac{\pi}{64}(D_o^4 - D_i^4) \quad \text{(Eq. 6-5)}$$

where I is the moment of inertia, D_o is the shaft outer diameter, and D_i is the shaft inner diameter.

Using Eq. 6-4 and Eq. 6-5, the maximum bending stress at the shaft bottom end was 128.9 MPa. Next, the torsional stress was calculated using Eq. 6-6 [76]:

$$\tau = \frac{Tc}{J} \quad \text{(Eq. 6-6)}$$

where τ is the torsional stress, T is the torque, and J is the polar moment of inertia, calculated with Eq. 6-7:

$$J = \frac{\pi}{32}(D_o^4 - D_i^4) \quad \text{(Eq. 6-7)}$$

Using Eq. 6-7 and Eq. 6-6, the maximum torsional stress on the bottom shaft with the 96 Nm maximum torque was 65.2 MPa. The bending stress and torsional stress were combined into the von Mises stress using Eq. 6-8 [76]:

$$\sigma' = (\sigma^2 + 3\tau^2)^{\frac{1}{2}} \quad \text{(Eq. 6-8)}$$

where σ' is the von Mises stress. The von Mises stress was 171.3 MPa, which resulted in a safety factor of 8.0 using Eq. 6-9:

$$n = \frac{S_y}{\sigma'} \quad \text{(Eq. 6-9)}$$

where S_y is the yield strength. With a safety factor of 8.0, the shaft is unlikely to yield due to the static loading conditions.

The bottom shaft must also resist fatigue failure. The process for cyclical stress analysis was similar to the static analysis, but the alternating and midrange stresses had to be calculated. The alternating bending stress was calculated using eq. 6-10 and the midrange bending stress was calculated using Eq. 6-11 [76]:

$$\sigma_a = K_f \frac{M_a c}{I} \quad \text{(Eq. 6-10)}$$

$$\sigma_m = K_f \frac{M_m c}{I} \quad \text{(Eq. 6-11)}$$

where σ_a is the alternating bending stress, K_f is the fatigue stress-concentration factor for bending, M_a is the alternating bending moment, σ_m is the midrange bending stress, and M_m is the midrange bending moment.

Since the loads acting on the bottom shaft are not affected by the ISO test loads applied to the PHP, the alternating and midrange stresses were determined by the tension force pulling on the shaft's pulley end. The maximum bending moment is 94.88 Nm (Figure 6-4) and the minimum bending moment is 0 Nm when the rope is not pulling on the shaft. Therefore, the midrange bending moment was 47.44 Nm and the alternating bending moment was 47.44 Nm. The shoulder fillet at the end of the bottom shaft adds a stress concentration to the shaft. Based on the shoulder dimensions, K_f is 2.1 [78]. Therefore, $\sigma_a = 135.3\ MPa$ and $\sigma_m = 135.3\ MPa$.

The alternating torsional stress was calculated using Eq. 6-12 and the midrange torsional stress was calculated using Eq. 6-13 [76]:

$$\tau_a = K_{fs}\frac{T_a c}{J} \quad \text{(Eq. 6-12)}$$

$$\tau_m = K_{fs}\frac{T_m c}{J} \quad \text{(Eq. 6-13)}$$

where, τ_a is the alternating torsional stress, K_{fs} is the fatigue stress-concentration factor for torsion, T_a is the alternating torque, τ_m is the midrange torsional stress, and T_m is the midrange torque.

The maximum torque is 96 Nm and the minimum torque is -96 Nm because the motor will apply 96 Nm to the PHP in both directions. Therefore, the alternating torque is 96 Nm and the midrange torque is 0 Nm. Based on the shoulder dimensions, K_{fs} is 1.75 [78]. Therefore, $\tau_a = 114.1\ MPa$ and $\tau_m = 0\ MPa$.

The bending and torsional stresses were combined to find the alternating von Mises stress (Eq. 6-14) and the midrange von Mises stress (Eq. 6-15) [76] :

$$\sigma'_a = (\sigma_a^2 + 3\tau_a^2)^{\frac{1}{2}} \quad \text{(Eq. 6-14)}$$

$$\sigma'_m = (\sigma_m^2 + 3\tau_m^2)^{\frac{1}{2}} \quad \text{(Eq. 6-15)}$$

where σ'_a is the alternating von Mises stress and σ'_m is the midrange von Mises stress. The fatigue safety factor was calculated using the modified Goodman line, Eq. 6-16 [76]:

$$\frac{1}{n} = \frac{\sigma'_a}{S_e} + \frac{\sigma'_m}{S_{ut}} \quad \text{(Eq. 6-16)}$$

where n is the safety factor, S_e is the endurance limit as described in Eq. 6-17, and S_{ut} is the ultimate tensile strength.

$$S_e = k_a k_b k_c k_d k_e k_f S'_e \quad \text{(Eq. 6-17)}$$

where

k_a = surface condition modification factor = 0.8511 for a ground shaft [79]

k_b = size modification factor = 0.90 for a 20 mm shaft [79]

k_c = load modification factor = 1 for combined bending and torsional loads [79]

k_d = temperature modification factor = 1 for room temperature [79]

k_e = reliability factor = 0.753 for 99.9% reliability [79]

k_f = miscellaneous-effects modification factor = 1 with no other known endurance limit reductions [79]

S'_e = test specimen endurance limit = 700 MPa for steels with $S_{ut} > 1400\ MPa$ [79]

Using Eq. 6-17 and Eq. 6-16, the shaft's endurance limit is 403 MPa and the fatigue failure safety factor is 1.5. Therefore, the bottom shaft should be able to sustain both static and cyclical loads without failure. Since the forces in the bottom shaft result from the ropes pulling on the shaft during power transmission, not from the applied test loads, the bottom shaft safety factors were the same for the M-L loading condition and the A-P loading condition. The bottom shaft safety factors are summarized in Table 6-2.

Table 6-2 Bottom shaft minimum safety factors for the four loading conditions

	Static Load Safety Factor	**Cyclical Load Safety Factor**
M-L Loading Condition	8.0	1.5
A-P Loading Condition	8.0	1.5

6.4 Motor Analysis

The motor FBD (Figure 6-6) was used to continue transferring the loads to the rest of the PHP components. The reaction forces between the motor and the knee found with the knee FBD were applied to the motor's distal end. Likewise, the reaction forces between the bottom shaft and the motor were also included. Using these known forces and Eq. 6-1 – Eq. 6-3, the resultant loads between the motor and the bearing housing were calculated for each loading condition.

No stress analysis was performed on the motor itself because the motor has already been tested and used successfully in a powered knee prosthesis. The forces found with the FBD were applied to the bearing housing FBD and were therefore needed for proximal component stress analyses.

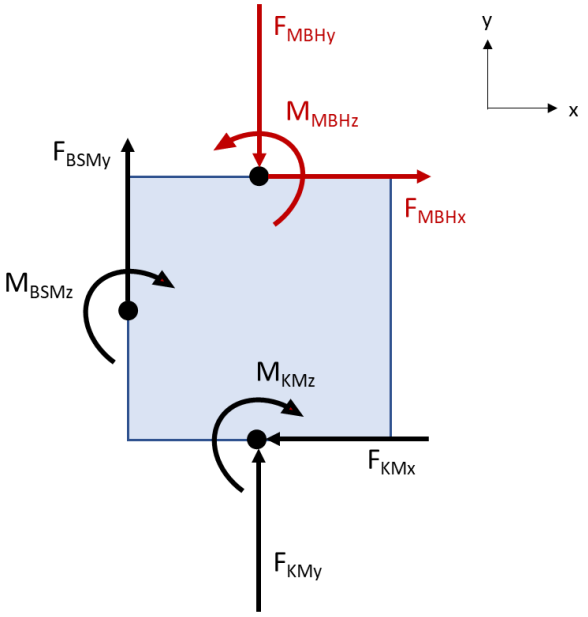

Figure 6-6 Motor frontal plane FBD, where F_{KMy} is the force between the knee and the motor in the y direction, F_{KMx} is the force between the knee and the motor in the x direction, M_{KMz} is the moment between the knee and the motor about the z-axis, F_{BSMy} is the force between the bottom shaft and the motor in the y direction, M_{BSMz} is the moment between the bottom shaft and the motor about the z-axis, F_{MBHx} is the force between the motor and the bearing housing in the x-direction, F_{MBHy} is the force between the motor and the bearing housing in the y direction, and M_{MBHz} is the moment between the motor and the bearing housing about the z-axis. Known forces are depicted in black and unknown forces are depicted in red.

6.5 Bearing Housing Analysis

The bearing housing is made of Aluminum 2024-T4. The bearing housing FBD (Figure 6-7) was used to determine the reaction forces between the bearing housing and the top shaft. Using Eq. 6-1-Eq. 6-3, F_{BHTS1y} was 7141 N, F_{BHTS2y} was 667.6 N, and F_{BHTS2x} was 329.6 N for the M-L static load case. The M-L static loading condition resulted in the highest force values for the four loading conditions.

The needle roller bearings used in the PHP have a dynamic load rating of 9100 N and a static load rating of 13,400 N. Therefore, for the 7141 N maximum radial load, the bearings have a safety factor of 1.3 for dynamic loading and 1.9 for static loading. Thus, the bearings should not fail with PHP use.

A stress analysis was performed at the filleted corner of the lateral side housing, which was the bearing housing critical location. Using stress calculations, the maximum bending stress for the M-L static load was 64.7 MPa, resulting in a safety factor of 5.0. For the fatigue calculations,

a 1.6 stress concentration factor was used based on the filleted corner geometry [78]. The M-L cyclical safety factor was 1.7. The calculations were repeated with the A-P loading conditions resulting in a 10.5 A-P static safety factor and a 2.6 A-P cyclical safety factor. The bearing housing safety factors are summarized in Table 6-3.

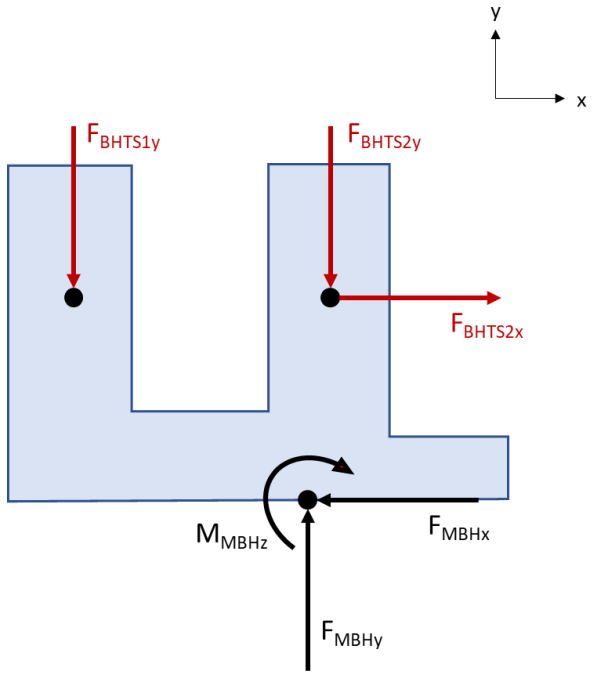

Figure 6-7 Bearing housing frontal plane FBD, where F_{MBHy} is the force between the motor and the bearing housing in the y direction, F_{MBHx} is the force between the motor and the bearing housing in the x direction, M_{MBHz} is the moment between the motor and the bearing housing about the z-axis, F_{BHTS1y} is the force between the top shaft and the lateral side of the bearing housing in the y direction, F_{BHTS2y} is the force between the top shaft and the medial side of the bearing housing in the y direction, and F_{BHTS2x} is the force between the top shaft and the medial side of the bearing housing in the x direction. Known forces are depicted in black and unknown forces are depicted in red.

Table 6-3 Bearing housing minimum safety factors for the four loading conditions

	Static Load Safety Factor	**Cyclical Load Safety Factor**
M-L Loading Condition	5.0	1.7
A-P Loading Condition	10.5	2.6

6.6 Top Shaft Analysis

The top shaft is made of 17-4 PH Stainless Steel H900. The top shaft frontal plane FBD is pictured in Figure 6-8. The forces from the pulley and the bearing housing were added to the shaft and used to calculate the forces between the top shaft and the hinge.

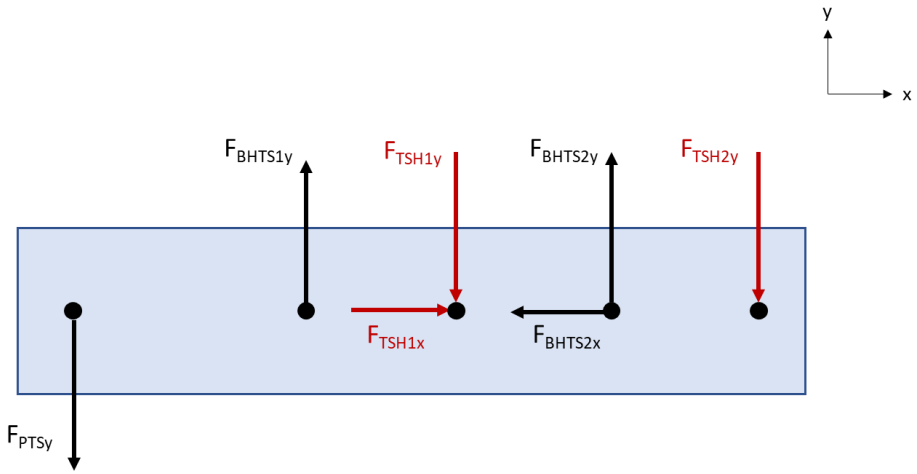

Figure 6-8 Top shaft frontal plane FBD, where F_{PTSy} is the force between the pulley and the top shaft in the y direction, F_{BHTS1y} is the force between the top shaft and the lateral side of the bearing holder in the y direction, F_{TSH1y} is the force between the top shaft and the lateral side of the top hinge in the y direction, F_{TSH1x} is the force between the top shaft and the lateral side of the top hinge in the x direction, F_{BHTS2y} is the force between the top shaft and the medial side of the bearing holder in the y direction, F_{BHTS2x} is the force between the top shaft and the medial side of the bearing holder in the x direction, and F_{TSH2y} is the force between the top shaft and the medial side of the top hinge in the y direction. Known forces are depicted in black and unknown forces are depicted in red.

Using forces in the FBD, shear force and bending moment diagrams were created to determine the internal forces along the shaft length. The M-L static loading condition shear force diagram is presented in Figure 6-9 and the bending moment diagram is presented in Figure 6-10. The torque diagram is pictured in Figure 6-11 and was based on the 96 Nm maximum torque for the M-L static loading condition.

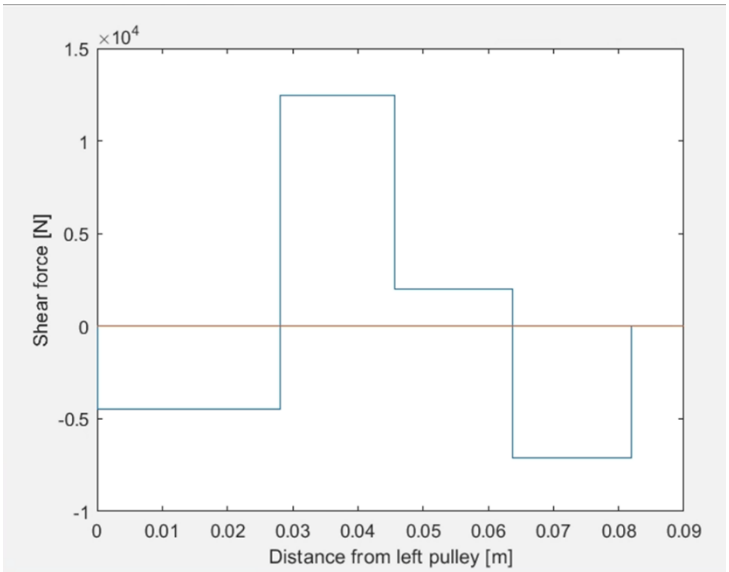

Figure 6-9 Top shaft static M-L loading condition shear force diagram

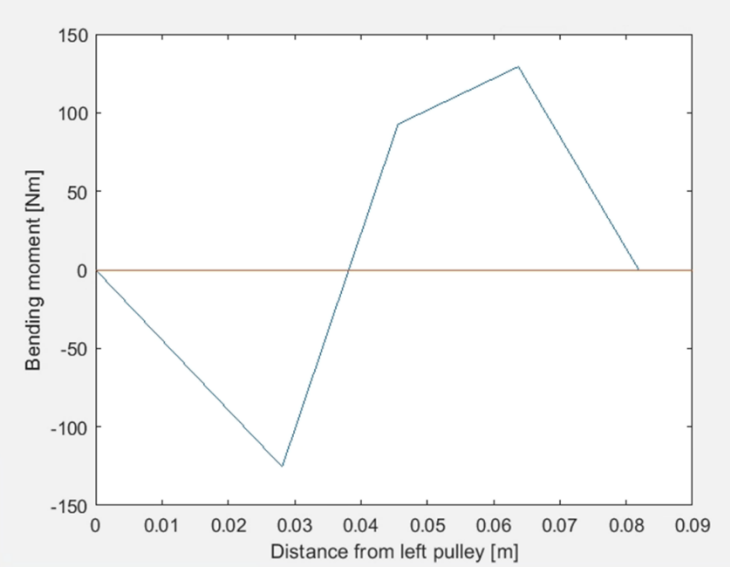

Figure 6-10 Top shaft static M-L loading condition bending moment diagram

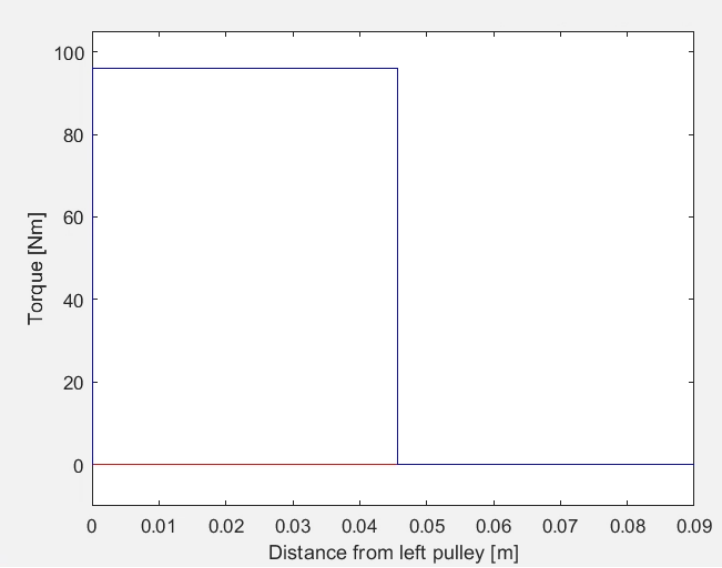

Figure 6-11 Top shaft torque diagram

The maximum stresses calculated occur where the top shaft interfaces with the lateral side of the bearing housing, as can be observed on the bending moment and torque diagrams. The static failure analysis was performed at this critical location. Using the same calculations outlined in Chapter 5.5, the static M-L safety factor was 9.4.

The process of creating the shear and bending moment diagrams was repeated with the M-L minimum cyclical load and the M-L maximum cyclical load. Based on the cyclical diagrams, the point where the top shaft interfaces with the hinge lateral side was the critical location for fatigue failure. The stress concentration at this point in the shaft was due to the hole for the pin. Based on the hole size relative to the shaft diameter, a bending stress fatigue concentration factor of 1.95 and a torsion stress fatigue concentration factor of 2.95 were used in the fatigue calculations [78]. The minimum safety factor for cyclical loading was 1.3. Therefore, the top shaft should sustain both static and cyclical loading.

The stress analysis was repeated for the A-P static and cyclical loading conditions, resulting in a safety factor of 8.5 for A-P static loading and 1.13 for A-P cyclic loading. The top shaft safety factors are summarized in Table 6-4.

Table 6-4 Top shaft minimum safety factors for the four loading conditions

	Static Load Safety Factor	Cyclical Load Safety Factor
M-L Loading Condition	9.4	1.3
A-P Loading Condition	8.5	1.13

6.7 Top Hinge Analysis

The top hinge is made of Aluminum 2024-T4. The top hinge frontal plane FBD (Figure 6-12) features the known reaction forces from the top shaft and was used to determine the reaction forces between the top hinge and the lamination plate.

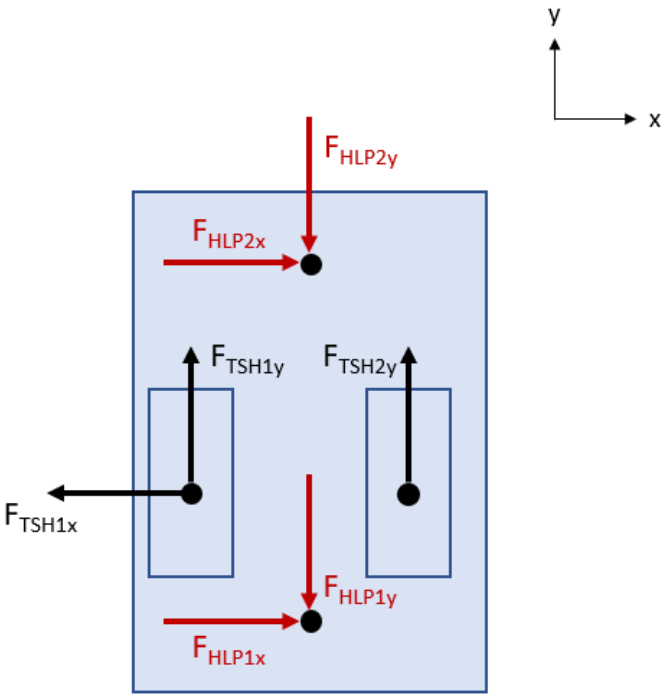

Figure 6-12 Top hinge frontal plane FBD, where F_{TSH1x} is the force between the top shaft and the lateral side of the top hinge in the x direction, F_{TSH1y} is the force between the top shaft and the lateral side of the top hinge in the y direction, F_{TSH2y} is the force between the top shaft and the medial side of the top hinge in the y direction, F_{HLP1x} is the force between the top hinge and the distal and of the lamination plate in the x direction, F_{HLP1y} is the force between the top hinge and the distal and of the lamination plate in the y direction, F_{HLP2x} is the force between the top hinge and the proximal and of the lamination plate in the x direction, F_{HLP2y} is the force between the top hinge and the proximal and of the lamination plate in the y direction. Known forces are depicted in black and unknown forces are depicted in red.

Based on the top hinge loads, the top hinge medial side encountered a 66.36 Nm bending moment acting as a cantilever beam for the M-L static loading condition. This equated to a 34 MPa bending stress and a 9.4 safety factor.

The maximum M-L cyclical loading bending stress was on the top hinge lateral side. The minimum safety factor in fatigue was 1.4. In A-P loading, the static safety factor was 3.9 and the cyclic safety factor was 1.4. The top hinge safety factors are summarized in Table 6-5.

Table 6-5 Top hinge minimum safety factors for the four loading conditions

	Static Load Safety Factor	**Cyclical Load Safety Factor**
M-L Loading Condition	9.4	1.4
A-P Loading Condition	3.9	1.4

6.8 Pulley Analysis

The pulleys are made of 17-4 PH Stainless Steel H900. Without the side plate supporting the edge of the pulley, the pulley rope groove (Figure 6-13) would act like a cantilever beam. In Figure 6-14, the rectangular section outlined in Figure 6-13 is modelled as a cantilever beam. The FBD in Figure 6-14 depicts the 4465 N force from the rope dispersed across the surface of the pulley rope groove.

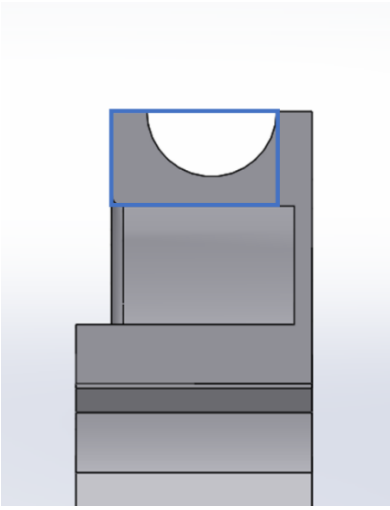

Figure 6-13 PHP pulley cross-section. The blue rectangle outlines the portion of the pulley that is modelled as a cantilever beam.

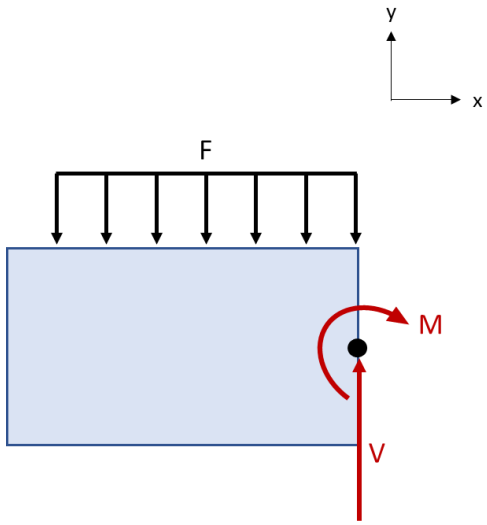

Figure 6-14 FBD of the pulley rope groove modelled as a cantilever beam, where F is the force from the rope acting on the pulley, V is the shear force at the edge of the rope groove, and M is the bending moment at the edge of the rope groove. Known forces are depicted in black and unknown forces are depicted in red.

Shear force (Figure 6-15) and bending moment (Figure 6-16) diagrams were created for the pulley based on the cantilever beam FBD. The maximum bending moment in the pulley rope groove was 12.28 Nm.

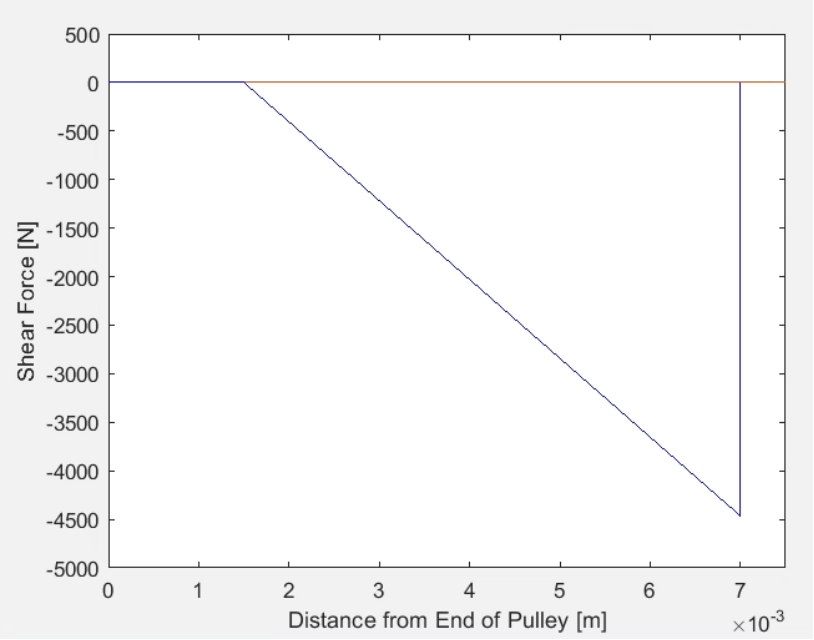

Figure 6-15 Pulley rope groove shear force diagram

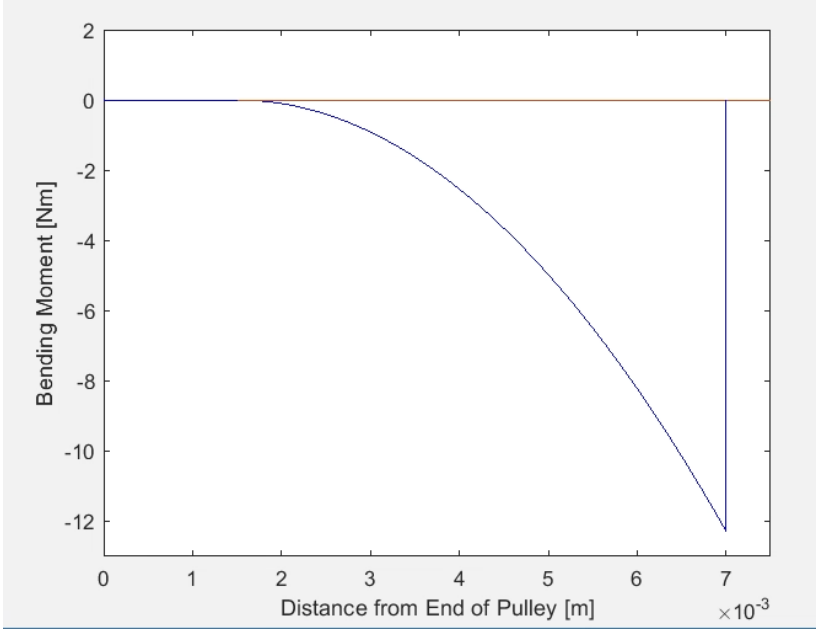

Figure 6-16 Pulley rope groove bending moment diagram

Using the maximum bending moment, the maximum bending stress in the pulley would be 1151 MPa, resulting in a static failure safety factor of 1.2. For cyclical loading, the maximum bending moment would be 12.28 Nm and the minimum bending moment would be 0 Nm when the rope is not exerting a force on the pulley. Therefore, the alternating bending stress would be 576 MPa and the midrange stress would be 576 MPa. Using the modified Goodman line, the fatigue failure safety factor was 0.64, indicating fatigue failure would occur in the pulley without the side plate supporting the other end of the rope groove.

With the addition of the side plate, the bending stress in the pulley was halved and the safety factors were therefore doubled. So, the pulley static failure safety factor became 2.4 and the fatigue safety factor became 1.3, and failure was no longer predicted.

Since the test load applied to the PHP does not affect the loads on the pulley, the safety factors for the A-P loading conditions are the same as for the M-L loading conditions. The pulley safety factors are summarized in Table 6-6.

Table 6-6 Pulley minimum safety factors for the four loading conditions

	Static Load Safety Factor	**Cyclical Load Safety Factor**
M-L Loading Condition	2.4	1.3
A-P Loading Condition	2.4	1.3

6.9 Attachment Ring Analysis

The attachment ring is made of aluminum 2024-T4 and prevents the motor's lateral side from rotating, withstanding the 96 Nm maximum torque. An attachment ring stress analysis at the critical locations, including the screw holes and the edges, determined a 6.2 minimum safety factor.

The strength of the screws holding the attachment ring to the attachment plate was also analyzed to ensure that the screws would not fail when the maximum torque is applied. The screws holding the attachment ring to the attachment plate are class 12.9, M5, coarse thread screws (14.2 mm^2 stress area, A_t, and 970 MPa proof load, S_p [80]). The screws are located 30 mm from the attachment ring's center. Therefore, when the attachment ring faces a 96 Nm torque, the screws are subjected to a 3200 N tension force (Eq. 4-4). Assuming that one screw will take all the load in resisting the torque, the screw faces a 225.3 MPa stress (Eq. 6-18 [80]).

$$\sigma = \frac{F}{A_t} \qquad \text{(Eq. 6-18)}$$

To determine the screw safety factor, n, the calculated stress was compared to the proof load using Eq. 6-19.

$$n = \frac{S_p}{\sigma} \qquad \text{(Eq. 6-19)}$$

The screw safety factor was 4.3, indicating that the screws should be able to withstand the tension forces from the maximum torque.

6.10 Key Analysis

The steel keys are used to transmit the torque between the shafts and the pulleys and thus must sustain the stresses generated from the torque. Two possible modes of failure for the keys are shear stress and crushing. Shear stress can be calculated with Eq. 6-20 [76]:

$$\tau = \frac{F}{tl} \qquad \text{(Eq. 6-20)}$$

where τ is the shear stress, F is the force at the shaft surface, t is the key width and l is the key length. The force can be calculated with Eq. 4-4. For a 96 Nm maximum torque and 10 mm shaft radius, the force at the shaft surface would be 9600 N. The key width is 3 mm and the length is 10 mm. Using Eq. 6-20, the shear stress on the key was 320 MPa.

The distortion-energy theory (Eq. 6-21) describes shear strength, S_{sy}, in terms of yield strength, S_y.

$$S_{sy} = 0.577 S_y \quad \text{(Eq. 6-21)}$$

17-4 PH stainless steel has a yield strength of 1379 MPa and therefore a shear strength of 795.683 MPa. The safety factor, n, for shear failure was calculated with Eq. 6-22 and found to be 2.5. Therefore, the keys should not fail from shear stress.

$$n = \frac{S_{sy}}{\tau} \quad \text{(Eq. 6-22)}$$

The safety factor for crushing failure is calculated with Eq. 6-23 [76]:

$$n = \frac{S_y t l}{2F} \quad \text{(Eq. 6-23)}$$

The safety factor for crushing is 2.2. Therefore, the keys should be able to resist both shear and crushing failure.

Chapter 7: Prototype

After the stress analysis, the model was prepared for manufacturing. Tolerances were added to each part to ensure that the parts could be assembled without interference and to limit the amount of movement between components. Sliding fits were used for the components that need to slide onto the shafts, namely the pulleys, bearings, and top hinge. Smaller tolerances were used for parts that needed to align more precisely, such as the bottom shaft over the bolt heads on the motor.

Tolerance chains were avoided wherever possible, to reduce the stacking of tolerances and consequent fit issues. The pulley and rope system was beneficial in reducing the number of tolerance chains because the ropes can be tightened after assembly and therefore the proximal-distal dimensions did not need to be as precise. There were, however, tolerance chains in the medial-lateral direction on the shafts and the attachment plate. For these locations where the tolerances were stacked, the dimensions were specified to provide additional space between the components. The additional space ensures that all the components fit into the assembly and shims can be used to fill the gaps if there is too much extra room.

Mechanical drawings were made for each PHP component, specifying the material, dimensions, and tolerances of each part (Appendix A). Once all drawings were completed, they were sent to machine shops to have the parts made. The PHP was assembled, and the finished prototype is pictured in .

While assembling the PHP, several small issues with the part tolerances created interference between PHP components. To resolve these issues, some material was cut away from the medial attachment piece and the bearing housing. With these additional post-manufacturing changes, all parts fit together well. Dimensions in the drawings were adjusted accordingly for any future PHP iterations.

(a)

(b)

(c)

Figure 7-1 PHP prototype with pulley cover (a), PHP prototype side view without cover front (b), PHP prototype front view without cover front (c)

Chapter 8: Mechanical Evaluation

Once the prototype was built and assembled, PHP strength was tested using the testing procedures outlined in ISO 15032:2000 Prostheses – Structural testing of hip joints [43]. Two testing conditions were examined – anterior-posterior (A-P) extension and medial-lateral (M-L). The A-P flexion loading condition was not performed since this test is only used for hip joints with a stride limiter.

Only static tests were performed for PHP structural testing since the main objective was to ensure that the PHP is strong enough to sustain weight-bearing and thus be safe for continued functional testing with people. Functional testing in this thesis will not provide enough cycles to reach fatigue failure. In the future, cyclical testing should be performed to ensure that the PHP is safe for long-term use.

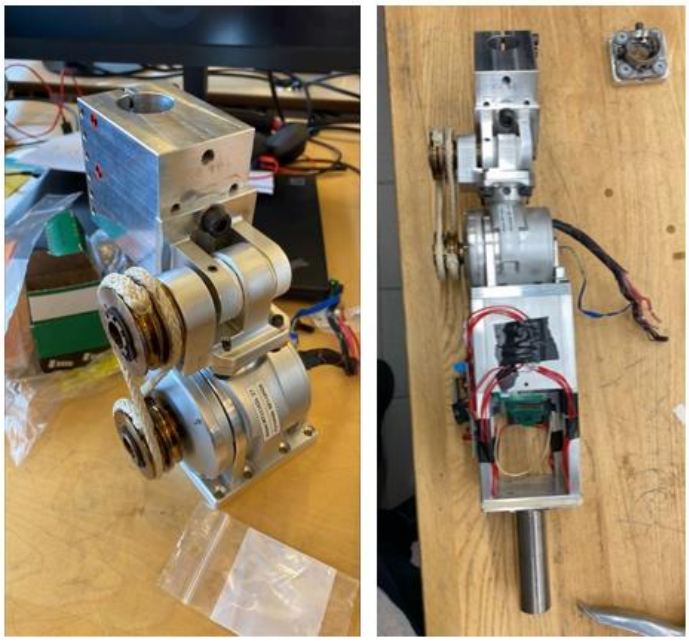

Figure 8-1 PHP bolted to metal block for structural testing (left) and metal pole connected to the PHP bottom for structural testing (right)

The PHP was tested in a servohydraulic testing system. The PHP top hinge was bolted to a metal block (Figure 8-1) that slides onto a pole in the testing machine. A female pyramid adapter was attached to the bottom of the electronics chassis to interface with another pole (Figure 8-1), to secure the PHP bottom in the testing machine. The moment arm lengths in the servohydraulic testing system were based on the loading conditions in the ISO standard.

8.1 Medial-Lateral Test

8.1.1 M-L Testing Setup

The M-L test setup was based on the ISO 15032:2000 M-L loading condition. The ISO document depicts a vertical hip device with the force applied at an angle; however, the testing machine can only apply force in the vertical direction, so the PHP was set at the appropriate angle. The testing equipment arm lengths were calculated from the moment arms outlined in ISO 15032:2000 and the overall PHP length. The M-L test setup is shown in Figure 8-2.

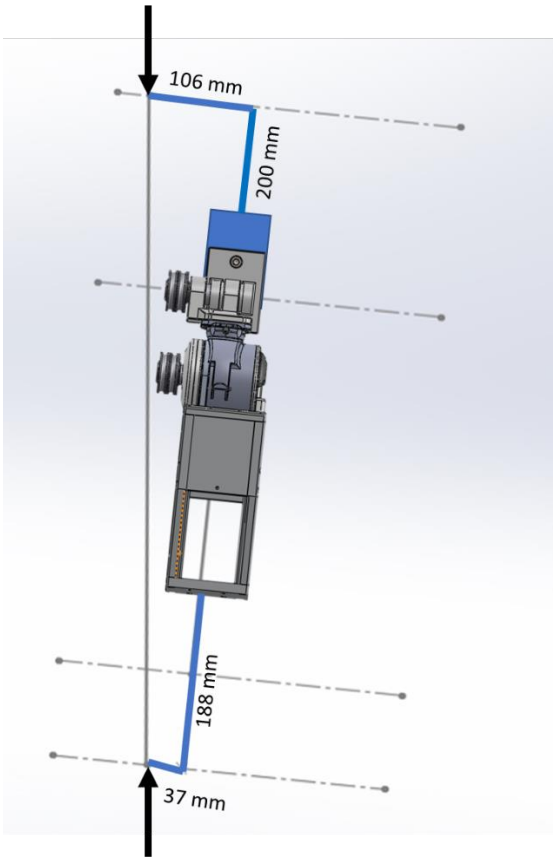

Figure 8-2 Medial-lateral mechanical testing setup and dimensions

As seen in Figure 8-2, the arm at the bottom of the testing setup should be 37 mm. However, the testing equipment used had a minimum length of 50 mm for that arm. So, a length of 50 mm was used instead. This increased the moment arm, thereby increasing bending stresses on the device and making the test more conservative. Following ISO 15032:2000, the M-L test was performed with the PHP in the fully extended position (Figure 8-3).

Figure 8-3 PHP in the testing machine for the M-L mechanical testing

8.1.2 M-L Testing Results

The force on the PHP was first set to the 1024 N settling force for 30 s, then returned to zero. Next, the force was increased by 200 N/s to the 3360 N ductile failure ultimate test force and then back to zero. The ductile failure test force was used because all PHP structural components are made of either aluminum or steel, which are both ductile materials. The force and displacement data recorded by the testing machine are presented in Figure 8-4.

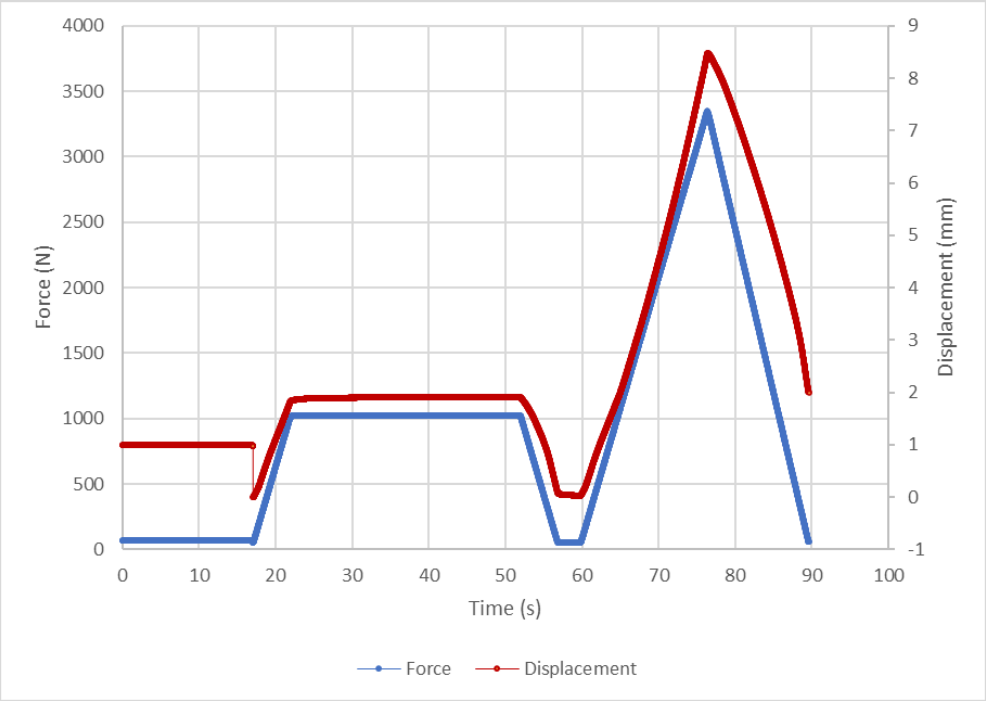

Figure 8-4 M-L structural test force and displacement versus time

Even with the longer moment arm on the bottom, the PHP successfully sustained the ultimate test force without failure. As seen in Figure 8-4, when the force goes to zero after the ultimate test force, displacement returns to the same value as during the settling force. No observable damage or deformation was found on the PHP components after the M-L test.

8.2 Anterior-Posterior Test

8.2.1 A-P Testing Setup

The A-P testing setup was based on the ISO 15032:2000 A-P extension test (Figure 8-5). Figure 8-6 shows the device in the testing equipment for the A-P test.

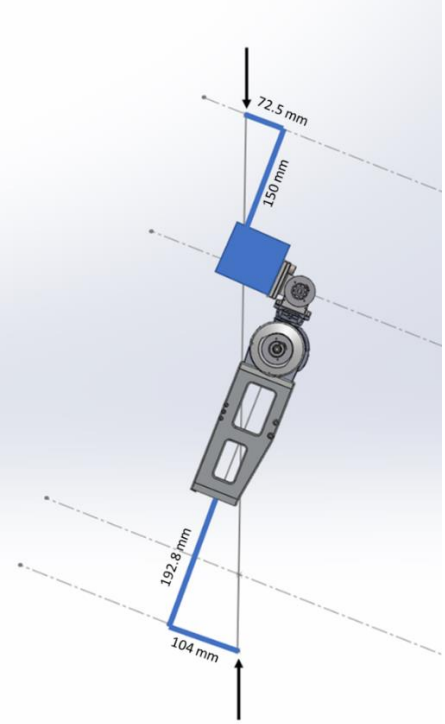

Figure 8-5 Anterior-posterior mechanical testing setup and dimensions

Figure 8-6 PHP in the testing machine for the A-P mechanical testing

8.2.2 A-P Testing Results

The same M-L test procedure was performed for the A-P test. The force and displacement data recorded by the testing machine for the A-P test are presented in Figure 8-7.

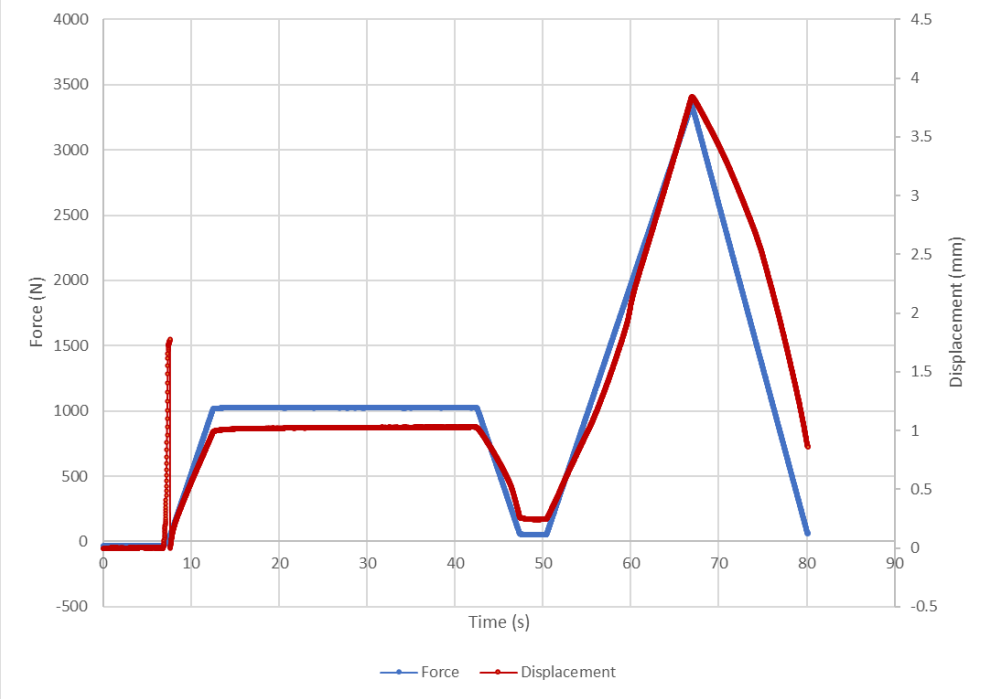

Figure 8-7 A-P structural test force and displacement versus time graph

Again, the PHP successfully sustained the ultimate test force without failure. Therefore, the PHP passed the structural tests and was considered safe for continued functional testing.

Chapter 9: Functional Evaluation

Once the PHP had been deemed structurally sound, functional testing was performed to determine if the prosthesis could successfully help a person ambulate. The device was first tested by powering the motor without any user. This was done to ensure that the system operated as expected and to resolve any issues with the controls and the pulley system. Next, able-bodied volunteers walked with the PHP using a HKAF prosthesis simulator.

9.1 Initial Testing

Initial functional testing was conducted to ensure that the PHP moved properly when the motor was powered. With the PHP fully assembled, a simple control pattern was applied to the motor to have the hip joint flex and extend in a repeating motion. The PHP rotated as expected; however, slack quickly developed in the system. It was observed that the ropes were lengthening with use. This issue arose not due to the Vectran fibres themselves stretching, but due to braiding. The individual strands of the rope were stretching relative to each other. After a few tests, the ropes had elongated too much to be useable with the PHP because they became too long to wrap around the pulleys without overlapping themselves.

Steel cables were used as a temporary solution. The cables were crimped to a fixed length, inserted into the pulley, and then wrapped around the pulley (Figure 9-1). After the first test, it was noted that the steel cables experienced the same type of stretching as the Vectran ropes with its similar braided design. However, unlike the Vectran ropes, after the first couple of tests and elongation, the steel cables stopped stretching and remained a consistent length. Therefore, no more slack developed in the system with continued use, and they could be used for the next step of functional testing. Though the steel cables were a successful solution for the hip simulator testing, they would not be ideal for a final product. Firstly, the cable's rated capacity was 1779 N [81], which is under the 4465 N tensile strength design criterion. Therefore, there is a risk of failure when the PHP faces increased loads. Next, the crimps stick out of the pulleys which is not visually appealing and prevented the cover from fitting over the pulleys. A future project will investigate other termination options for the Vectran rope.

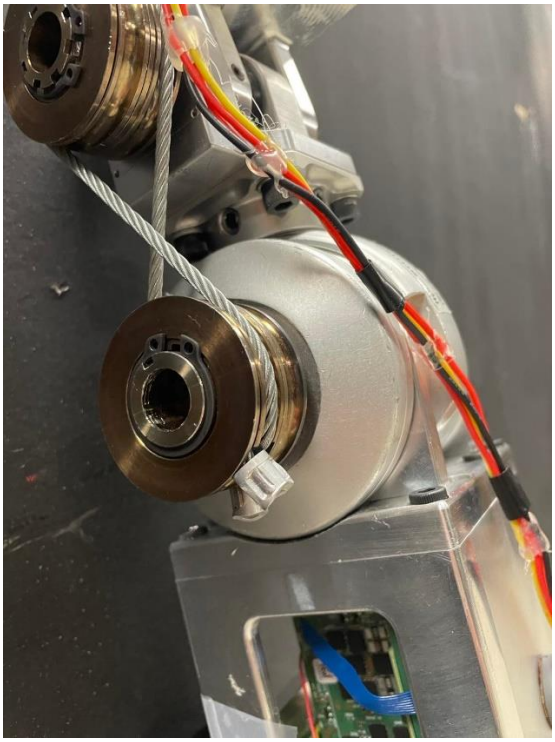

Figure 9-1 Crimped steel cables replacing the Vectran ropes

9.2 Hip Disarticulation Simulator Testing

After testing PHP motion and fixing the slack issue by using steel cables, the PHP was tested with non-amputee participants on a hip disarticulation simulator. Gait footage was analyzed using video annotation software to determine hip range of motion and gait parameters. Participant subjective feedback was also recorded comparing the PHP to previous Helix3D walking tests. The simulator testing protocol was approved by the University of Ottawa Office of Research Ethics and Integrity (Appendix B).

9.2.1 Testing Setup

The PHP was tested using a prosthesis simulator (Figure 9-2) [82] that allows non-amputees to walk with a HKAF prosthesis. An ethylene vinyl acetate foam sole was inserted into the left shoe, increasing the user's left leg height [82]. The hip-knee-ankle prosthesis was connected laterally to the participant's right side using a hip abduction orthosis. The extra length on the left side created a clearance of 4 cm between the user's right foot and the floor [82]. Therefore, weight-bearing occurs only on the participant's left natural leg and on the prosthetic leg on the right.

Figure 9-2 Hip disarticulation simulator setup with Helix 3D hip joint, showing 4 cm ground clearance on the prosthetic-side healthy limb [82]

Figure 9-3 Hip disarticulation simulator with PHP, Össur Rheo 3 knee joint, and Össur Pro-Flex XC foot

The PHP was joined to an Össur Rheo 3 knee joint and an Össur Pro-Flex XC foot to create a full HKAF prosthesis (Figure 9-3). Prosthetic leg length was adjusted for each participant to ensure equal leg lengths between the prosthetic and intact sides. Participants had the option of using one or two walking canes to assist with balance, based on the participant's comfort level with the hip disarticulation simulator.

A testing walkway was created in the Movement Performance Laboratory at the University of Ottawa. Tape markings were placed on the laboratory floor to identify a 10 m walkway.

9.2.2 Methodology

PHP functionality was evaluated for level gait. The three participants walked 10 m one way then turned around and walked 10 m back. A second volunteer walked beside the participant with a camera to record the trials. The video footage was later analyzed to evaluate gait parameters such as range of motion and step time. All three participants had previously used the simulator to walk with the Helix3D hip joint [82]. Subjective feedback comparing the PHP with the Helix3D was also obtained. The participants were given one training session to get accustomed to walking with the PHP on the simulator and one testing session where the data was recorded.

9.2.2.1 Participants

Three male volunteers between the ages of 25 and 44 participated in the functional testing with the simulator (Table 9-1). Only healthy participants with two intact legs were considered for this study. Participant heights ranged from 175 cm to 180 cm and weights ranged from 95 kg to 98 kg. Participant A used one walking cane during testing and participants B and C used two.

Table 9-1 Functional testing participant demographics

	Participant A	**Participant B**	**Participant C**
Sex	Male	Male	Male
Age (years)	44	28	25
Height (cm)	178	180	175
Weight (kg)	95	95	98
Number of Walking Canes Used	1	2	2

9.2.2.2 Control System

At the time of testing, the PHP control system was still under development. Therefore, a repeated gait cycle was used (Figure 9-4). The hip angle began at 40° flexion at heel strike, then extended to a 20° maximum extension. The hip then flexed to 44° maximum flexion and slowly returned to 40° flexion. A 2.5 s stride time was used to ensure all participants would be able to keep up with the walking pace.

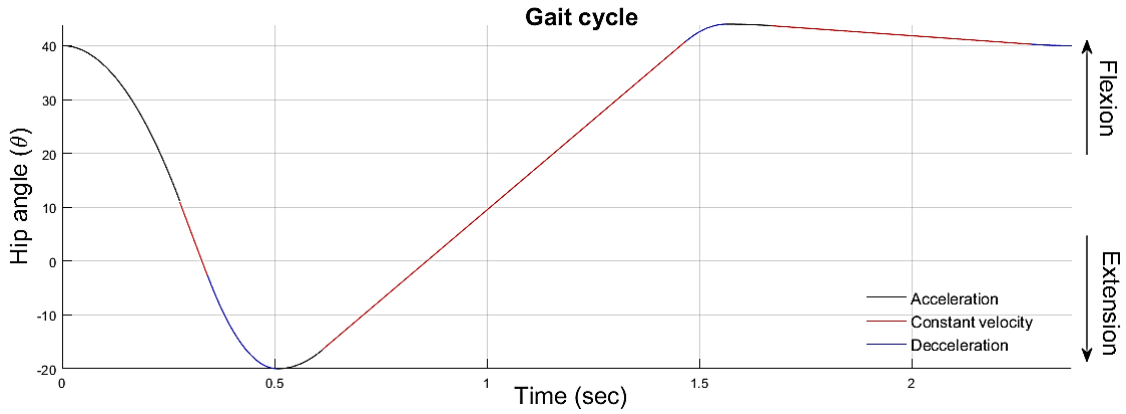

Figure 9-4 Functional testing controls hip angle profile

9.2.3 Results and Discussion

The functional testing video footage was analyzed using the Kinovea video annotation tool [83]. Five consecutive strides were examined for each participant to determine average ranges of motion and step times. The five strides were selected where there were no large stumbles, and the participant did not put their prosthetic-side natural foot down.

The hip angle was measured between the line along the torso and the line from the hip joint to the knee joint (Figure 9-5). This angle was tracked throughout the five strides (Figure 9-6).

Figure 9-5 Participant C 42.2° maximum hip flexion (left) and participant C 19.8° maximum hip extension (right)

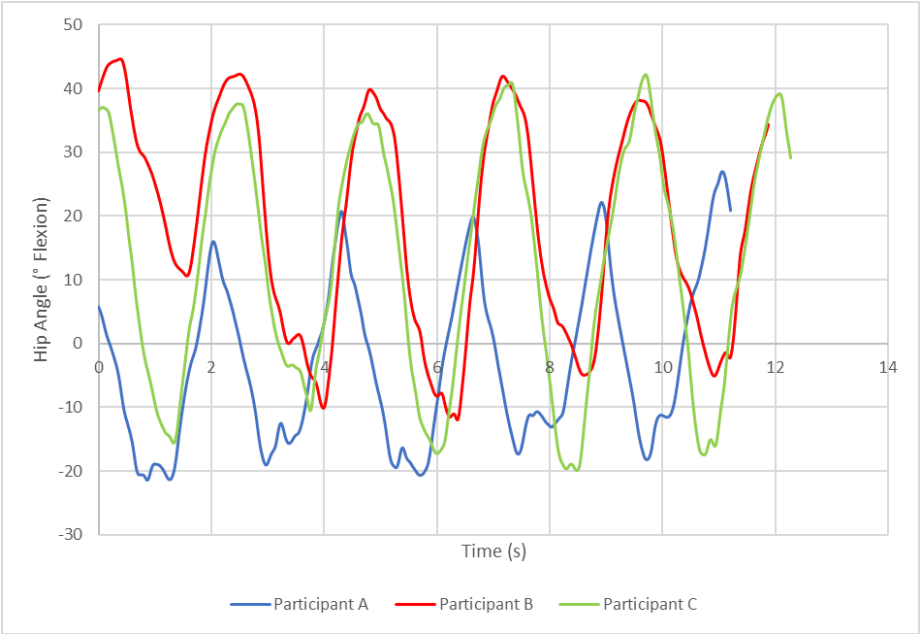

Figure 9-6 PHP hip flexion angle vs time across 5 strides for participant A (blue), participant B (red), and participant C (green)

Participant A's gait cycle appears shifted to the left compared to participant B and C. This is because participant A placed his prosthetic foot down (initial contact) at an earlier point in the

predetermined gait profile than the other two participants. This was a result of personal preference in walking with the simulator.

The maximum angles for each participant are identified in Table 9-2. The average range of motion was 55.7°. This was 8.3° less than the programmed 64° range of motion. One factor that may contribute to the discrepancy is that the camera was not always perfectly square to the PHP. Therefore, when the video was analyzed in 2D, the angle relative to the camera would affect the measured hip angle. Furthermore, markers were not used to measure the angles. The software had a difficult time tracking the angles and the end points had to be manually adjusted frame by frame. Markers would have helped maintain consistent reference points and produced more accurate angle measurements. The gait control system could have undershot the target angle.

Table 9-2 Functional testing range of motion

Participant	**Maximum Flexion (°)**	**Maximum Extension (°)**	**Range of Motion (°)**
A	26.9	21.4	48.3
B	44.7	12.0	56.7
C	42.2	19.8	62.1
Average	37.9 ± 7.9	17.7 ± 4.1	55.7 ± 5.7

Kinovea was also used to identify initial contact and toe-off moments for both feet. These initial contact and toe-off moments were used to calculate the average step times across the 5 strides (Table 9-3). The prosthetic step time (from initial contact to toe off) was on average 0.63 times the intact step time, meaning that the gait was asymmetrical and the participants were spending more time on their healthy side than on the prosthetic side. This asymmetry was likely due to the participants feeling less stable on the prosthetic side, thus swinging their intact leg quickly to return the more stable leg to the ground. The intact leg swing time was on average 0.29 s, while the prosthetic leg swing time was on average 1.08 s, confirming that the participants were swinging the intact leg faster than the prosthetic leg was programmed to swing.

Table 9-3 Functional testing gait parameters with percentages of average stride time

		Participant A	Participant B	Participant C	Average
Stride Time (s)		2.35 ± 0.06	2.38 ± 0.09	2.45 ± 0.08	2.39 ± 0.05
Step Time (s)	**Prosthetic**	1.50 ± 0.09 (64 %)	1.19 ± 0.05 (50%)	1.24 ± 0.07 (51%)	1.31 ± 0.17 (55%)
	Intact	2.04 ± 0.05 (87%)	2.09 ± 0.02 (88%)	2.09 ± 0.09 (85%)	2.07 ± 0.03 (87%)
Swing Time (s)	**Prosthetic**	0.85 ± 0.06 (36%)	1.18 ± 0.13 (50%)	1.22 ± 0.07 (50%)	1.08 ± 0.20 (45%)
	Intact	0.27 ± 0.02 (11 %)	0.27 ± 0.03 (11%)	0.34 ± 0.05 (14%)	0.29 ± 0.04 (12%)
Double Support Time (s)		0.61 ± 0.09 (26%)	0.46 ± 0.07 (19%)	0.45 ± 0.11 (18%)	0.51 ± 0.09 (21%)
Cadence (steps/min)		51.15	50.51	48.94	50.20 ± 1.14
Step Time Ratio		0.74	0.57	0.59	0.63 ± 0.09

All three participants stated that the PHP was easier to walk with than the non-powered Helix3D. They specifically noted that they no longer felt like they had to swing the prosthesis around to move it forward, therefore reducing necessary pelvic rotation. Other feedback included that the extra weight of the PHP was not noticeable and that the participants did not feel like they were carrying a heavy object when they had to support the prosthetic swing phase. This subjective feedback supports continued development of the PHP and suggests potential for the PHP to be a successful solution in improving ambulation for hip disarticulation and hemipelvectomy amputees. More detailed biomechanical testing can confirm any differences in pelvic motion between Helix3D gait and PHP gait. Gait analysis and subjective feedback from amputees using the PHP are needed to fully observe the benefits of adding power to the hip joint.

Chapter 10: Conclusions and Future Work

In this thesis, a novel microprocessor-controlled PHP was designed and evaluated for both strength and function. The pulley and rope power transmission system proved successful in transmitting the rotational power from the actuator to the hip joint. The final design met all the design criteria, including mechanical strength tests. The PHP was also tested with able-bodied participants using a hip disarticulation simulator, where ambulation was successful. Though the current design achieved positive results and shows promise as a hip amputee ambulation aid, future work is still needed to improve and evaluate the design.

10.1 Design Criteria

The final PHP met all the design criteria outlined in Chapter 3:. The final device weighed 3.9 kg, as measured with a scale. This put the PHP under the 4.0 kg weight limit. The functional testing participants noted that this 3.9 kg weight did not feel heavy while walking, or noticeably impede their motion.

The PHP needed to support users up to 100 kg. The PHP successfully supported a 98 kg user during functional testing, which is close to the required 100 kg. The PHP also successfully passed ISO mechanical testing designed for users up to 100 kg. The strength requirements outlined in ISO 15032:2000 were to withstand a 2240 N load for 30 s without failure or deformation greater than 15 mm, withstand a 3360 N load without ductile failure, and withstand 2×10^6 cycles between 50 N and 1330 N without failure. The PHP faced a 3360 N load without failure or deformation greater than 15 mm. Cyclical testing was not conducted on the PHP; however, calculations and FEA simulations indicate that the device should be able to withstand fatigue from the cycles outlined in the ISO standard.

In functional testing, the PHP reached 21.4° extension and 44.7° flexion. Therefore, the PHP obtained the 20° hip extension requirement. The maximum flexion value was due to the gait pattern controls, not a physical limit of the device itself. When placed in maximum flexion, the PHP hip angle measured with a protractor was 145°, successfully surpassing the 130° hip flexion requirement.

The final PHP power transmission gear ratio was 1:1. Therefore, the device should have the same maximum torque and angular velocity as the actuator. The maximum actuator torque is

96 Nm and the maximum angular velocity is 300°/s, reaching the outlined 96 Nm and 150°/s outlined criteria. The actual hip moment was not measured; however, moments were enough to successfully propel all three functional testing participants forward, allowing level ground walking.

Geometric constraints were established to ensure the PHP could fit comfortably under a user's pants. The first geometric restriction was that the PHP could not protrude more than 20 mm from the top of the lamination plate. The final device protruded 11 mm anteriorly, passing the criterion. The PHP could also not protrude more than 7.99 cm laterally or 4.99 cm medially from the centre of the lamination plate. 7.2 cm lateral protrusion and 4.7 cm medial protrusion were measured on the final device. The device length was also controlled to ensure a large population could use the device. The final PHP length between the motor centre and the hip joint was 86.75 mm, which was under the 96.5 mm maximum value. Therefore, the PHP met all the geometric constraints.

Finally, the PHP could not have any uncovered finger traps. A cover was designed to go over the pulley system, where the main finger traps occurred. However, the cover no longer fit over the pulleys when the steel cables were used for functional testing. A cover that encompasses the entire device would also be more successful because there is still potential for a finger to be caught between the bearing housing and the lamination plate with the current design. Therefore, this requirement was only partially met and could be improved upon.

The design criteria results are summarized in Table 10-1.

Table 10-1 Outlined design criteria with the actual values from the final PHP design

Criteria	Outlined Limit	Actual Value
Device weight	Maximum 4.0 kg	Measured 3.9 kg
User weight	Maximum 100 kg	Tested with 98 kg user Passed strength tests for 100 kg user
Strength	Withstand 2240 N load for 30 s without failure or deformation > 15 mm Withstand 3360 N load without ductile failure Withstand 2×10^6 cycles between 50 N and 1330 N without failure	Passed static loading tests FEA simulations indicated that device should pass cyclical loading test
Range of motion	Minimum 20° hip extension	22° hip extension (measured with protractor)
	Minimum 130° hip flexion	145° hip flexion (measured with protractor)
Hip moment	Minimum 96 Nm	1:1 gear ratio should provide 96 Nm hip moment, not measured
Angular velocity	Minimum 150 °/s	1:1 gear ratio should provide 300°/s angular velocity, not measured
Anterior protrusion	Maximum 20 mm from top of lamination plate	11 mm (measured with ruler)
Lateral protrusion	Maximum 7.99 cm from centre of lamination plate	7.2 cm (measured with ruler)
Medial protrusion	Maximum 4.99 cm from centre of lamination plate	4.7 cm (measured with ruler)
Device length	Maximum 96.5 mm between the motor centre and the hip joint	86.75 mm (measured with ruler)
User safety	No uncovered finger traps	Cover prevents most finger traps Cover does not fit over steel cables

10.2 Future Work

The novel PHP design met the outlined design criteria and proved successful in allowing able-bodied individuals to walk with a hip disarticulation simulator. However, future work is needed to improve upon the existing design and to further evaluate the device before it can be taken to the market.

10.2.1 Part Optimization

The final PHP met the strength requirements while respecting the geometric and weight restrictions. Further part optimization could reduce the weight and size of the device further. A more lightweight prosthesis requires less energy for the user to walk, and a more compact design would improve user comfort. The current PHP design uses relatively simple geometry; however, tools such as SolidWorks' topology optimization can be used to reduce unnecessary material and optimize the part shapes to provide the required strength with the least weight. The parts can also be redesigned to improve aesthetics.

10.2.2 Control System Implementation

A simple control system with a repeated gait cycle was used for the functional testing. The final device will use sensors with a complex control system to identify user gait initiation and adjust gait parameters based on pelvic motion. The control system is currently under development and will allow users to control PHP gait when it is implemented into the system, instead of following a predetermined cycle.

10.2.3 Cable Solution

As noted in Chapter 9:, the initial spliced Vectran ropes used with the pulleys stretched when the motor was operated, developing slack into the system. Steel cables were used for the functional testing; however, these cables do not have an adequate tensile strength and must be crimped in a way that protrudes from the pulleys, prevents the cover from being placed over the pulleys, and is not aesthetically pleasing. A separate project has been introduced to investigate the best solution for the rope to be used with the pulleys. The new solution must not stretch under tension and must fit neatly with the pulleys. The pulleys may also have to be redesigned to suit the new cable solution.

10.2.4 Cyclical Testing

The mechanical testing done in this thesis featured only static tests. FEA simulations indicated that the PHP should be able to withstand the cyclical testing outlined in ISO 15032:2000; however, to ensure that the PHP will last long term and not fail under fatigue, the cyclical tests should be performed on the device.

10.2.5 Amputee Testing

The PHP showed promise in the HKAF prosthesis simulator functional testing with able-bodied individuals. However, the goal is for the device to be used by actual amputees. Therefore, to ensure that the device is suitable for hip disarticulation and hemipelvectomy amputees, the next prototype will need to be tested by volunteers with these amputations. This should occur after the other issues have been resolved.

References

[1] M. Windrich, M. Grimmer, O. Christ, S. Rinderknecht, and P. Beckerle, "Active lower limb prosthetics: a systematic review of design issues and solutions," *Biomed. Eng. OnLine*, vol. 15, no. Suppl 3, Dec. 2016, doi: 10.1186/s12938-016-0284-9.

[2] R. L. Waters, J. Perry, D. Antonelli, and H. Hislop, "Energy cost of walking of amputees: the influence of level of amputation," *J. Bone Joint Surg. Am.*, vol. 58, no. 1, pp. 42–46, Jan. 1976.

[3] "Hip Disarticulation and Hemipelvectomy ‹ News - Kenney Orthopedics - Orthotics & Prosthetics." https://www.kenneyorthopedics.com/about/news/view/592/hip-disarticulation-and-hemipelvectomy (accessed Nov. 30, 2019).

[4] E. Ludwigs, M. Bellmann, T. Schmalz, and S. Blumentritt, "Biomechanical differences between two exoprosthetic hip joint systems during level walking," *Prosthet. Orthot. Int.*, vol. 34, no. 4, pp. 449–460, 2010, doi: 10.3109/03093646.2010.499551.

[5] M. Grimmer and A. Seyfarth, "Mimicking Human-Like Leg Function in Prosthetic Limbs," 2014, pp. 105–155. doi: 10.1007/978-94-017-8932-5_5.

[6] R. L. Waters and S. Mulroy, "The energy expenditure of normal and pathologic gait," *Gait Posture*, vol. 9, no. 3, pp. 207–231, Jul. 1999, doi: 10.1016/S0966-6362(99)00009-0.

[7] "Helix 3D Hip Joint System: Clinical Study Summaries." Otto Bock Clinical Research & Services.

[8] H. Gholizadeh, N. Baddour, M. Botros, K. Brannen, F. Golshan, and E. Lemaire, "Hip disarticulation and hemipelvectomy prostheses: A review of the literature," *Prosthet. Orthot. Int.*, vol. Publish Ahead of Print, Sep. 2021, doi: 10.1097/PXR.0000000000000029.

[9] D. Neumann, *Kinesiology of the Musculoskeletal System: Foundations for Rehabilitation*, 2nd ed. St Louis: Mosby, 2010.

[10] A. D. Segal *et al.*, "Kinematic and kinetic comparisons of transfemoral amputee gait using C-Leg and Mauch SNS prosthetic knees," *J. Rehabil. Res. Dev.*, vol. 43, no. 7, pp. 857–869, Dec. 2006.

[11] "Steeper LPC - C-Leg 4," *Steeper LPC*. https://www.thelondonprosthetics.com/Prosthetic-Solutions/Lower-Limb/Microprocessor-knees/C-Leg-4 (accessed Aug. 20, 2023).

[12] "Ossur: Mauch Knee SNS (K3) | Prosthetic Solutions." https://prostheticsolutions.com/components/ossur-mauch-knee-sns-k3/ (accessed Aug. 20, 2023).

[13] P. M. Dall and A. Kerr, "Frequency of the sit to stand task: An observational study of free-living adults," *Appl. Ergon.*, vol. 41, no. 1, pp. 58–61, Jan. 2010, doi: 10.1016/j.apergo.2009.04.005.

[14] M. J. Highsmith *et al.*, "Kinetic asymmetry in transfemoral amputees while performing sit to stand and stand to sit movements," *Gait Posture*, vol. 34, no. 1, pp. 86–91, May 2011, doi: 10.1016/j.gaitpost.2011.03.018.

[15] M. J. Highsmith *et al.*, "Correlations between residual limb length and joint moments during sitting and standing movements in transfemoral amputees," *Prosthet. Orthot. Int.*, vol. 40, no. 4, pp. 522–527, Aug. 2016, doi: 10.1177/0309364614564025.

[16] T. Schmalz, S. Blumentritt, and B. Marx, "Biomechanical analysis of stair ambulation in lower limb amputees," *Gait Posture*, vol. 25, no. 2, pp. 267–278, Feb. 2007, doi: 10.1016/j.gaitpost.2006.04.008.

[17] E. Wolf, V. Everding, A. Linberg, B. Schnall, J. Czerniecki, and J. Gambel, "Assessment of transfemoral amputees using C-Leg and Power Knee for ascending and descending inclines

and steps," *J. Rehabil. Res. Dev.*, vol. 49, pp. 831–42, Aug. 2012, doi: 10.1682/JRRD.2010.12.0234.
[18] N. C. Buell, L. L. Willingham, K. J. Allyn, B. J. Hafner, D. G. Smith, and D. Boone, "Evaluation of gait style to ascend and descend stairs for lower limb amputees," *Proc. 11th World Congr. Int. Soc. Prosthet. Orthot.*, p. 367, 2004.
[19] B. J. Hafner, L. L. Willingham, N. C. Buell, K. J. Allyn, and D. G. Smith, "Evaluation of Function, Performance, and Preference as Transfemoral Amputees Transition From Mechanical to Microprocessor Control of the Prosthetic Knee," *Arch. Phys. Med. Rehabil.*, vol. 88, no. 2, pp. 207–217, Feb. 2007, doi: 10.1016/j.apmr.2006.10.030.
[20] S. Hamamura *et al.*, "Factors affecting prosthetic rehabilitation outcomes in amputees of age 60 years and over," *J. Int. Med. Res.*, vol. 37, no. 6, pp. 1921–1927, Dec. 2009, doi: 10.1177/147323000903700630.
[21] C. A. McLaurin, "Hip Disarticulation prosthesis," Prosthetic Services Centre, Department of Veterans Affairs, Toronto, 15, 1954.
[22] S. E. Solomonidis, A. J. Loughran, J. Taylor, and J. P. Paul, "Biomechanics of the hip disarticulation prosthesis," *Prosthet. Orthot. Int.*, vol. 1, no. 1, pp. 13–18, Apr. 1977, doi: 10.3109/03093647709164599.
[23] C. W. Radcliffe, "The Biomechanics of the Canadian-Type Hip-Disarticulation Prosthesis," *Artif. Limbs*, vol. 4, no. 2, pp. 29–38, 1957.
[24] H. Iwakura, M. Abe, H. Fujinaga, S. Kakurai, and H. Yano, "Locomotion of the hemipelvectomy amputee," *Prosthet. Orthot. Int.*, vol. 3, no. 2, pp. 111–114, 1979.
[25] B. L. Schnall, B. S. Baum, and A. M. Andrews, "Gait Characteristics of a Soldier With a Traumatic Hip Disarticulation," *Phys. Ther.*, vol. 88, no. 12, pp. 1568–1577, Dec. 2008, doi: 10.2522/ptj.20070337.
[26] J. Perry, "Chapter 13 - Normal Gait," in *Atlas of Limb Prosthetics: Surgical, Prosthetic, and Rehabilitation Principles*, 2nd ed.Mosby, 1992.
[27] M. W. Whittle, "Chapter 2 - Normal gait," in *Gait Analysis (Fourth Edition)*, M. W. Whittle, Ed., Edinburgh: Butterworth-Heinemann, 2007, pp. 47–100. doi: 10.1016/B978-075068883-3.50007-6.
[28] G. Stark, "Overview of Hip Disarticulation Prostheses," *JPO J. Prosthet. Orthot.*, vol. 13, no. 2, p. 50, Jun. 2001.
[29] T. Van der Waarde and J. Michael, "Chapter 21B - Hip Disarticulation and Transpelvic Amputation: Prosthetic Management," in *Atlas of Limb Prosthetics: Surgical, Prosthetic, and Rehabilitation Principles*, 2nd ed.Mosby, 1992.
[30] T. Chin, S. Sawamura, R. Shiba, H. Oyabu, Y. Nagakura, and A. Nakagawa, "Energy expenditure during walking in amputees after disarticulation of the hip," *J. Bone Joint Surg. Br.*, vol. 87-B, no. 1, pp. 117–119, Jan. 2005, doi: 10.1302/0301-620X.87B1.14617.
[31] S. Blumentritt, E. Ludwigs, M. Bellmann, and H. Boiten, "The New Helix3D Hip Joint," p. 6.
[32] "Prosthetic leg in India, Artificial limbs in India, Artificial limb supplier, Prosthetic support, Orthotic support." https://www.karepoindia.com/paediatric-ctch-hip.html (accessed Aug. 20, 2023).
[33] E. Gailledrat *et al.*, "Does the new Helix 3D hip joint improve walking of hip disarticulated amputees?," *Ann. Phys. Rehabil. Med.*, vol. 56, no. 5, pp. 411–418, 2013, doi: 10.1016/j.rehab.2013.05.001.

[34] Y. Ueyama, T. Kubo, and M. Shibata, “Robotic hip-disarticulation prosthesis: evaluation of prosthetic gaits in a non-amputee individual,” *Adv. Robot.*, vol. 34, no. 1, pp. 37–44, 2020, doi: 10.1080/01691864.2019.1705908.
[35] M. K. Ishmael, D. Archangeli, and T. Lenzi, “Powered hip exoskeleton improves walking economy in individuals with above-knee amputation,” *Nat. Med.*, vol. 27, no. 10, Art. no. 10, Oct. 2021, doi: 10.1038/s41591-021-01515-2.
[36] R. C. Browning, J. R. Modica, R. Kram, and A. Goswami, “The Effects of Adding Mass to the Legs on the Energetics and Biomechanics of Walking,” *Med. Sci. Sports Exerc.*, vol. 39, no. 3, pp. 515–525, Mar. 2007, doi: 10.1249/mss.0b013e31802b3562.
[37] “Power Knee PKA01: Instructions for Use.” Össur.
[38] “Hip prosthesis with: Helix 3D,” *OttoBock*. https://www.ottobock.ca/en/prosthetics/lower-limb-prosthetics/solution-overview/helix-hip-system/ (accessed Feb. 06, 2022).
[39] T. Van der Waarde, “Ottawa Experience With Hip Disarticulation Prostheses,” *Orthot. Prosthet.*, vol. 38, no. 1, pp. 29–35, 1984.
[40] “How much will my lower limb prosthesis weigh?,” *De La Torre Orthotics & Prosthetics*. https://www.delatorreop.com/faq/how-much-will-my-lower-limb-prosthesis-weigh/ (accessed Feb. 13, 2022).
[41] P. de Leva, “Adjustments to Zatsiorsky-Seluyanov’s segment inertia parameters,” *J. Biomech.*, vol. 29, no. 9, pp. 1223–1230, Sep. 1996, doi: 10.1016/0021-9290(95)00178-6.
[42] National Center for Health Statistics, “Anthropometric Reference Data for Children and Adults: United States, 2015-2018,” *US Dep. Health Hum. Serv.*, no. 46, Jan. 2021.
[43] “Prostheses - Structural testing of hip units.” International Organization for Standardization, Apr. 15, 2000.
[44] R. L. Bona, N. A. Gomeñuka, J. L. L. Storniolo, A. Bonezi, and C. M. Biancardi, “Self-selected walking speed in individuals with transfemoral amputation: recovery, economy and rehabilitation index,” *Eur. J. Physiother.*, vol. 22, no. 3, pp. 133–140, May 2020, doi: 10.1080/21679169.2018.1561941.
[45] E. Russell Esposito, C. A. Rábago, and J. Wilken, “The influence of traumatic transfemoral amputation on metabolic cost across walking speeds,” *Prosthet. Orthot. Int.*, vol. 42, no. 2, pp. 214–222, Apr. 2018, doi: 10.1177/0309364617708649.
[46] B. J. Darter, D. H. Nielsen, H. J. Yack, and K. F. Janz, “Home-Based Treadmill Training to Improve Gait Performance in Persons With a Chronic Transfemoral Amputation,” *Arch. Phys. Med. Rehabil.*, vol. 94, no. 12, pp. 2440–2447, Dec. 2013, doi: 10.1016/j.apmr.2013.08.001.
[47] C. Gordon *et al.*, “1988 Anthropometric Survey of U.S. Army Personnel: Methods and Summary Statistics,” United States Army Natick Research, Development and Engineering Center, Natick, Massachusetts, Technical Report Natick/TR-89/044, Sep. 1989. [Online]. Available: http://mreed.umtri.umich.edu/mreed/downloads/anthro/ansur/Gordon_1989.pdf
[48] “7E10 Helix3D.” Ottobock.
[49] “National Health and Nutrition Examination Survey 2015-2016.” Centers for Disease Control and Prevention, 2016. [Online]. Available: https://wwwn.cdc.gov/nchs/nhanes/continuousnhanes/default.aspx?BeginYear=2015
[50] R. Drillis and R. Contini, “Body Segment Parameters,” Office of Vocational Rehabilitation, New York, New York, 1166–03, 1966.
[51] “Otto Bock Helix Hip Joint System,” *MCOP Prosthetics*. https://mcopro.com/prosthetics/technology/ottobock-helix-hip/ (accessed Dec. 15, 2020).

[52] “Ossur Adapters.” Ossur. [Online]. Available: https://media.ossur.com/image/upload/product-documents-global/Height_Adjustable_Pylon_us_en_PN20348.pdf
[53] T. M. Köhler, M. Bellmann, and s Blumentritt, “Polycentric Exoprosthetic Knee Joints - Extent of Shortening during Swing Phase,” *Can. Prosthet. Orthot. J.*, vol. 3, no. 1, Jul. 2020, doi: 10.33137/cpoj.v3i1.33768.
[54] M. P. Greene, “Four Bar Linkage Knee Analysis,” *Orthot. Prosthet.*, vol. 37, no. 1, pp. 15–24, 1983.
[55] K. Johnson and A. J. Davis, “Prosthetic Restoration and Management of Transitibial, Transfemoral, and Hip Disarticulation/Hemipelvectomy Amputations,” in *Prosthetic Restoration and Rehabilitation of the Upper and Lower Extremity*, Demos Medical Publishing, 2013, pp. 87–97.
[56] C. W. Radcliffe, “Above-knee prosthetics,” *Prosthet. Orthot. Int.*, vol. 1, no. 3, pp. 146–160, Dec. 1977, doi: 10.3109/03093647709164629.
[57] “Power Knee™ | Motor-powered Prosthetic Knee | Bionic Knee.” https://www.ossur.com/en-ca/prosthetics/knees/power-knee (accessed Aug. 22, 2023).
[58] Ottobock, “Hip prosthesis with: Helix 3D | Ottobock US.” https://www.ottobockus.com/products/helix-hip-system/ (accessed Apr. 06, 2022).
[59] R. Juvinall and K. Marshek, “Chapter 15 Spur Gears,” in *Fundamentals of Machine Component Design*, 5th ed.Wiley, 2012, pp. 620–674.
[60] R. Juvinall and K. Marshek, “Chapter 8 Fatigue,” in *Fundamentals of Machine Component Design*, 5th ed.Wiley, 2012, pp. 312–371.
[61] R. Juvinall and K. Marshek, “Chapter 16 Helical, Bevel, and Worm Gears,” in *Fundamentals of Machine Component Design*, 5th ed.Wiley, 2012, pp. 675–715.
[62] “High Performance Polyurethane Timing Belts and Pulleys.” BRECOflex Co., L.L.C. Accessed: Jun. 01, 2022. [Online]. Available: https://brecoflex-co-llc.dcatalog.com/v/B212-Polyurethane-Timing-Belts/brecoflex-co-llc.dcatalog.com/v/B212-Polyurethane-Timing-Belts/
[63] “Technical Engineering - General Drive Considerations.” Diamond Chain Company. [Online]. Available: https://www.diamondchain.com/wp-content/uploads/2017/03/TechnicalEngineering.pdf
[64] “Diamond Standard Series Chain.” Diamond Chain Company. [Online]. Available: https://www.diamondchain.com/wp-content/uploads/2016/10/Diamond-Standard-Series-1.pdf
[65] “Rope Materials,” *Premium Ropes*. https://www.premiumropes.com/rope-advice/rope-materials (accessed Mar. 14, 2022).
[66] “Technical Information.” Alpha Ropes. [Online]. Available: https://www.alpha-ropes.com/en/downloads/file191_gb.pdf
[67] “Rope Materials,” *Marlow Ropes*, Sep. 20, 2016. https://www.marlowropes.com/material-types (accessed Mar. 14, 2022).
[68] “Vectran,” *FibrXL*. https://fibrxl.com/fibrxl-performance/fibers/vectran/ (accessed Mar. 14, 2022).
[69] “A Beginner’s Guide to Splicing Ropes,” *Ropes Direct*, Apr. 27, 2020. https://www.ropesdirect.co.uk/blog/a-beginners-guide-to-splicing-rope/ (accessed Mar. 14, 2022).

[70] J. Hartter and J. Garland, “Synthetic Rope End Connections for Use in Timber Harvesting,” *Int. J. For. Eng.*, vol. 17, no. 1, pp. 39–51, Jan. 2006, doi: 10.1080/14942119.2006.10702528.
[71] “How to Splice Rope,” *Samson Rope*. https://www.samsonrope.com/resources/how-to-splice-rope (accessed Mar. 14, 2022).
[72] “Splicing,” *Cordage Institute*. https://www.ropecord.com/new/splicing.php (accessed Mar. 14, 2022).
[73] “17-4 PH Stainless Steel Product Data Sheet.” AK Steel Corporation, Jul. 2007.
[74] “2024 Aluminum Alloy: Properties.” Gabrian International Ltd. [Online]. Available: https://www.gabrian.com/wp-content/uploads/2018/10/2024-Aluminum-Alloy-Properties.pdf
[75] “Marlow Excel V12 3mm 12-Strand Vectran 3mm,” *The Chandlery Marine Supplies*. https://www.thechandleryonline.com/product_info.php?products_id=2572 (accessed Oct. 05, 2022).
[76] R. G. Budynas and J. K. Nisbett, “Shafts and Shaft Components,” in *Shigley’s Mechanical Engineering Design*, 9th ed.McGraw-Hill, 2011, pp. 359–408.
[77] R. G. Budynas and J. K. Nisbett, “Load and Stress Analysis,” in *Shigley’s Mechanical Engineering Design*, 9th ed.McGraw-Hill, 2011, pp. 265–356.
[78] R. G. Budynas and J. K. Nisbett, “Charts of Theoretical Stress-Concentration Factors,” in *Shigley’s Mechanical Engineering Design*, 9th ed.McGraw-Hill, 2011, pp. 1026–1032.
[79] R. G. Budynas and J. K. Nisbett, “Fatigue Failure Resulting from Variable Loading,” in *Shigley’s Mechanical Engineering Design*, 9th ed.McGraw-Hill, 2011, pp. 265–356.
[80] R. Juvinall and K. Marshek, “Chapter 10 Threaded Fasteners and Power Screws,” in *Fundamentals of Machine Component Design*, 5th ed.Wiley, 2012, pp. 411–471.
[81] “Galvanized Steel Wire Rope - Not for Lifting,” *McMaster-Carr*. https://www.mcmaster.com/3450T38/ (accessed Apr. 07, 2023).
[82] A. Fanous, M. Botros, H. Gholizadeh, N. Baddour, and E. Lemaire, “Design and evaluation of a hip prosthesis simulator: A technical note,” *Prosthet. Orthot. Int.*, vol. 2023, Feb. 2023, doi: 10.1097/PXR.0000000000000208.
[83] “Kinovea.” https://www.kinovea.org/ (accessed Apr. 05, 2023).

Appendix A – Mechanical Drawings

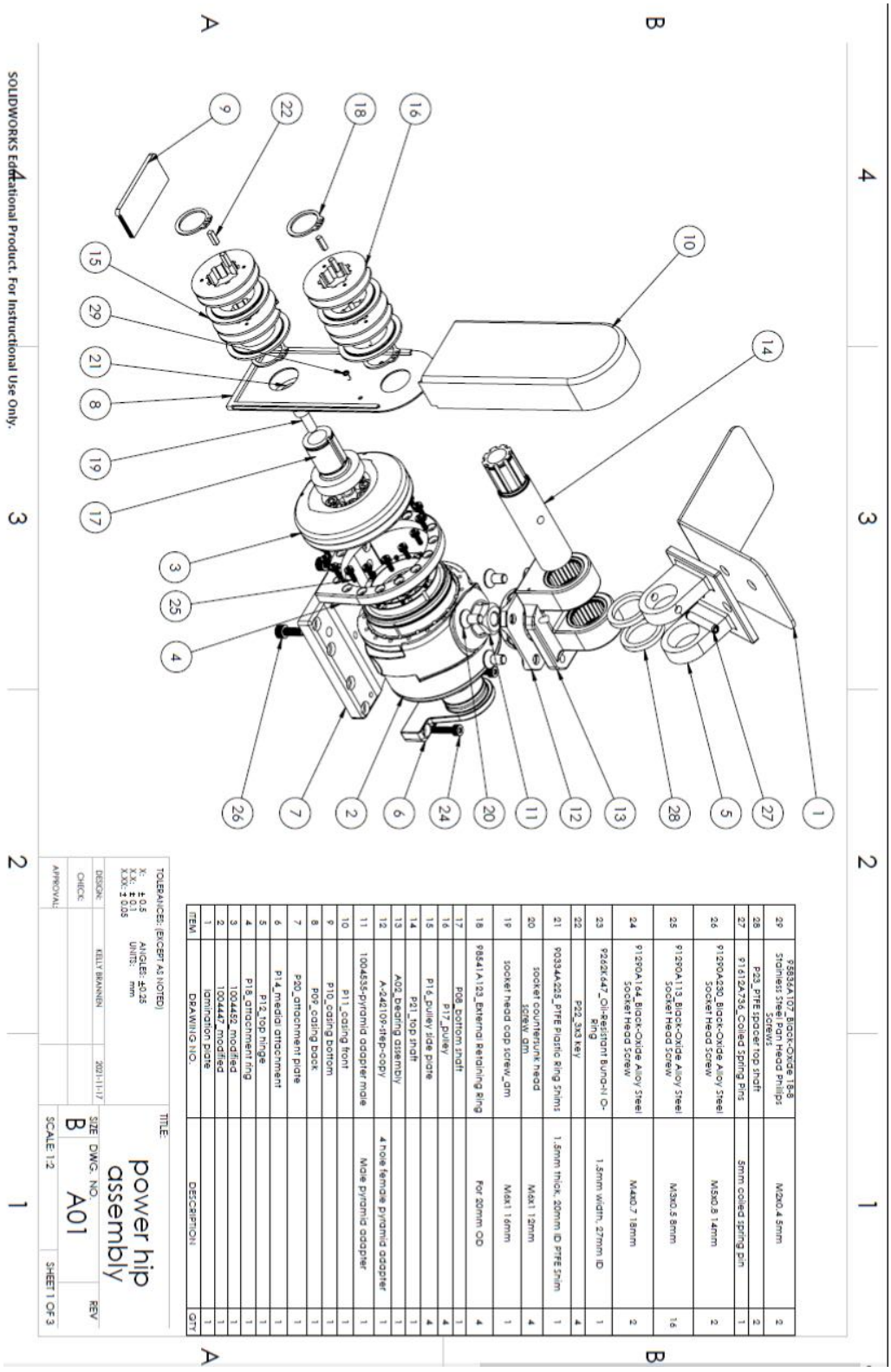

ITEM	DRAWING NO.	DESCRIPTION	QTY
29	95883A107_Black-Oxide 18-8 Stainless Steel Pan Head Phillips Screws	M2x0.4 5mm	2
28	P23_PTFE spacer top shaft		2
27	91612A736_Coiled Spring Pins	5mm coiled spring pin	1
26	91290A230_Black-Oxide Alloy Steel Socket Head Screw	M5x0.8 14mm	2
25	91290A113_Black-Oxide Alloy Steel Socket Head Screw	M3x0.5 8mm	16
24	91290A164_Black-Oxide Alloy Steel Socket Head Screw	M4x0.7 18mm	2
23	9262K647_Oil-Resistant Buna-N O-Ring	1.5mm width, 27mm ID	1
22	P22_3x3 key		4
21	90394A225_PTFE Plastic Ring Shims	1.5mm thick, 20mm ID PTFE Shim	1
20	socket countersunk head screw_gtm	M4x1 12mm	4
19	socket head cap screw_gtm	M4x1 16mm	1
18	98641A132_External Retaining Ring	For 20mm OD	4
17	P08_bottom shaft		1
16	P17_pulley		4
15	P16_pulley side plate		4
14	P21_top shaft		1
13	A02_bearing assembly		1
12	A-240106-step-copy	4 hole female pyramid adapter	1
11	100455-pyramid adapter male	Male pyramid adapter	1
10	P11_casing front		1
9	P10_casing bottom		1
8	P09_casing back		1
7	P20_attachment plate		1
6	P14_medial attachment		1
5	P12_top hinge		1
4	P18_attachment ring		1
3	100445Z_modified		1
2	100444Z_modified		1
1	lamination plate		1

TOLERANCES: (EXCEPT AS NOTED)
X: ± 0.5 ANGLES: ±0.25
XX: ± 0.1 UNITS: mm
XXX: ± 0.05

DESIGN: KELLY BRANNEN 2021-11-17
CHECK:
APPROVAL:

TITLE: power hip assembly

SIZE B DWG. NO. A01 REV

SCALE: 1:2 SHEET 1 OF 3

SOLIDWORKS Educational Product. For Instructional Use Only.

Figure A-01 Power hip assembly drawing a

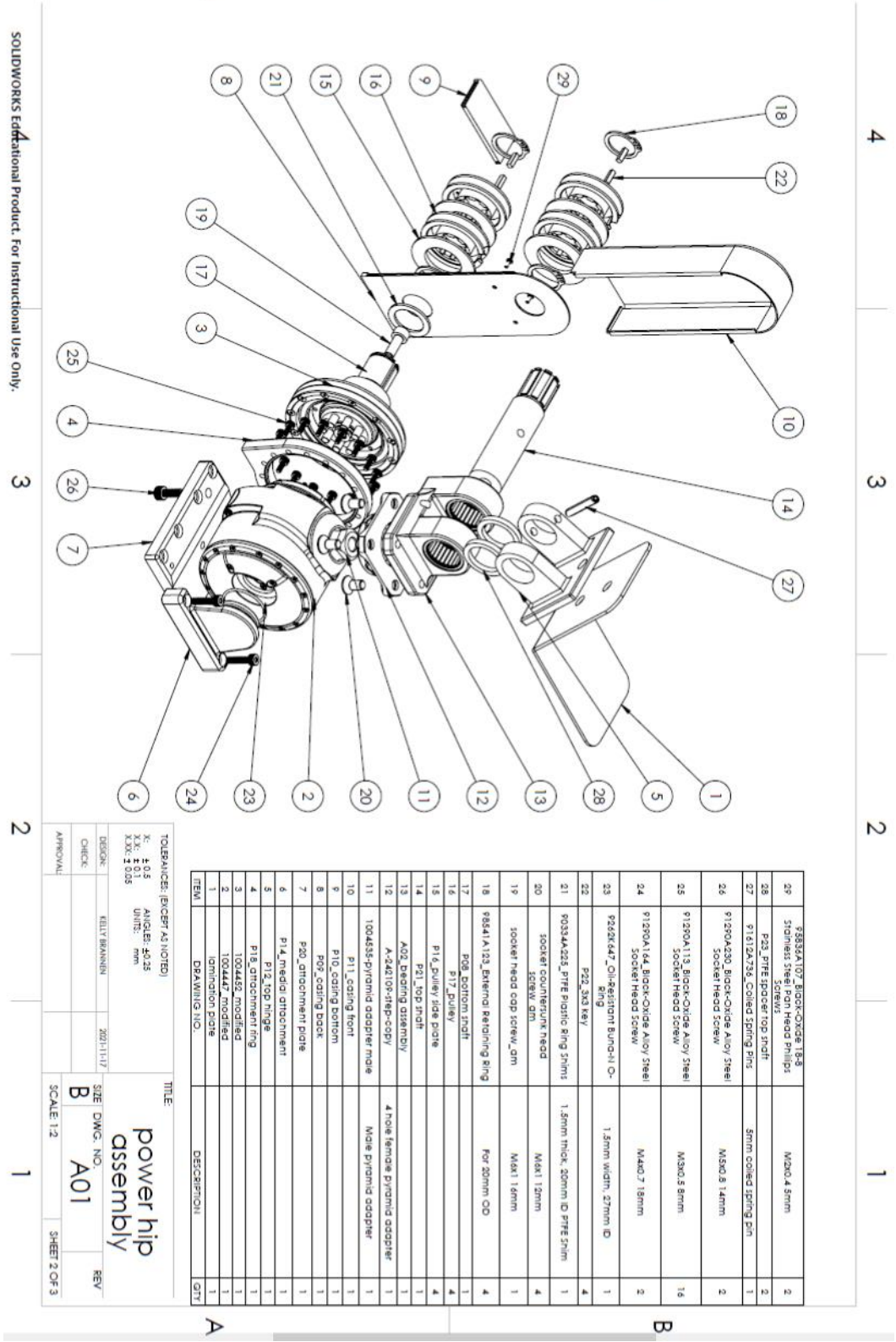

Figure A-02 Power hip assembly drawing b

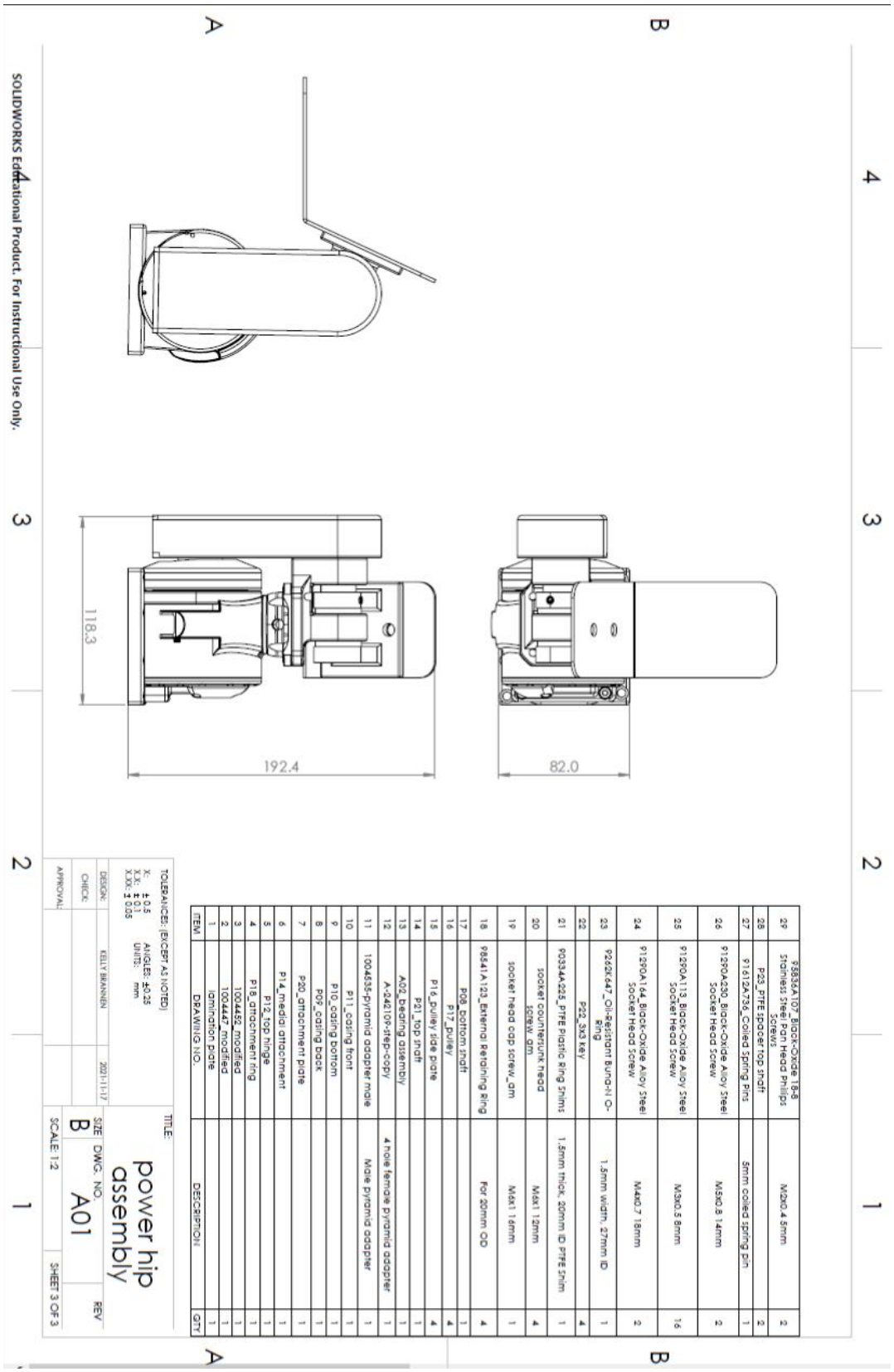

ITEM	DESCRIPTION	QTY
29	98836A107_Black-Oxide 18-8 Stainless Steel Pan Head Phillips Screws	M2x0.4 5mm	2
28	P23_PTFE spacer top shaft		2
27	91612A734_Coiled Spring Pins	5mm coiled spring pin	1
26	91290A030_Black-Oxide Alloy Steel Socket Head Screw	M5x0.8 14mm	2
25	91290A113_Black-Oxide Alloy Steel Socket Head Screw	M3x0.5 8mm	16
24	91290A164_Black-Oxide Alloy Steel Socket Head Screw	M4x0.7 18mm	2
23	9262K447_Oil-Resistant Buna-N O-Ring	1.5mm width, 27mm ID	1
22	P22_3x3 key		4
21	90334A225_PTFE Plastic Ring Shims	1.5mm thick, 20mm ID PTFE Shim	1
20	socket countersunk head screw_am	M4x1 12mm	4
19	socket head cap screw_am	M4x1 16mm	1
18	98641A123_External Retaining Ring	For 20mm OD	4
17	P08_bottom shaft		1
16	P17_pulley		1
15	P16_pulley side plate		4
14	P21_top shaft		4
13	A02_bearing assembly		1
12	A-240109-step-copy	4 hole female pyramid adapter	1
11	1004535-pyramid adapter male	Male pyramid adapter	1
10	P11_casing front		1
9	P10_casing bottom		1
8	P09_casing back		1
7	P20_attachment plate		1
6	P14_medial attachment		1
5	P12_top hinge		1
4	P18_attachment ring		1
3	1004452_modified		1
2	1004447_modified		1
1	lamination plate		1

TOLERANCES: (EXCEPT AS NOTED)
X: ± 0.5
X.X: ± 0.1
X.XX: ± 0.05
ANGLES: ±0.25
UNITS: mm

DESIGN:
CHECK:
APPROVAL:

TITLE:

SIZE: B
DWG. NO.: A01
REV:

Figure A-03 Power hip assembly drawing c

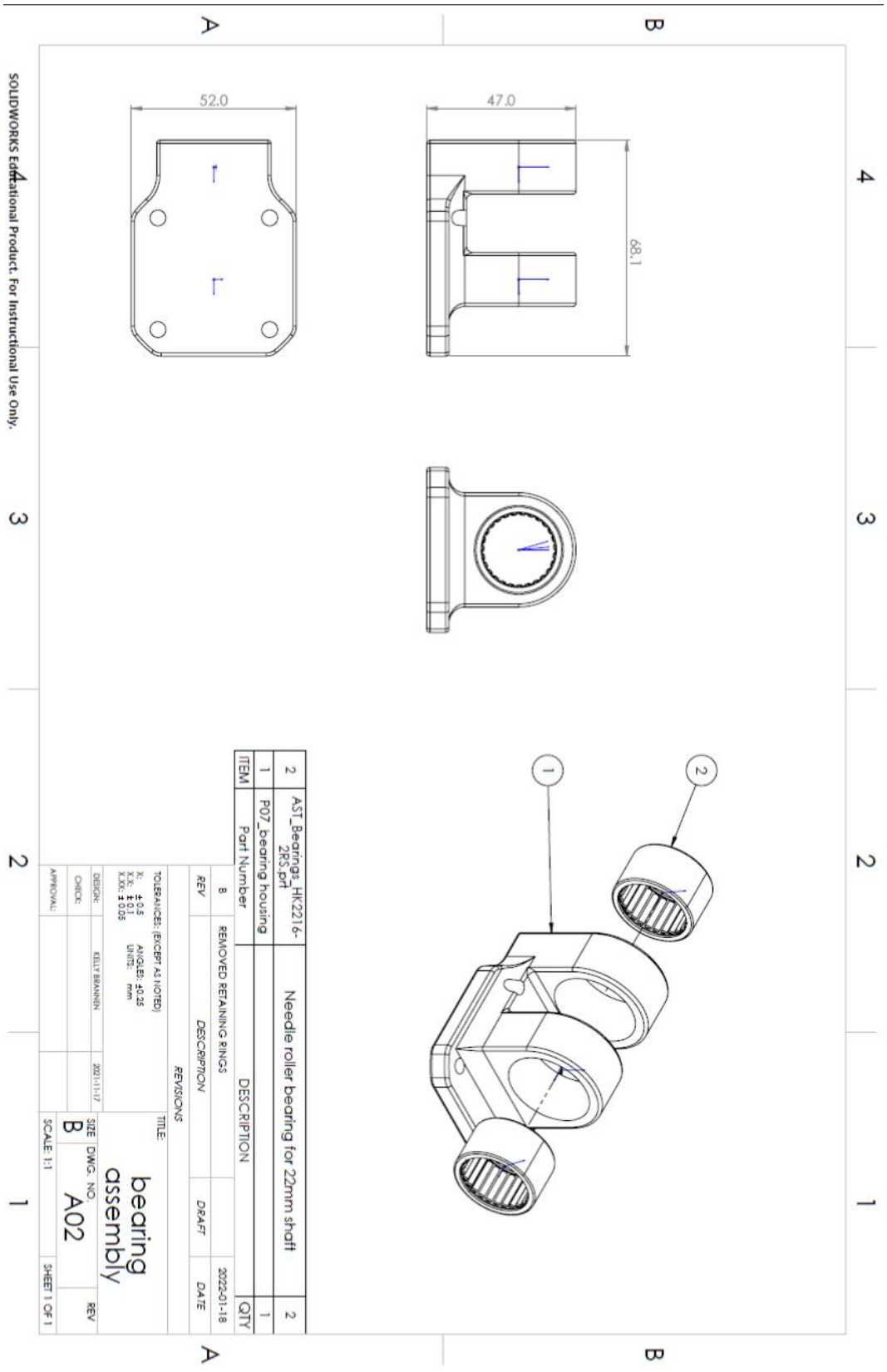

Figure A-04 Bearing assembly drawing

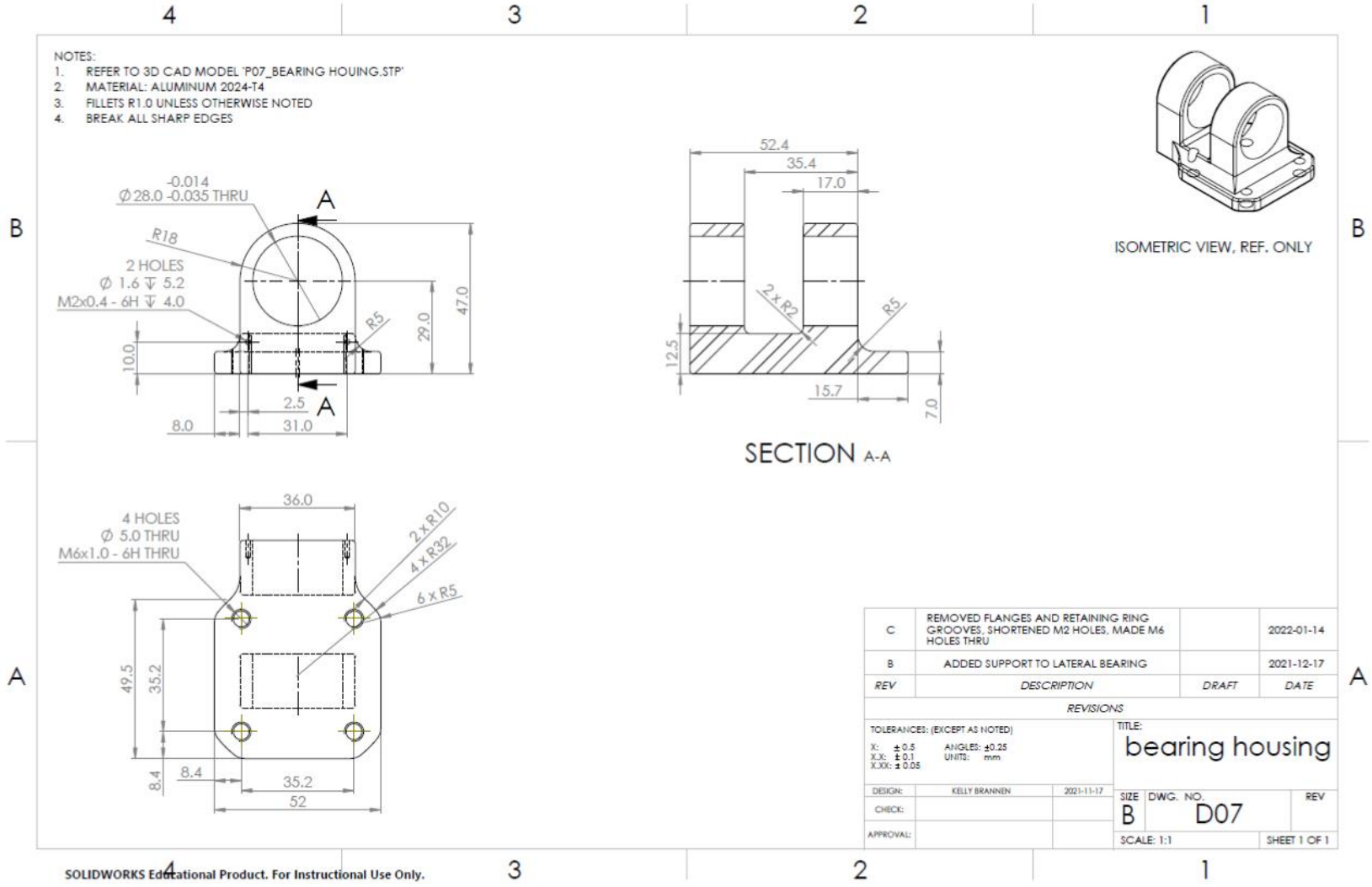

Figure A-05 Bearing housing drawing

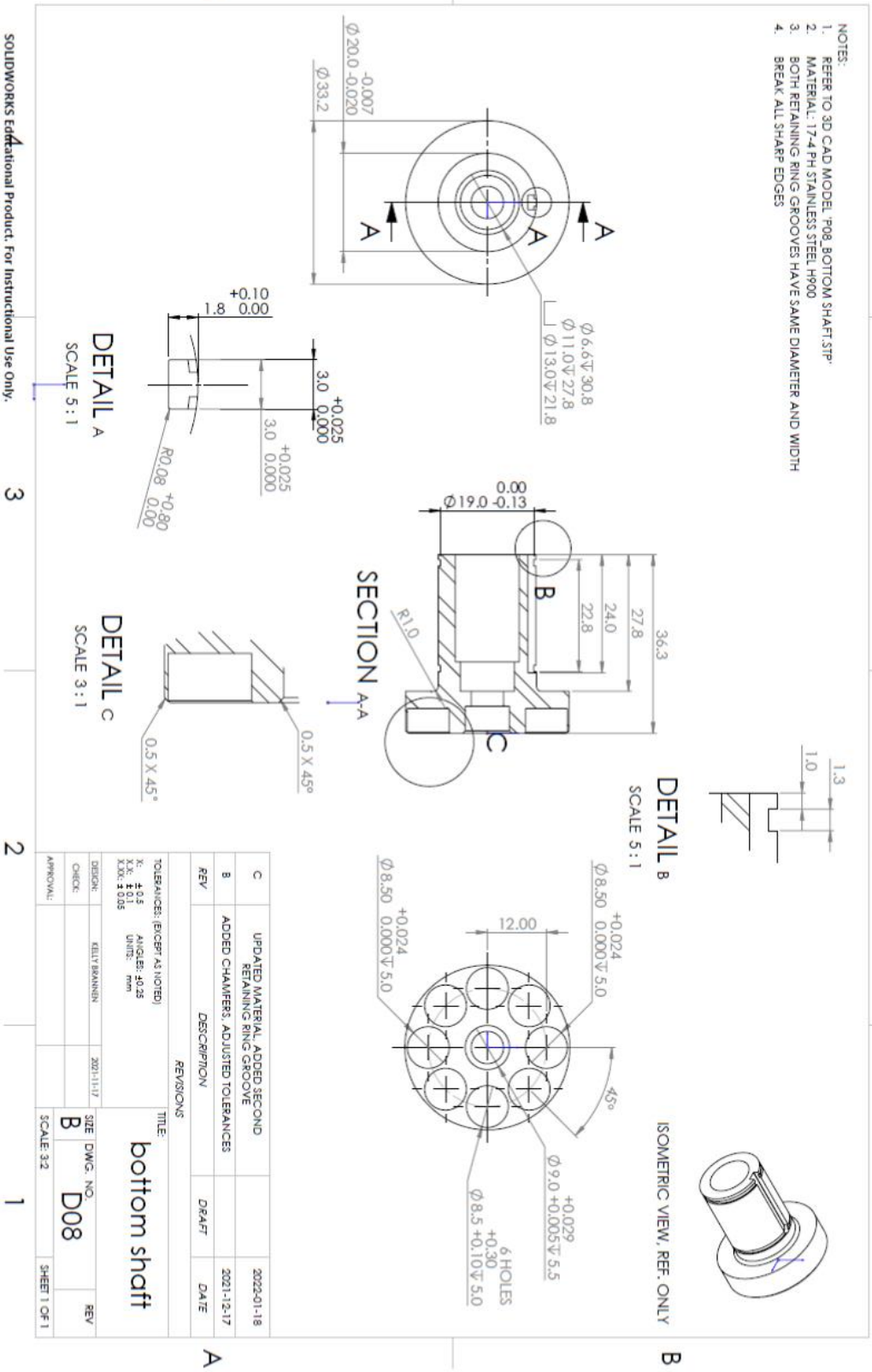

Figure A-06 Bottom shaft drawing

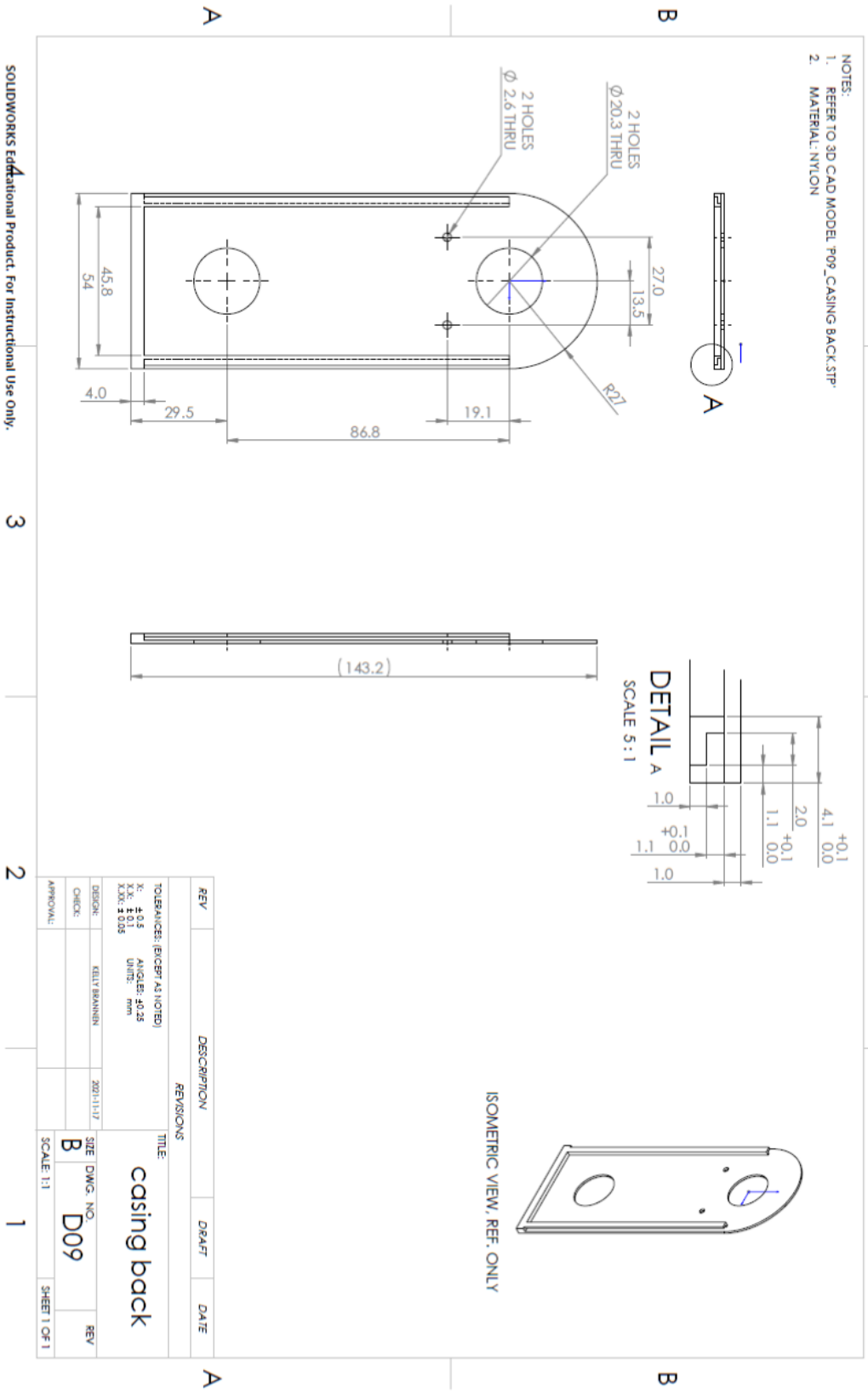

Figure A-07 Casing back drawing

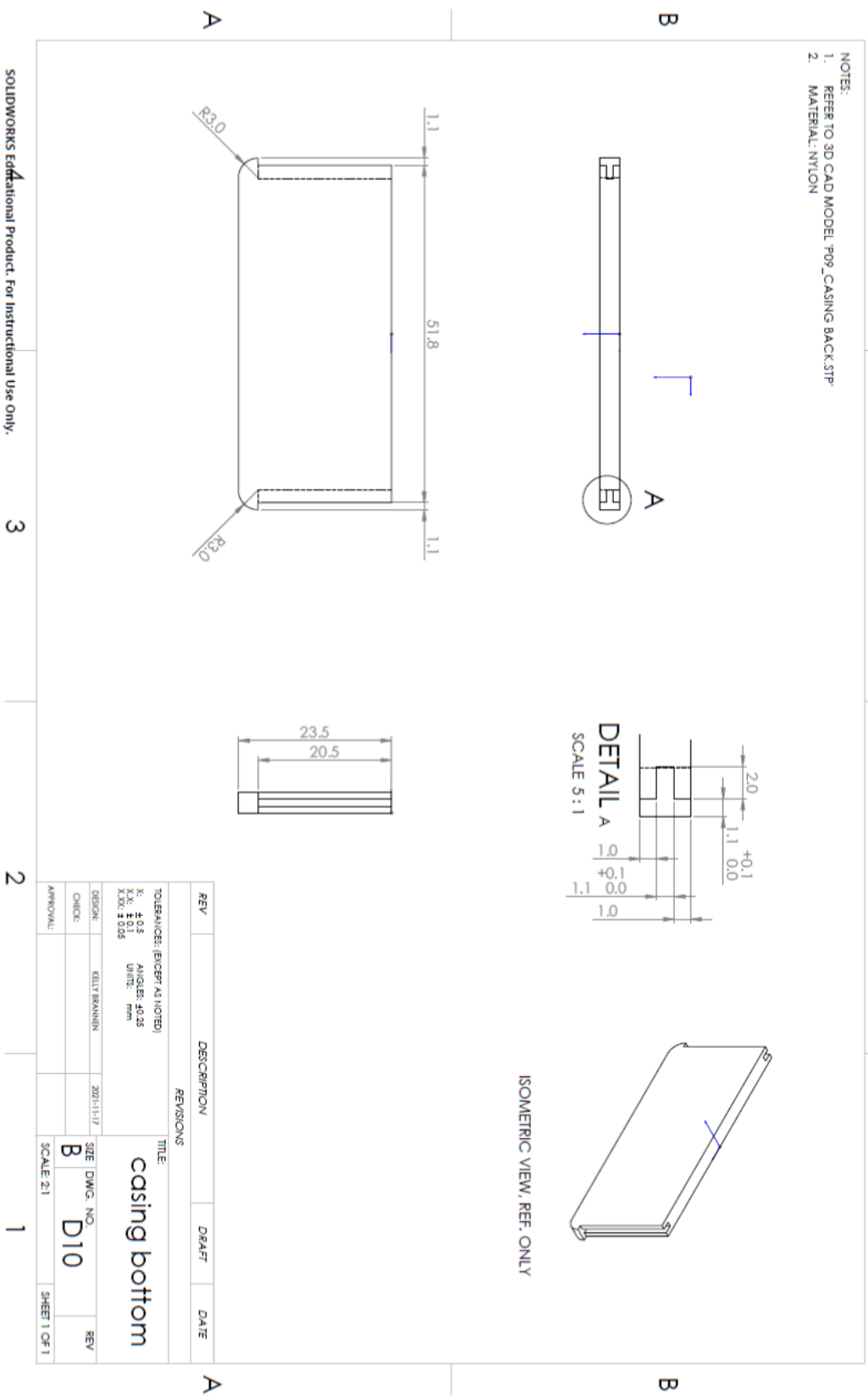

Figure A-08 Casing bottom drawing

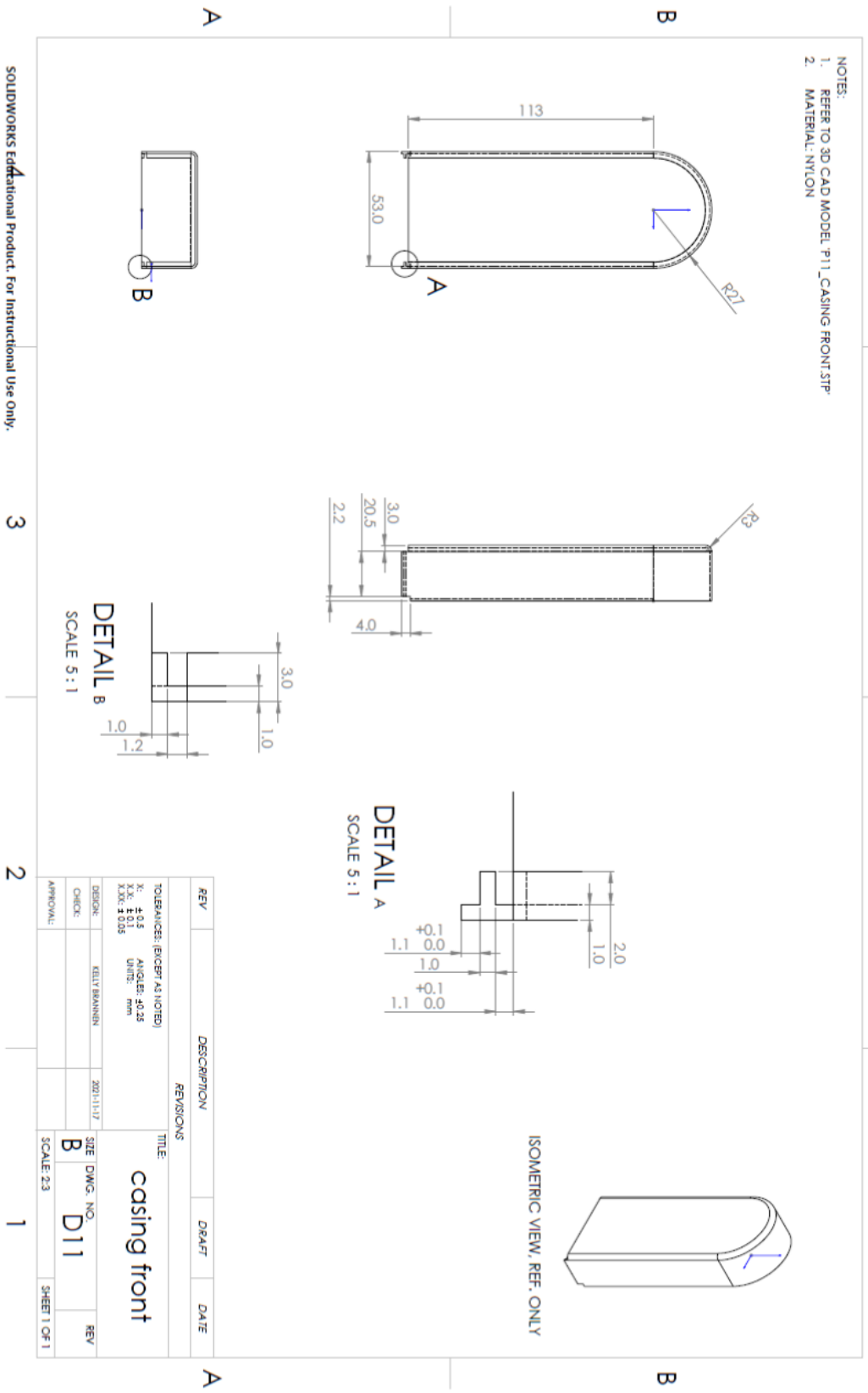

Figure A-09 Casing front drawing

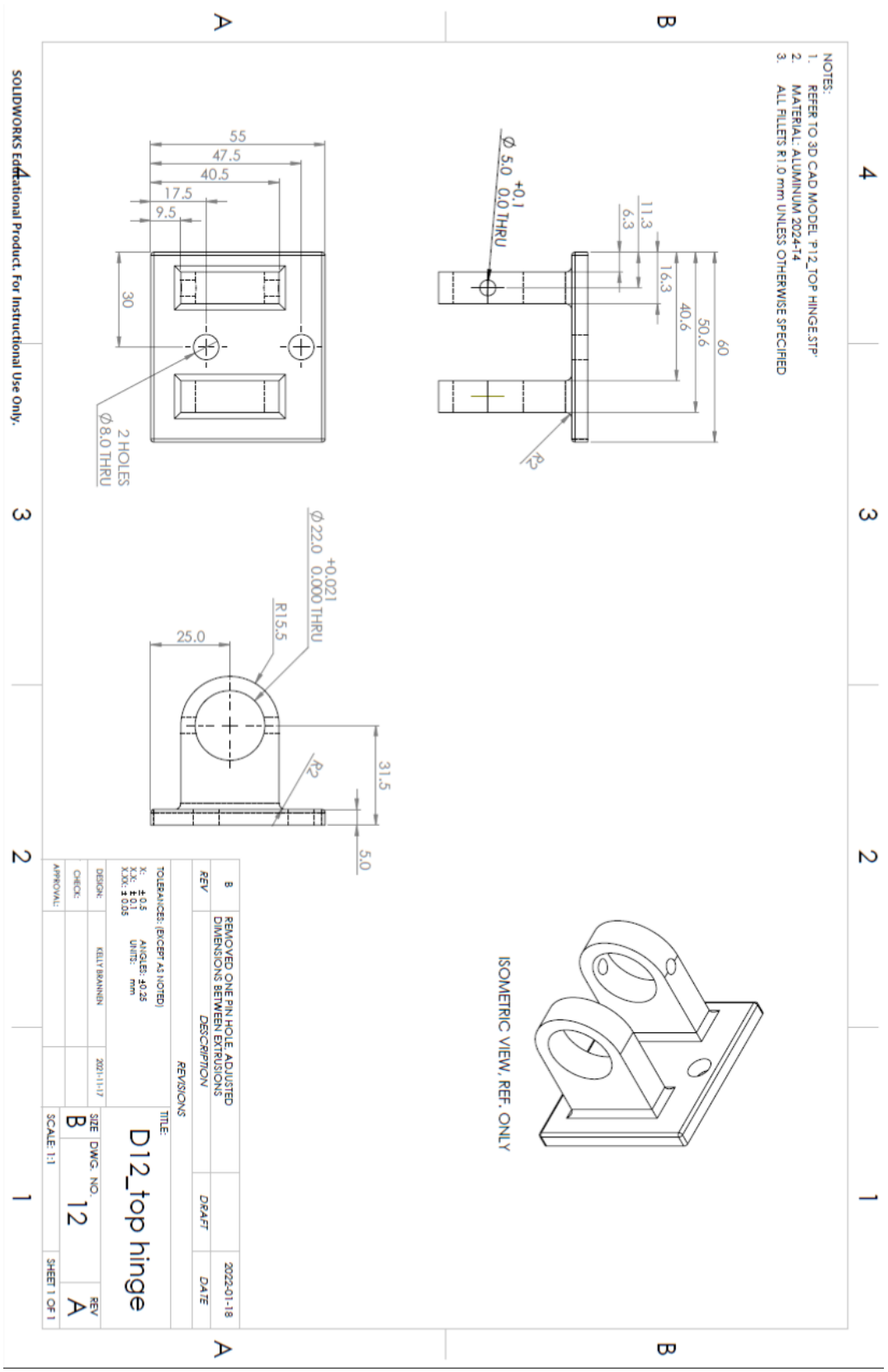

Figure A-10 Top hinge drawing

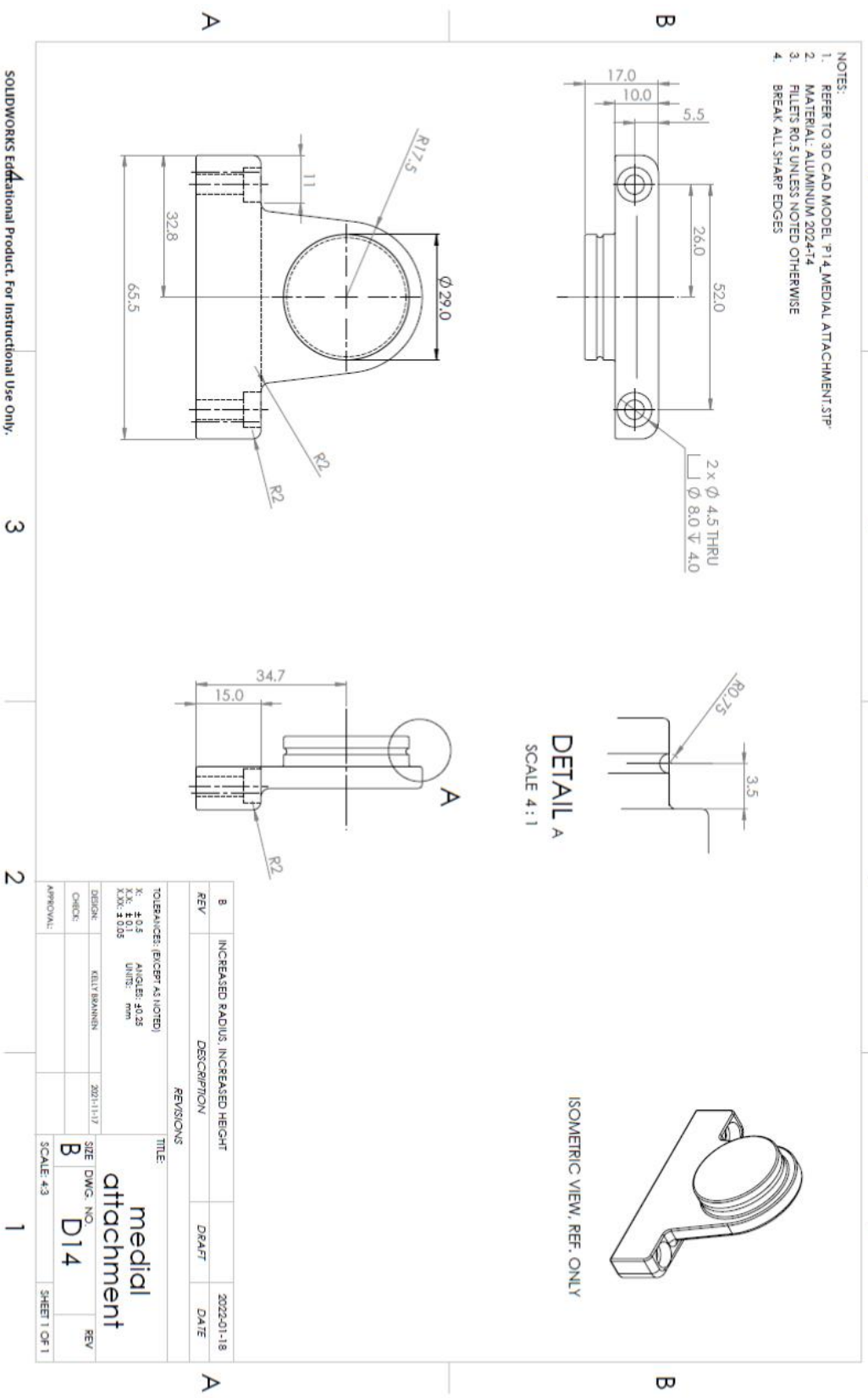

Figure A-11 Medial attachment drawing

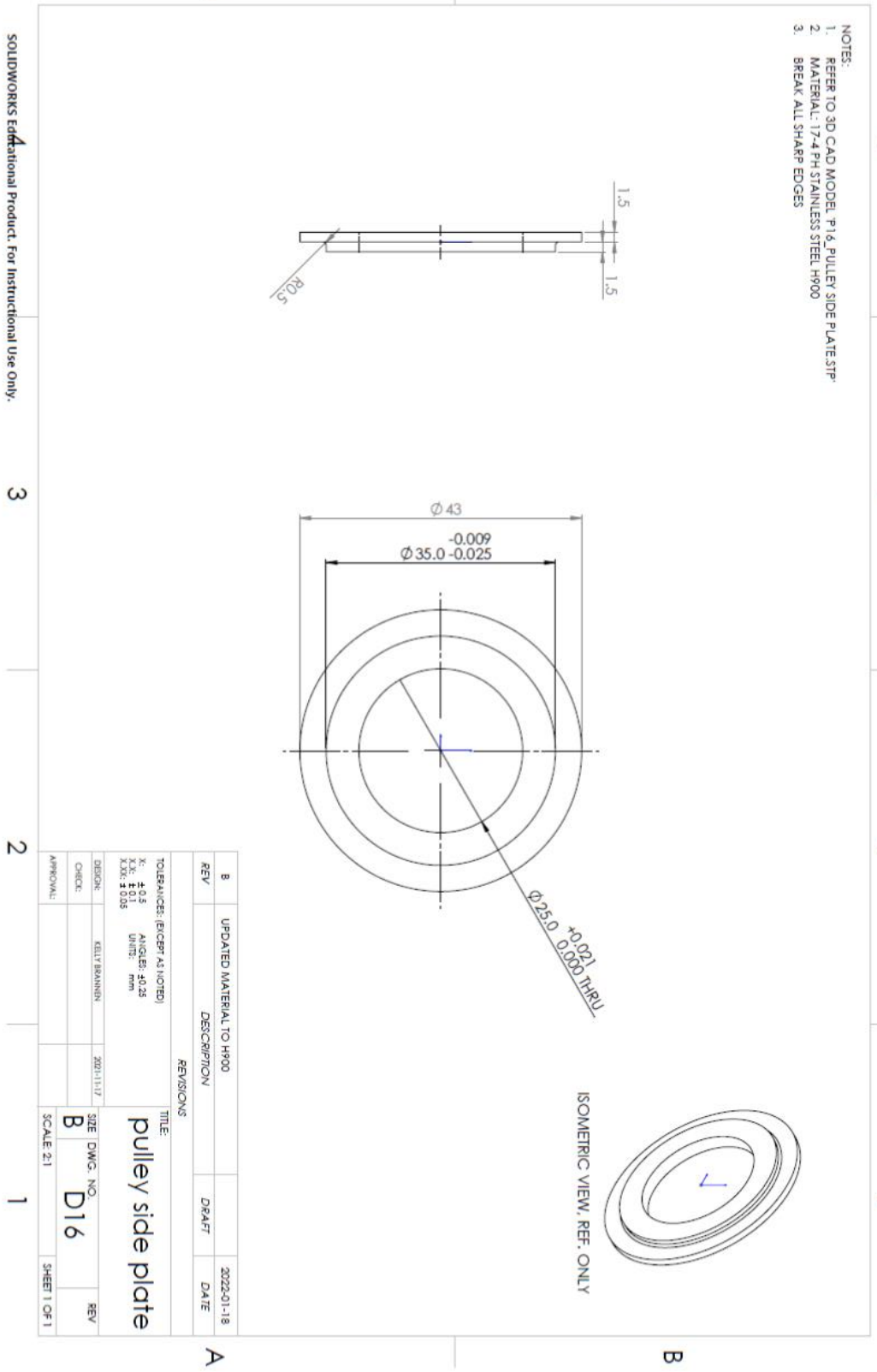

Figure A-12 Pulley side plate drawing

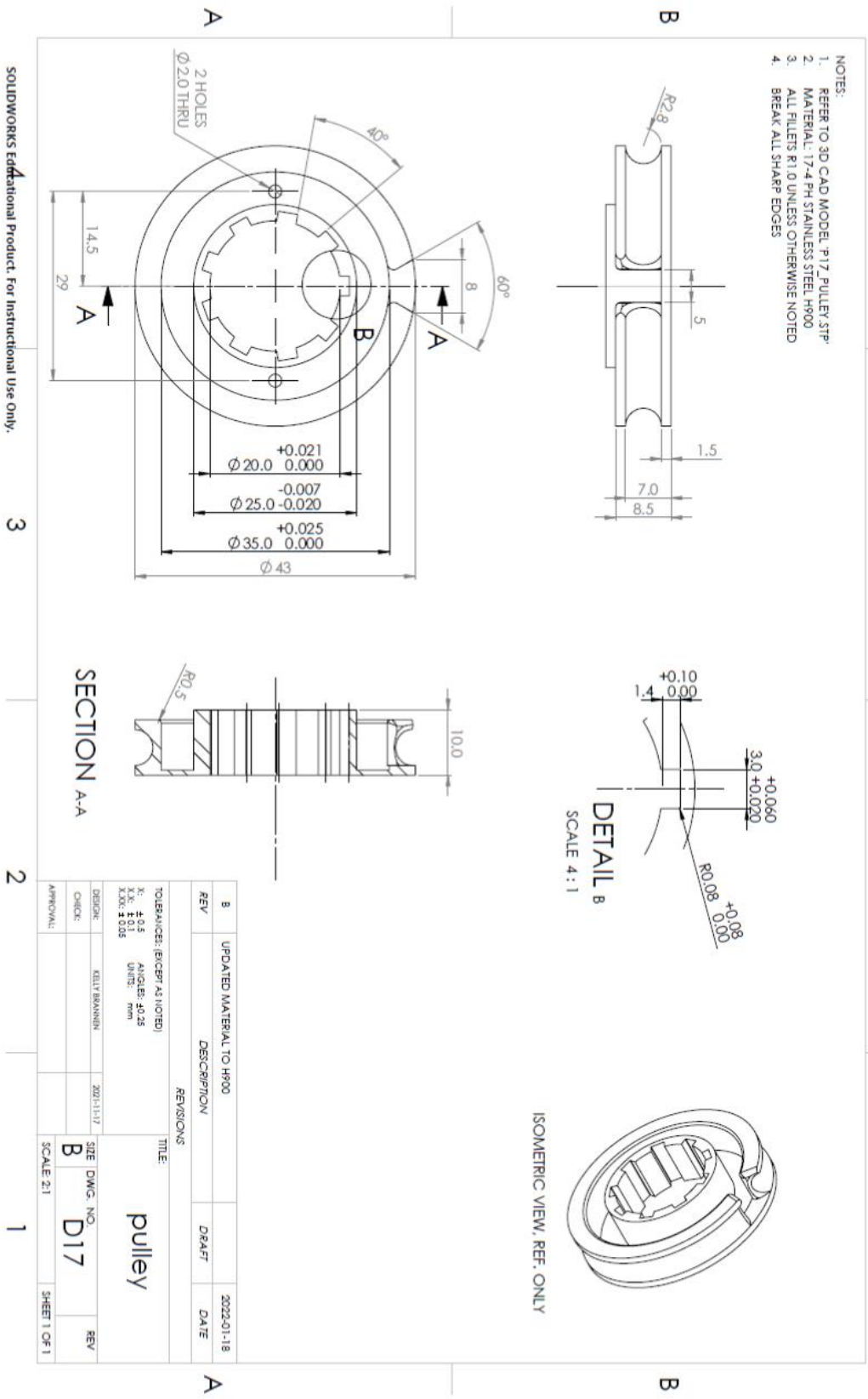

Figure A-13 Pulley drawing

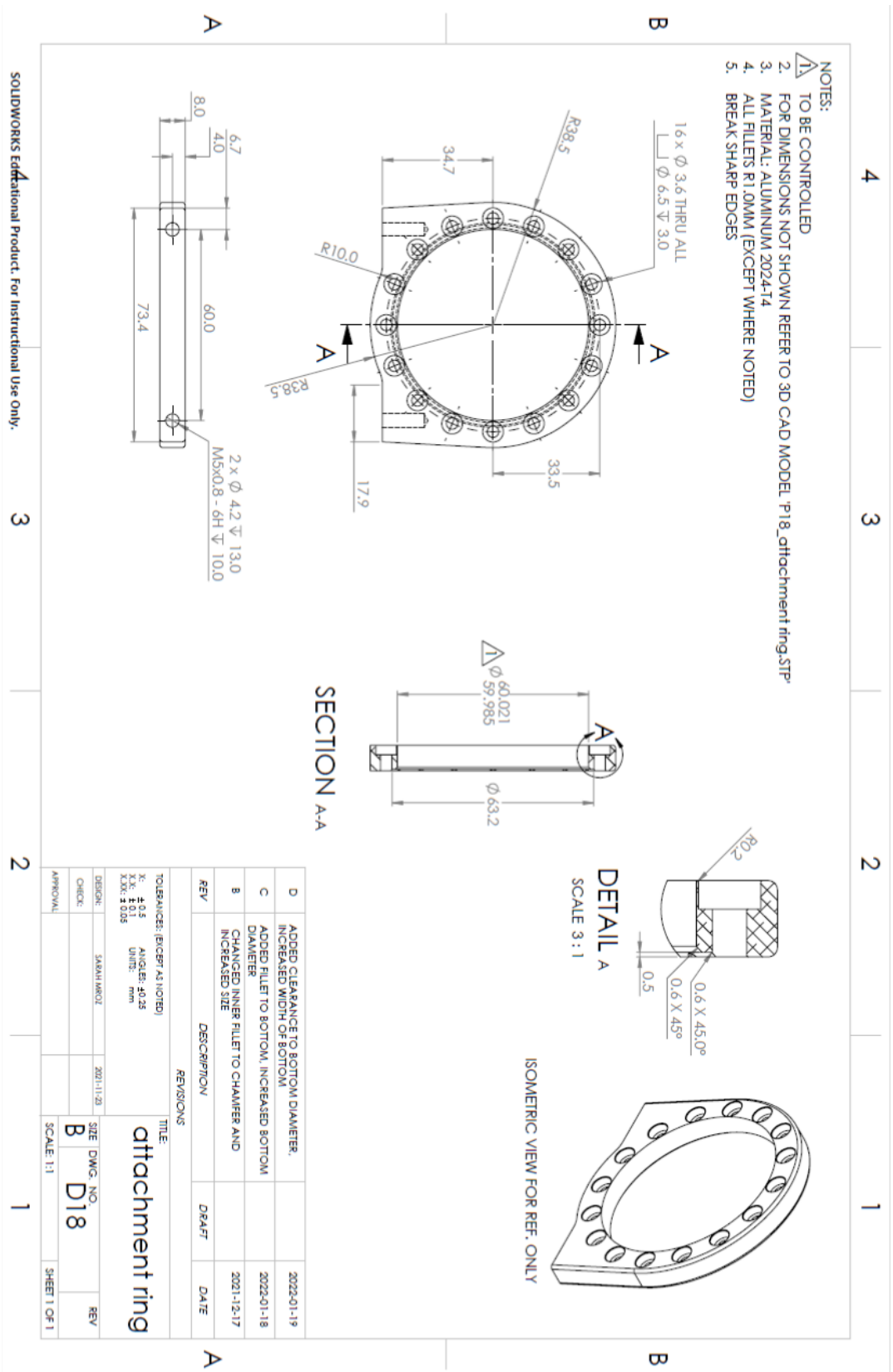

Figure A-14 Attachment ring drawing

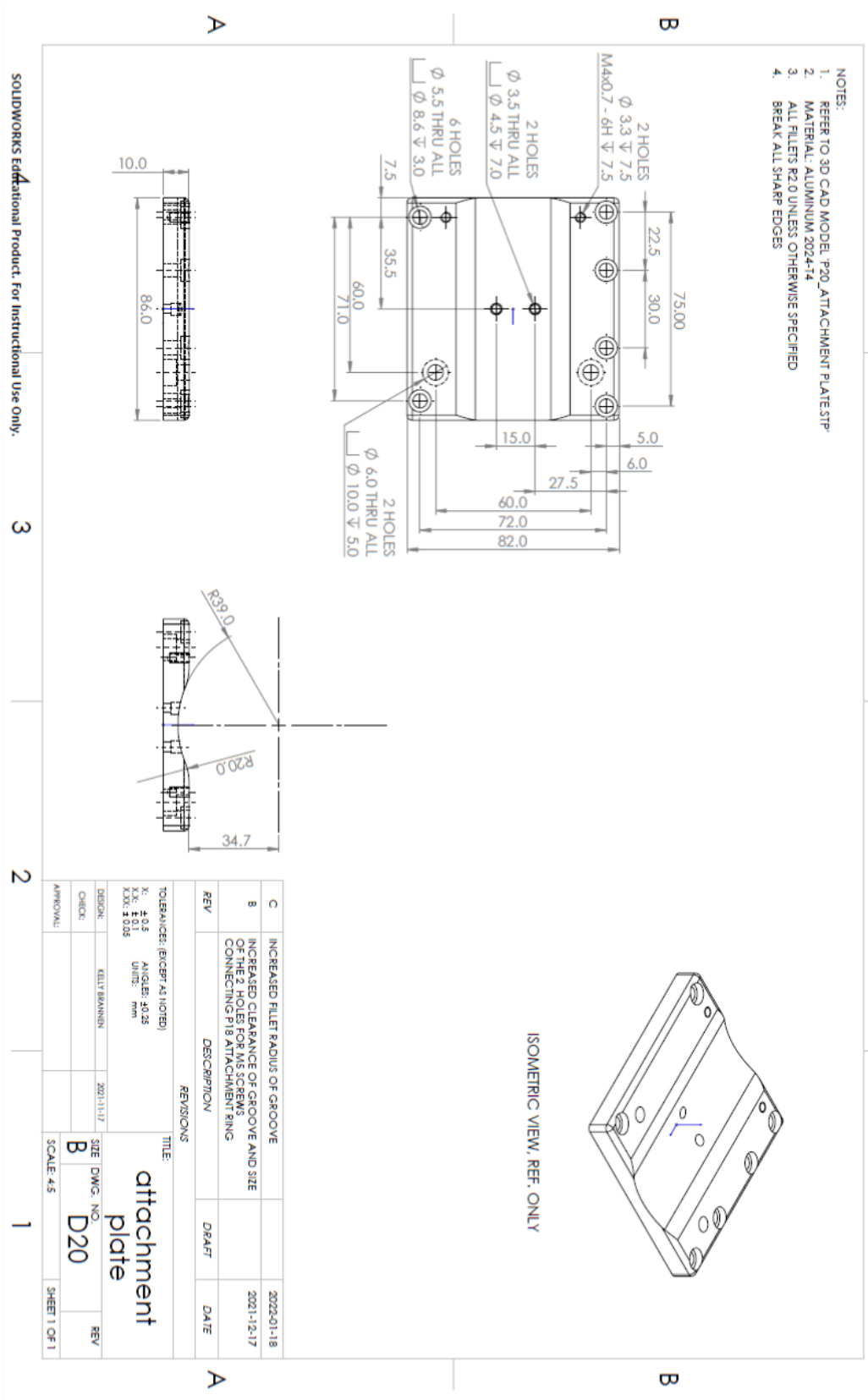

Figure A-15 Attachment plate drawing

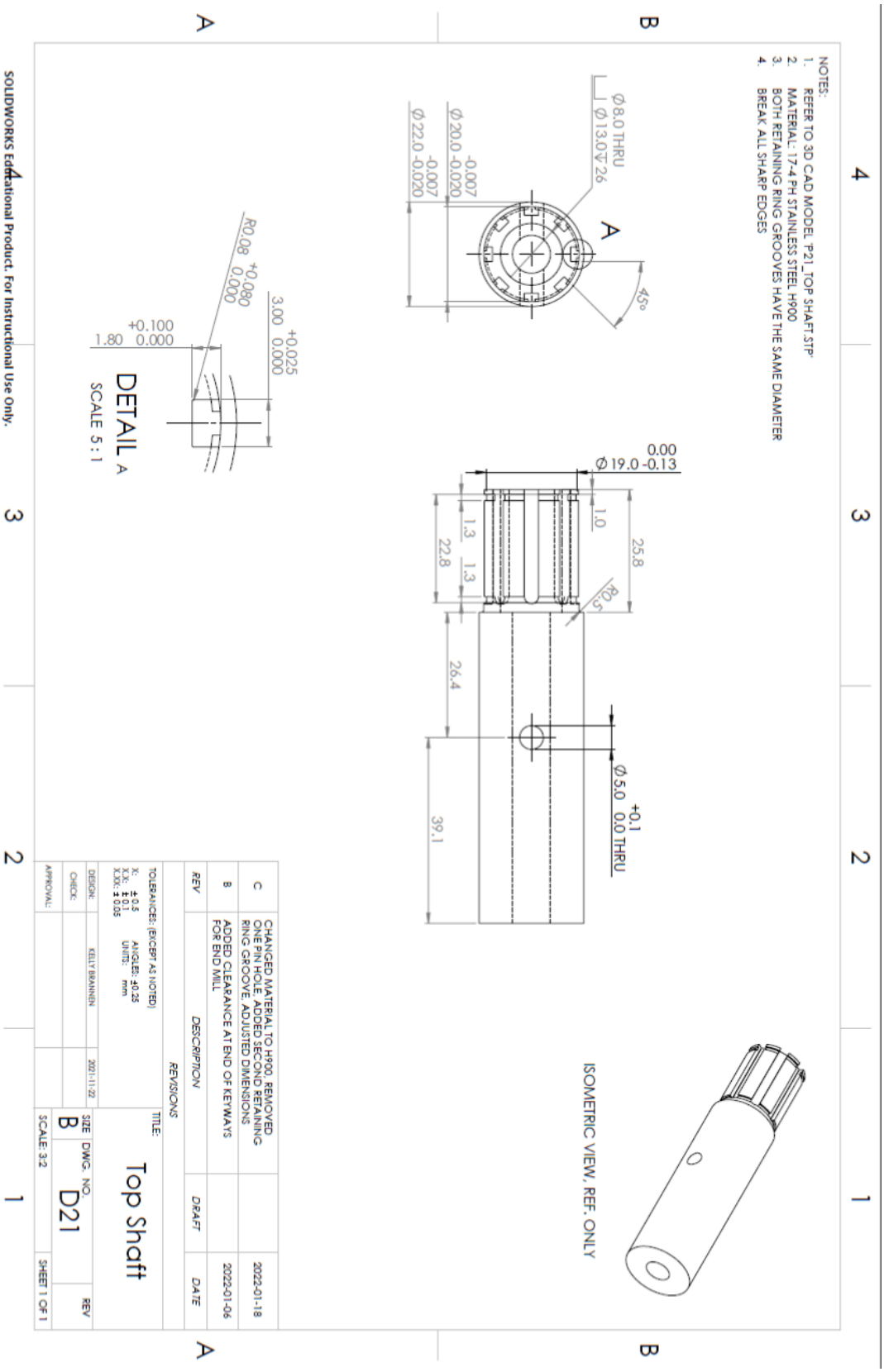

Figure A-16 Top shaft drawing

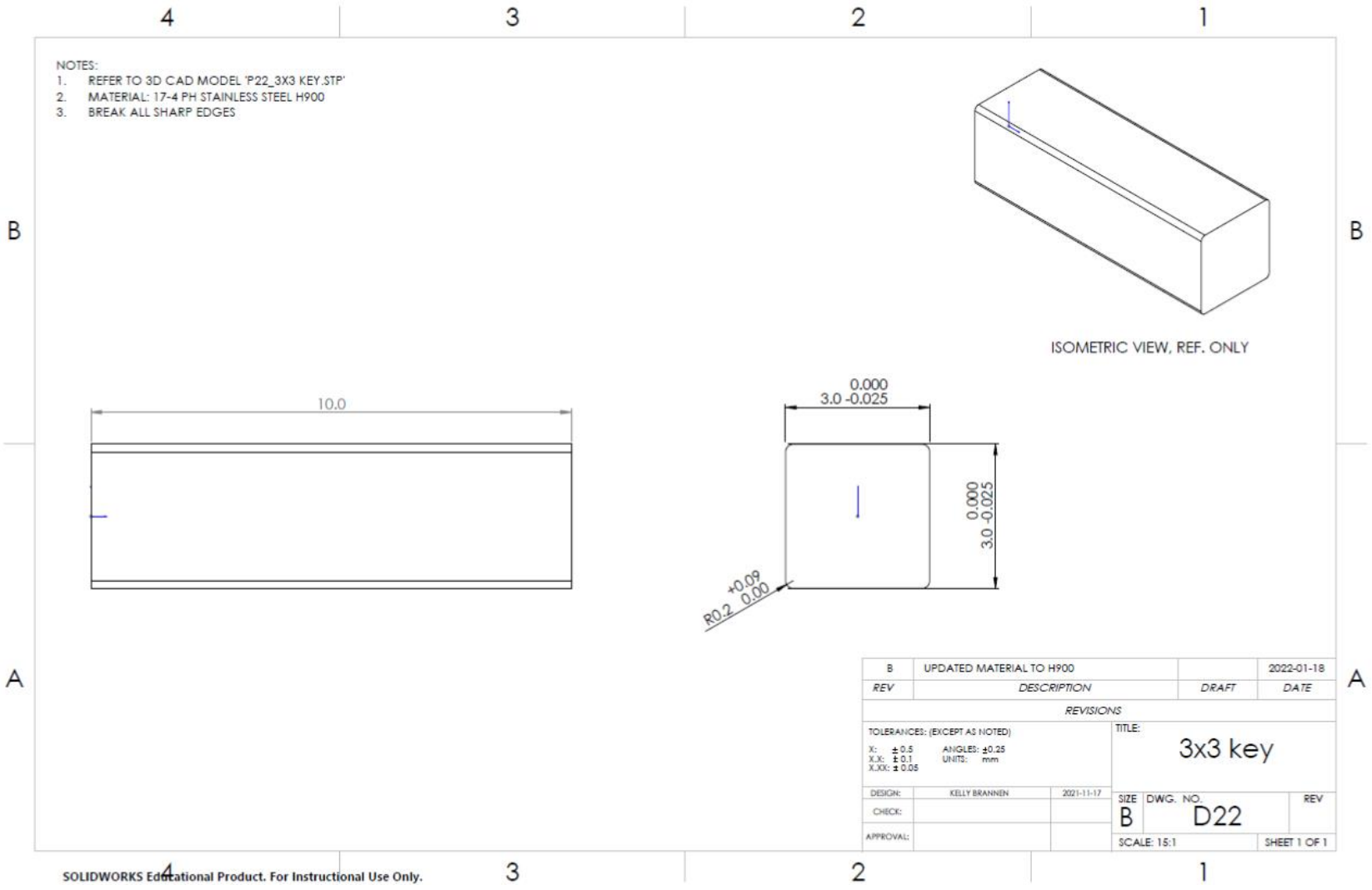

Figure A-17 Key drawing

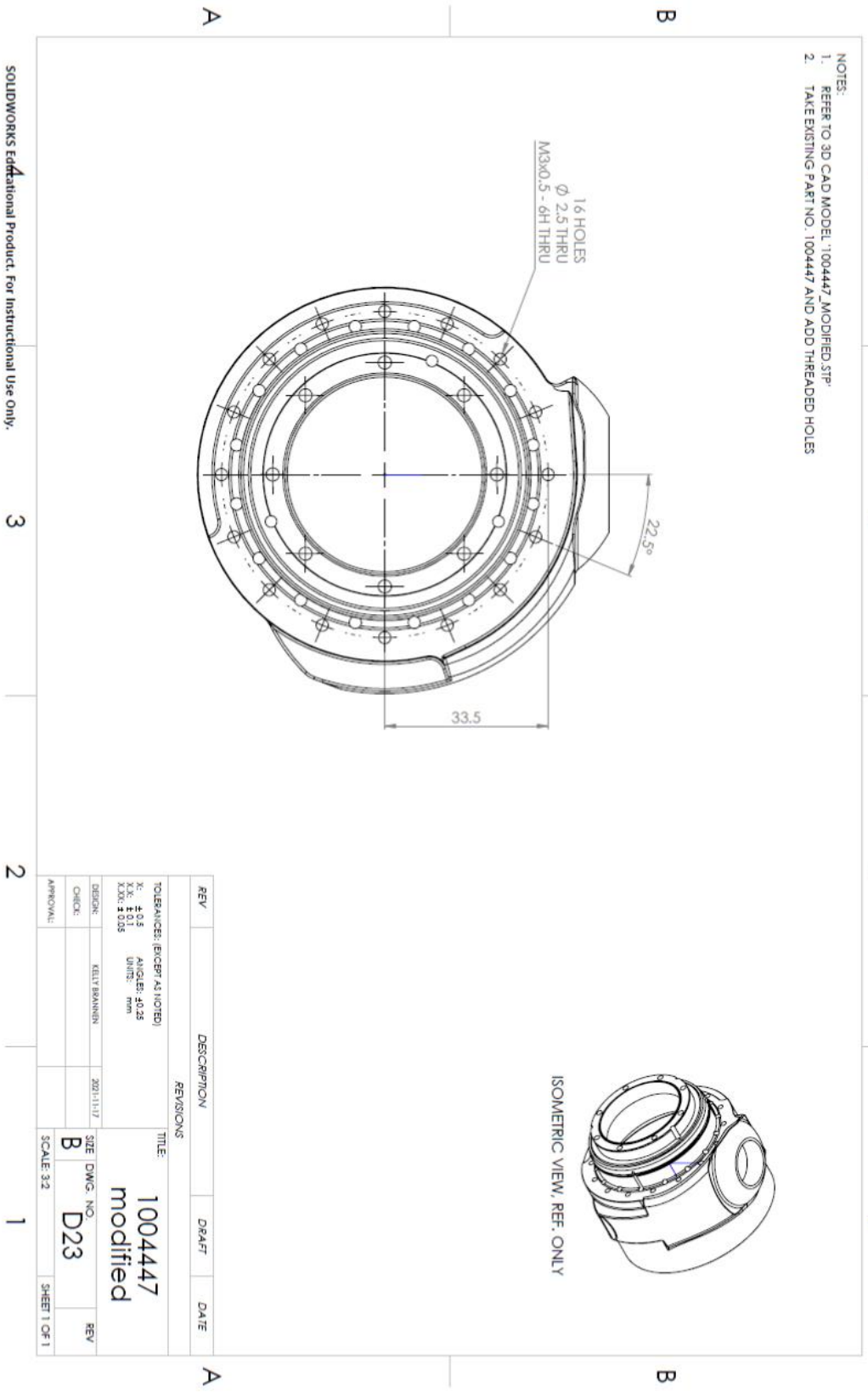

Figure A-18 Modified motor casing drawing

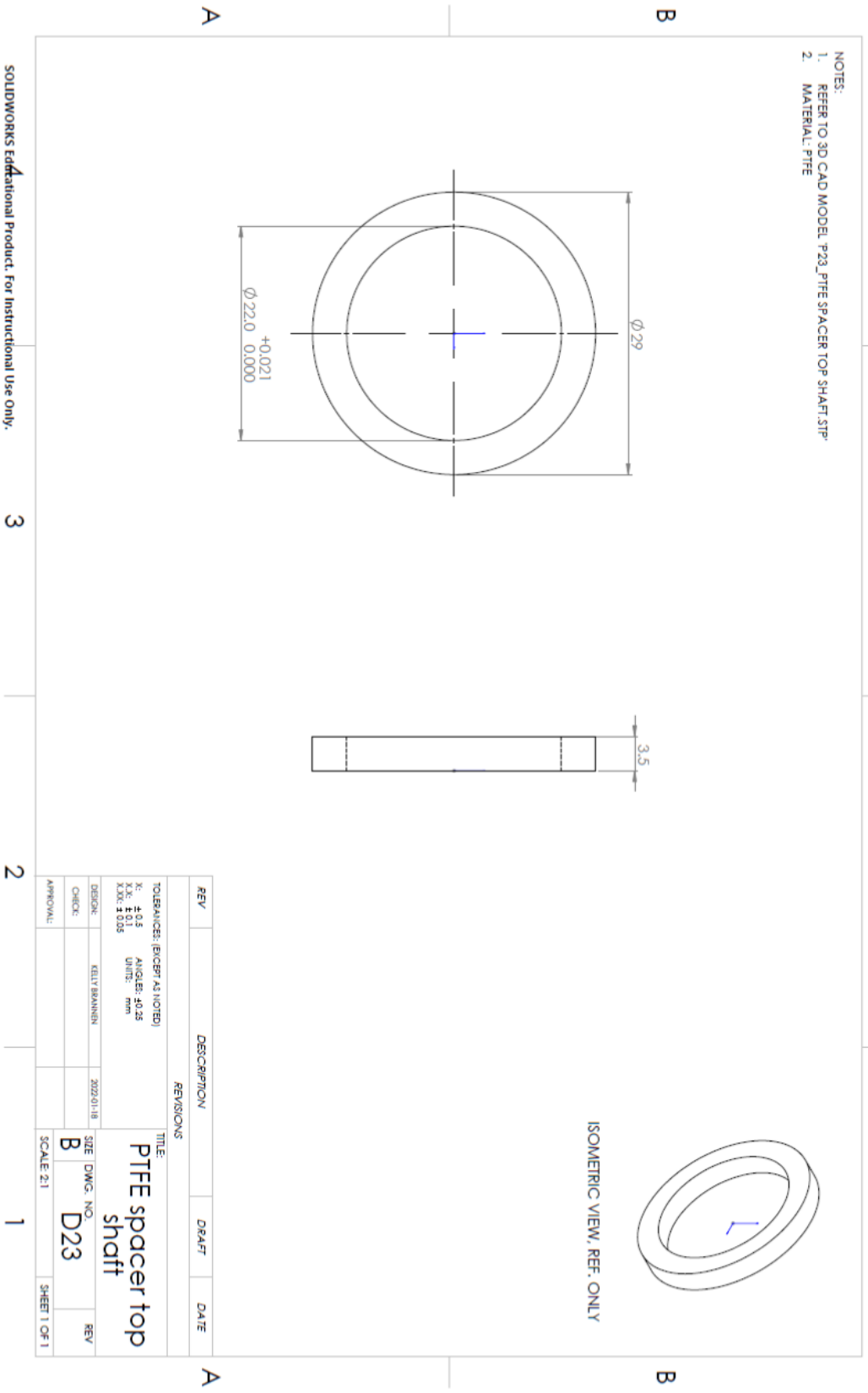

Figure A-19 Top shaft PTFE spacer drawing

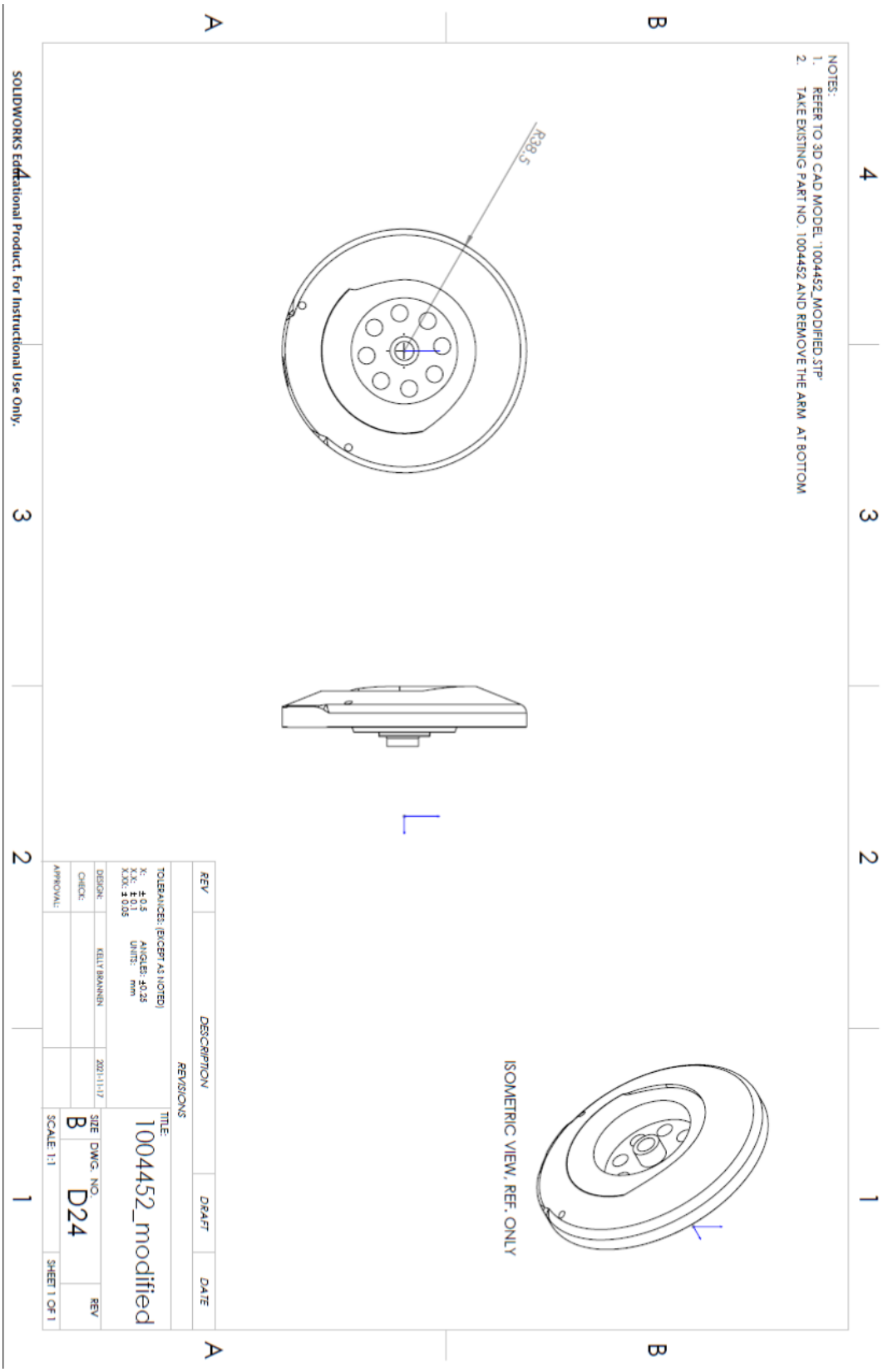

Figure A-20 Modified motor end plate drawing

Appendix B – Functional Testing Ethics Approval

25/08/2021

Université d'Ottawa
Bureau d'éthique et d'intégrité de la recherche

University of Ottawa
Office of Research Ethics and Integrity

CERTIFICAT D'APPROBATION ÉTHIQUE | CERTIFICATE OF ETHICS APPROVAL

Numéro du dossier / Ethics File Number	H-04-21-6811
Titre du projet / Project Title	DESIGNING AND EVALUATION OF A HIP DISARTICULATION PROSTHESIS SIMULATOR
Type de projet / Project Type	Recherche de professeur / Professor's research project
Statut du projet / Project Status	Approuvé / Approved
Date d'approbation (jj/mm/aaaa) / Approval Date (dd/mm/yyyy)	25/08/2021
Date d'expiration (jj/mm/aaaa) / Expiry Date (dd/mm/yyyy)	24/08/2022

Équipe de recherche / Research Team

Chercheur / Researcher	Affiliation	Role
Edward LEMAIRE	Département de médecine / Department of Medicine	Chercheur Principal / Principal Investigator
Amir FANOUS	Département de génie mécanique / Department of Mechanical Engineering	Étudiant-chercheur / Student-researcher
Michael BOTROS	Département de génie mécanique / Department of Mechanical Engineering	Assistant de recherche / Research Assistant
Natalie BADDOUR	Département de génie mécanique / Department of Mechanical Engineering	Co-chercheur principal / Co-principal investigator
Hossein GHOLIZADEH	Département de génie mécanique / Department of Mechanical Engineering	Co-chercheur / Co-investigator

Conditions spéciales ou commentaires / Special conditions or comments

550, rue Cumberland, pièce 154 Ottawa (Ontario) K1N 6N5 Canada
550 Cumberland Street, Room 154 Ottawa, Ontario K1N 6N5 Canada

613-562-5387 • 613-562-5338 • ethique@uOttawa.ca / ethics@uOttawa.ca
www.recherche.uottawa.ca/deontologie | www.recherche.uottawa.ca/ethics

25/08/2021

Université d'Ottawa
Bureau d'éthique et d'intégrité de la recherche

University of Ottawa
Office of Research Ethics and Integrity

Le Comité d'éthique de la recherche (CÉR) de l'Université d'Ottawa, opérant conformément à l'*Énoncé de politique des Trois conseils* (2014) et toutes autres lois et tous règlements applicables, a examiné et approuvé la demande d'éthique du projet de recherche ci-nommé.

L'approbation est valide pour la durée indiquée plus haut et est sujette aux conditions énumérées dans la section intitulée "Conditions Spéciales ou Commentaires". Le formulaire « Renouvellement ou Fermeture de Projet » doit être complété quatre semaines avant la date d'échéance indiquée ci-haut afin de demander un renouvellement de cette approbation éthique ou afin de fermer le dossier.

Toutes modifications apportées au projet doivent être approuvées par le CÉR avant leur mise en place, sauf si le participant doit être retiré en raison d'un danger immédiat ou s'il s'agit d'un changement ayant trait à des éléments administratifs ou logistiques du projet. Les chercheurs doivent aviser le CÉR dans les plus brefs délais de tout changement pouvant augmenter le niveau de risque aux participants ou pouvant affecter considérablement le déroulement du projet, rapporter tout évènement imprévu ou indésirable et soumettre toute nouvelle information pouvant nuire à la conduite du projet ou à la sécurité des participants.

The University of Ottawa Research Ethics Board, which operates in accordance with the *Tri-Council Policy Statement* (2014) and other applicable laws and regulations, has examined and approved the ethics application for the above-named research project.

Ethics approval is valid for the period indicated above and is subject to the conditions listed in the section entitled "Special Conditions or Comments". The "Renewal/Project Closure" form must be completedfour weeks before the above-referenced expiry date to request a renewal of this ethics approval or closure of the file.

Any changes made to the project must be approved by the REB before being implemented, except when necessary to remove participants from immediate endangerment or when the modification(s) only pertain to administrative or logistical components of the project. Investigators must also promptly alert the REB of any changes that increase the risk to participant(s), any changes that considerably affect the conduct of the project, all unanticipated and harmful events that occur, and new information that may negatively affect the conduct of the project or the safety of the participant(s).

Germain ZONGO
Responsable d'éthique en recherche / Protocol Officer
Pour/For **Daniel LAGAREC** Président(e) du/ Chair of the **Comité d'éthique de la recherche en sciences de la santé et sciences / Health Sciences and Sciences Research Ethics Board**

550, rue Cumberland, pièce 154
Ottawa (Ontario) K1N 6N5 Canada

550 Cumberland Street, Room 154
Ottawa, Ontario K1N 6N5 Canada

613-562-5387 • 613-562-5338 • ethique@uOttawa.ca / ethics@uOttawa.ca
www.recherche.uottawa.ca/deontologie | www.recherche.uottawa.ca/ethics